Nano-Prototyping and 3D Bioimaging with Dual Beam Microscopy

PhD thesis in physics

written by
Dieter Akemeier

Universität Bielefeld
2013

Declaration of authorship

I hereby certify that the work presented in this dissertation is my original work and that all passages and ideas that are not mine have been fully and properly acknowledged.

Bielefeld, November 21, 2013 Dieter Akemeier

Contents

1 Introduction

> I would like to describe a field, in which little has been done, but in which an enormous amount can be done in principle. This field is not quite the same as the others in that it will not tell us much of fundamental physics (in the sense of, "What are the strange particles?") but it is more like solid-state physics in the sense that it might tell us much of great interest about the strange phenomena that occur in complex situations. Furthermore, a point that is most important is that it would have an enormous number of technical applications.
>
> What I want to talk about is the problem of manipulating and controlling things on a small scale. (Feynman)

The quote above is from a famous talk held by Richard Feynman on December 29th 1959 - "There's Plenty of Room at the Bottom". In this talk he envisioned the advantages of miniaturisation. The striking part was not stopping at micro machining, but going a step further and giving the listeners a first impression of what true nanosized structures would offer. By now, there is a completely different understanding of what "small" means, as processors with millions of nanometer sized transistors are part of our everyday lives. Still further and further miniaturisation is important in many field and its advantages remain unchanged.

> "How do we write small?"

Electron microscopy was already available 1960, giving access to high resolution imaging. However, the creation of small features was still not possible. One of the tools envisioned by Feynman in his talk is a scanning electron microscope that uses ions instead of electrons. By now such machines are commercially available - focused ion beam microscopes. With such a device it is possible to write small. However, such a microscope is

not used for the production of nanostructures. Up till now it is mainly used for analytical applications. That is because there is an other method for nanoproduction that is dominant today.

This method is lithography. Lithography uses light to modify a resist in order to create structures. After complicated deposition and etching steps a feature is created. This is still a time consuming and complex process. The complexity even increases with every step of further miniaturisation. However, the possibilities for parallelisation make it a worthwhile. Without this parallelisation our computers would not be affordable. For process development and afterwards for quality control, high resolution analysis is required. Here, electron and focused ion beam microscopes have been important tools. The inorganic samples can be imaged fast and offer a good contrast in a scanning electron microscope. The focused ion beam microscopes are used to mill cross-sections or prepare lamellas for high resolution transmission electron imaging.

Returning to writing small. With the advances in lithography, driven by miniaturisation, the resolution and power of the analytical tools increased as well. A combination of a focused ion beam and a scanning electron microscope was created - the dual beam microscope. This unique device has the ability to write small features and image them. It is a powerful tool with many analytical applications. However, such a flexible device offers applications beyond semiconductor analysis. These are explored and described in this thesis.

The first application is small scale production of custom made nanostructures. Many experiments and devices could be improved with specifically tailored elements. However, a small batch size coupled with high precision requirements makes production of those elements not feasible with conventional lithographic means. In this thesis, dual beam production is used to create nanotextured apertures for a next generation super resolution microscope. Therefore, a specialised process and automation routines were developed for the dual beam microscope.

> Is it possible, for example, to emit light from a whole set of antennas, like we emit radio waves from an organized set of antennas to beam the radio programs to Europe? The same thing would be to beam the

> light out in a definite direction with very high intensity. (Perhaps such a beam is not very useful technically or economically.) (Feynman)

The second topic is the creation of nanoantenna arrays. Small antenna arrays were already mentioned in Feynmans talk as an interesting topic for nanotechnology. While in the 1960s Feynman had no idea of their possible application, Kim et al. proposed them as a tool for higher harmonics generation in 2008 [Kim08]. Here, a dual beam microscope is used to create the nanoantennas. The flexibility offered by this production process (in comparison to high resolution lithography) allows fast modifications of significant features. Through programming the dual beam microscope it is possible to rapidly create a wide range of prototypes with different parameters. In combination with theoretical models, experimental parameters can be explored very fast. The theoretical models also show increased effects in the active region of the antennas for very small dimensions (<20 nm). The structuring process used to create features of and below 20 nm is explored in detail.

> We have friends in other fields - in biology, for instance. We physicists often look at them and say, "You know the reason you fellows are making so little progress?" (Actually I don't know any field where they are making more rapid progress than they are in biology today.) "You should use more mathematics, like we do." They could answer us - but they're polite, so I'll answer for them: "What you should do in order for us to make more rapid progress is to make the electron microscope 100 times better." (Feynman)

A dual beam microscope with its unique combination of high resolution imaging and micro manipulation can become an effective tool for working on interdisciplinary topics. While the resolution of a scanning electron microscope has not been increased a hundred fold, the combination with precision milling gives a dual beam microscope access to a new dimension - invisible before! Using these it should be possible to create 3D models of tissue with unprecedented volume and resolution. However, dual beam tomography is a recent development and still not widely used. In order to demonstrate the possibilities and improve upon the methodology, this

method was applied to different tissue samples. Most of the work was done on a vital part of the kidney - the glomerulus. The reconstructed volume showed the possibilities offered by this novel technique and also revealed new biological features.

Structure of this thesis

This thesis is composed of three main parts, each focusing one a single topic. Each chapter has a similar structure with a separate introduction, basic background, experiment, result and outlook sections. While the chapter topics differ greatly, they are all connected through the method used for nanomanipulation - a dual beam microscope and scripting automation. The final outlook chapter is focused on the method and its further applications rather than the specific application presented in the main matter parts.

2 Dual beam microscopes

This work is centred around dual beam techniques. Most of the work was done with a dual beam microscope - the Helios NanoLab 600i (FEI, Netherlands). A dual beam microscope is a combination of a scanning electron and a focused ion beam microscope. The main disadvantage of conventional focused ion beam microscopes are their imaging properties. This severely limits their application. In dual beam microscopes this problem is migrated through the scanning electron column, which is subsequently used for imaging. Dual beam devices thereby combine high resolution imaging with high resolution milling. In addition a dual beam microscope offers applications which are not possible with the individual devices.

The particle beams (electron and ion) are created with the same sources and accelerator columns as in the respective single beam devices. However, both columns are facing the same vacuum chamber and are aligned to share a coincidence point. Working at the coincidence point allows ion milling and electron imaging of the same sample area. A sketch of a dual beam setup and the coincidence point is found in illustration 2.1. In most cases, the angle between both columns is between 45° and 52°. A motorised stage is used to bring the sample to this point and tilt it perpendicular to the respective beam.

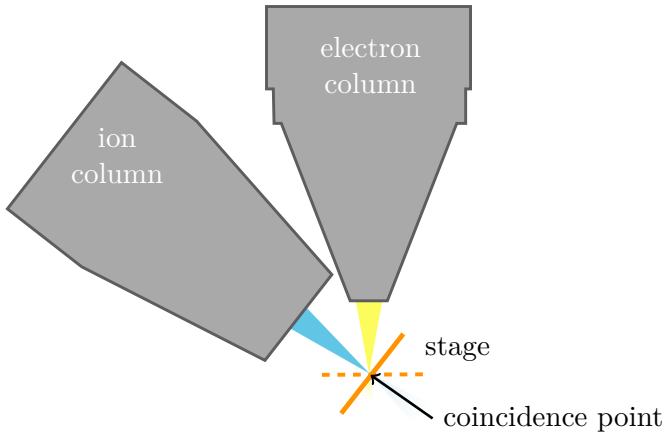

Figure 2.1: Sketch of the dual beam setup. At the coincidence point both beams (electron and ion) overlap. The stage is used to move the sample to this point.

2.1 Scanning electron microscope column

A scanning electron microscope uses electrons for imaging. A beam of electrons is generated and accelerated towards the sample. The beam is focused into a small spot and then scanned across the surface of the sample. The electrons interact with the sample, producing various signals that contain information about the sample topology. In order to generate an image, the detector signals are combined with the beam positions.

A scanning electron column consists of an electron gun, a series of electromagnetic lenses, alignment and scanning coils. A sketch of a scanning electron microscope column is shown in illustration 2.2.

The electron beam is created by an electron gun. Multiple types of electron guns are available. In the Helios NanoLab 600i, a Schottky thermal field emitter is used. In a field emitter electron gun (FEG), the electron beam is created through field electron emission. Hence, a strong electric field (multiple kV) is applied to a sharp tungsten tip. In thermally assisted field emission the tip is heated to near melting temperature in order to

increase the electron yield.

Electromagnetic lenses are used to focus the beam. In the lens systems, multiple coils are used to generate a magnetic field. Through the lens current the strength of this field and thereby the refractive power of the lenses is controllable. The scanning and stigmation coils also use magnetic fields to create the raster scan pattern of the beam and to make stigmation adjustments.

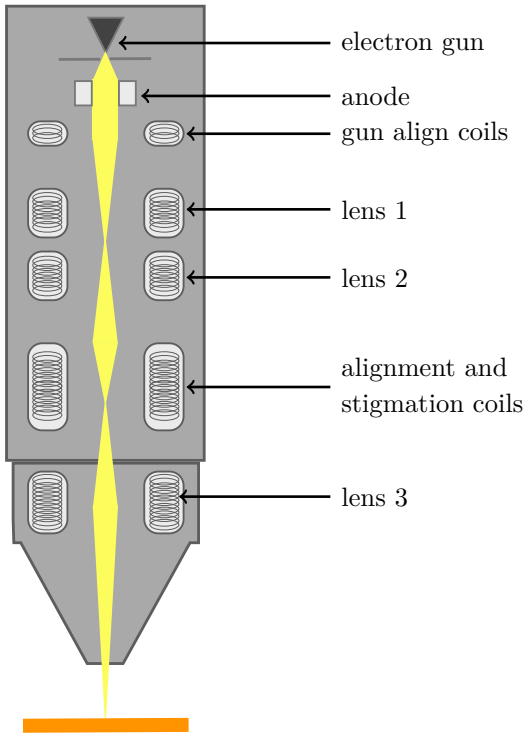

Figure 2.2: Sketch of a scanning electron microscope column.

2.2 Focused ion beam

A focused ion beam microscope is similar to a scanning electron microscope as both microscopes create a beam of charged particles and focus it towards the sample surface. In both setups the surface is scanned in a rasterised fashion. However, instead of electrons, ions are used. Due to their high kinetic energy, the ions modify the surface and can sputter surface atoms. Though it is possible to take images with a focused ion beam device, the ions will modify and possibly destroy the sample after prolonged scanning. On the other hand the ion can be used to selectively remove material from the sample surface. Using the scanning coils to steer the ion beam, material can be removed with high precision. In a dual beam microscope therefore, the scanning electron column is used for imaging, while the ion beam is used for sample manipulation. Most of the time milling is used to support analytical applications, either by removing cover layers or through the creation of cross-sections and transmission electron microscopy lamella.

A focused ion beam device column is similar to a scanning electron microscope column. A sketch of an ion column is shown in illustration 2.3. Due to the positive charge of the ions, electrostatic lenses are used instead of the electromagnetic.

There are different types of ion sources available. The first ion beam microscopes used a field ion source to ionise hydrogen [Esc75]. Newer models use liquid metal ion sources (LMIS). The use of gallium has several advantages. It has a low melting point and thereby only needs very limited heating to stay in liquid phase. The gallium ions are heavy enough to allow milling of heavy materials, but do not instantly destroy soft samples. In addition, the low vapour pressure of the material greatly benefits the source construction. In contrast, for materials with higher vapour pressure an alloy source must be used, which then complicates column design as an additional mass separator must be employed [Yao07].

In most setups, including the Helios NanoLab, a gallium liquid metal ion source is used to generate the ion beam. Gallium is heated to near the evaporation point and flows over a heat resistant tungsten needle. The gallium atoms are drawn to the tip of the needle by an annular electrode (extractor) positioned concentric over the tip. The combination of surface

tension and electrostatic forces draws the liquid metal into a sharp tip with an apex of approx. 5 nm (taylor cone). This cone tip is small enough that ions can be efficiently ionised through field evaporation by the extractor voltage and are then accelerated through the ion column [Yao07]. A second electrode, called suppressor, is used to regulate the created ion current. After the ion current is started by a high extractor voltage, the suppressor voltage is slowly ramped up until the beam current is reduced to a stable 2 µA.

After creation, the beam current is further regulated through an aperture dial. In the Helios NanoLab the standard aperture dial has 15 different drill holes, which can be used to set eleven different beam currents. High use apertures exist twice, this minimises the effects of wear on the aperture and increases the overall lifetime. The aperture diameter is also directly proportionate to the beam diameter. A smaller aperture current offers a smaller overall beam diameter and thereby a higher patterning resolution. The commonly used apertures and their applications are:

21 nA The highest current available, only used for large scale rough cutting.

2.8 nA A high current milling aperture, used for rough cuts and regular cross sections.

93 pA An aperture used for high precision milling, polishing and cleaning cross sections.

28 pA The default imaging current. It still has a good brightness, but does not modify the sample surface rapidly. However, continued scanning or high resolution small area scans can significantly mill a sample.

1.5 pA The smallest possible ion current. Most images do not yield enough contrast to be viable. Used for maximum resolution milling, as this aperture offers the smallest beam diameter.

For all beam currents above, an accelerator voltage of 30 kV was used. For smaller voltages the beam currents are also reduced.

Milling is the main application of a focused ion beam device. Apart from the beam current, the mill rate is also dependent on the sputtered material.

Generally, metals have significantly higher milling rates than insulators. In most focused ion beam devices, material specific mill rates are saved in specific application files.

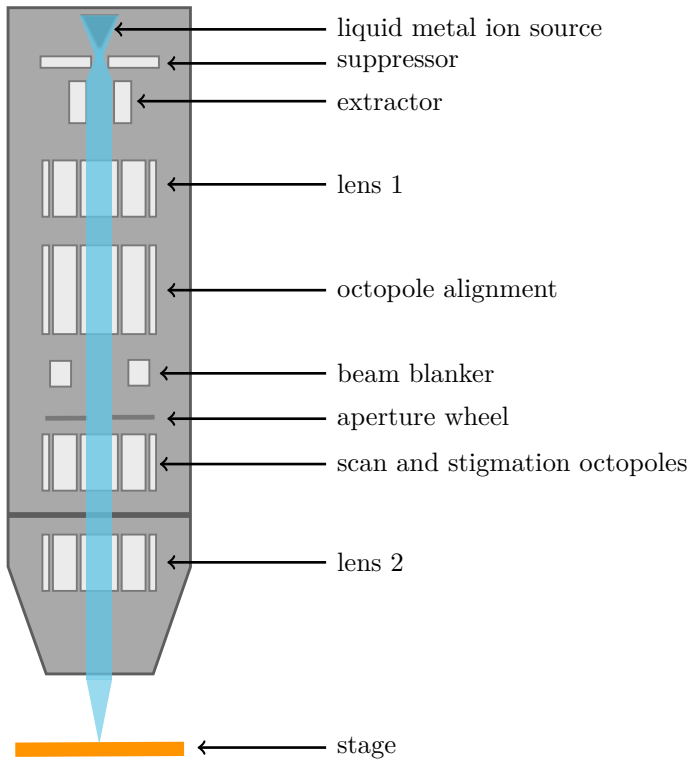

Figure 2.3: Sketch of a focused ion beam column.

2.3 Detectors

There are multiple detectors available in a dual beam microscope. The most common is a secondary electron detector. Secondary electrons are ionisation byproducts and can be generated by either beam. Edges normally show a higher secondary electron signal, because their interaction area with

the primary beam is bigger. Hence they are brighter in the resulting micrographs. A Everhart-Thornley secondary electron detector consists of a scintillator inside a faraday cage. A small positive voltage of around 50 V is applied to the faraday cage in order to attract the low energy secondary electrons and guide them into the detector. Inside, a high positive voltage of multiple kV is used to accelerate the electrons towards the scintillator [Eve60]. Some detectors have additional energy filters to further narrow the energy spectra.

Most scanning electron microscopes are equipped with a backscattered electron detector. Backscattered electrons are beam electrons elastically scattered by the atomic cores of the sample. Heavy atoms reflect more electrons and are therefore, brighter in the resulting micrographs. This gives backscattered electron images an element specific contrast. Very few electrons are scattered under an angle, most are reflected backwards. Therefore, the detector is a donut shaped scintillator situated concentric around the electron beam to increase the detection yield.

In the Helios NanoLab, an additional electron detector is available. This detector is a transmission detector for scanning electron microscopes (STEM detector). While the previously described detectors are situated near the electron column and face the top of the sample, the STEM detector is inserted under the sample to detect transmitted electrons. Therefore, the samples must be sufficiently thin (<100 nm) to transmit electrons. The detector consists of different segments and by changing the active segment, different detection modes can be selected. It offers detection settings comparable to bright and dark field imaging of conventional light microscopy. In addition, STEM imaging offers an increased resolution[1] and the imaging modes can increase the contrast.

Ion imaging

It is possible to take micrographs with the ion beam as well. When the ion beam interacts with the surface, secondary electrons as well as secondary

1 Thin transmission samples have a more localised volume, in comparison to regular samples, where the electrons can interact with the sample.

or sputtered ions are created. The electrons can be detected with the secondary electron detector. The maximum achievable resolution of an ion beam is somewhere between a long exposure and a fast scan [Orl96]. The limiting factor is the relationship between surface milling and secondary electrons created. Small features can be sputtered away before sufficient signal electrons are collected on the detector [Orl96].

In addition to this secondary electron detection, some microscopes have ion detectors. Ion detectors are similar to the Everhart-Thornley detector. However, the sign of the applied voltages is reversed to attract positively charged ions. Ion images have a high surface sensitivity, but due to the low resolution/high noise they have a limited application.

2.4 Gas injection systems

The Helios NanoLab is equipped with a gas injection system. This allows the deposition of materials in situ. The most common application is the deposition of materials during the preparation of transmission electron microscope lamella. However, the system is very flexible and offers additional options for sample preparation and fast prototyping. It has the ability to deposit a platinum based conductor and carbon based insulator.

There is a wide range of other materials available. All materials share a shell of organic precursor molecules. The materials are normally stored in solid phase in a small heating/sublimation setup. For deposition they are heated to sublimation temperature. A guiding system, shaped like a hollow needle, is inserted into the microscope. Through this the gas is injected into the chamber and brought very near to the sample surface. The precursor shell can be decomposed through the interaction of the electron or ion beam with the solid surface. The target material can then adhere to the sample surface through Van der Waals forces [Lip96] [Tao90].

2.4.1 Direct write lithography

Lithography with a dual beam device differs from resist based lithography. The main difference between creating a structure with a focused ion beam

and creating a structure with standard resist based lithography is that a dual beam does not require a resist.

In a standard lithography process a structure is created in the resist layer and subsequently transferred to the sample. The two basic transfer processes are liftoff and selective etching. In a liftoff process material is deposited onto an exposed and developed resist layer. Afterwards the resist is removed. The selective etch method uses the resist layer as an etch mask for either a chemical wet etch or an argon ion milling. For both methods the resist acts as an intermediary. A structure is always initially created in resist and then transferred to the actual material. The need for a resist step in between the transfer processes makes it impossible to create patterns in multiple layers that rely on each other during one process step, e.g. creating a sensor element and contacting it through a passivation layer.

In a focused ion beam the materials are modified directly by the ions. There is no need for a resist exposure and complicated structure transfer processes. The etching is replaced by ion beam milling, and the lift-of processes are replaced by gas injection assisted deposition. This makes structuring in a focused ion beam completely sequential. It is possible to create multilayer patterns in a single process step, e.g. defining a sensor through milling, passivating it with an insulator layer and contacting it.

2.5 Helios NanoLab 600i

The Helios NanoLab uses a five axis motorised stage. In XY-direction it has a movement range of 150 mm and in Z a range of 10 mm. The repeatability of a stage move is 1 µm. The stage has a tilt range between $-10°$ and $60°$. For the range between $50°$ and $54°$ the tilting accuracy is $0.1°$. For milling the stage is tilted towards the ion column and then brought to coincident height. Most milling is done with the ion beam perpendicular to the sample surface. For the Helios NanoLab this is a tilt of $52°$. The coincident distance is at 4 mm, measured from the tip of the pole shoe of the electron column towards the sample surface. The stage is fully rotatable and has a compucentric rotation feature.

The Helios uses a field emission scanning electron microscopy (FESEM)

column with a Schottky thermal field emitter. It has a 60° dual objective lens with pole pice protection. The achievable resolution depends on the accelerator voltage. It is 0.8 nm for 15 kV and 1.2 nm for 1 kV. A FEI Tomahawk column is used as an ion column. The possible accelerator voltages range from 30 kV to 500 V. The lowest acceleration voltage of the ion column is only used for ultra fine polishing. The maximum resolution of the ion beam is 4 nm at 30 kV. The column can produce a maximum beam current of 65 nA. However, in the configuration used in our lab, using the biggest aperture available, the maximum current is 21 nA. The lifetime for the respective sources is 1 year for the electron source and 1000 h for the ion source.

3 Scripting - Automated structuring with dual beam microscopes

A dual beam microscope is commonly used for quality control and analytical applications in many different branches of industry and research. It combines electron imaging with high resolution feature milling and pattern generation. This could make a dual beam microscope a powerful device for prototyping and small scale production. However, it still relies on many different manual commands to define features and start milling processes. There are some predefined automation routines, e.g. the trench cutting for transmission electron microscopy lamellas. However, these do not offer an environment flexible enough to support a higher level of automation or enable prototyping.

For advanced prototyping applications a flexible automation environment is desirable. Without it dual beam microscopes lack the abilities to create and recreate complicated structures. Some applications, like the above mentioned lamella preparation, are based on an underlying scripting language. This scripting engine offers access to many machine variables and has a good control over the patterning engine. With the scripting automation a dual beam setup has all the tools needed for a fast prototyping on the nanoscale. Though the structure creation and analytical option are available per default, only the addition of automation gives one the ability to create and improve a process reliably. With an available automation routine, a structure can be created and analysed. If any errors are found or improvements are necessary, these can be implemented into the automation routine. This workflow is needed for every form of lithographical development. When working with a dual beam microscope, the entire process (structure creation and analysis) takes place within one machine without breaking the vacuum. This decreases the developing time greatly.

3.1 Basic scripting commands

The script used for controlling the Helios NanoLab has access to all basic functions of the device. It is possible to control the position of the five axis stage, the gas injection system, beam currents, accelerator voltage and the magnification. In addition simple patterns can be created and positioned. Complicated applications can be created through loops and simple mathematical functions. Scripts are written with a text editor and are run using the helper program 'runscript' on the Helios control computer.

The most basic commands are the set commands. They are used to set global machine variables like the beam current, beam tilt and accelerator voltage. An important variable for patterning applications is the write field size. For dual beam structuring the write field corresponds to the area reachable with the patterning beam. It is thereby determined by the magnification. The code to set the write field to a specific width is shown in illustration 3.1. The application type and the overall patterning z-dimension is also determined through the set command. For example the 'setpatinfo 0.2, Pt dep' changes the application to platinum deposition and sets the height to 200 nm for all further patterns.

The script supports the creation of four basic pattern shapes: box, obox, circle, line and polygon (Figure 3.2). The 'obox' command creates an outlined box. Their positions and sizes must be given as part of the command in microns using the centre of the write field as the origin. The box commands are defined by the positions of their diagonal, while for the line both end points must be given. Circles are defined by giving their centre location and an inner and outer radius. For polygons all edge position are required. Complex patterns must be created by combining these shapes. The command 'mill' starts milling or deposition of all defined patterns in the active write field. All patterns can be deleted using the 'clear' command.

The Helios NanoLab does not offer a simulator to dry run scripts. This makes debugging script files difficult and time consuming. In order to check the script file for errors, it must be loaded with the 'runscript' program and tested live on the dual beam microscope. The scripting engine is a powerful toolbox, giving the user great control over many microscope settings. However, there are no fail safe mechanisms or additional security

```
getmag
hfw = 4096/dacppm
sethfw = 128
hfwratio = hfw/sethfw
setmag (mag*hfwratio)
```

Figure 3.1: A script to set the horizontal field width to 128 µm. The command getmag reads the magnification and saves it to the variable *mag*. The variable *dacppm* is automatically created when a script is started and is the image resolution in pixels per microns. The quotient of the maximum digital resolution (4096) and the *dacppm* variable is the actual horizontal field width hfw. In the next steps the ratio between the current horizontal field width hfw and the target field width $sethfw$ is computed. This ratio is then used in the final step to set the new magnification using the 'setmag' command and the *mag* variable. The *mag* variable is similar to the *dacppm* variable created automatically and gives the magnification.

```
box -5,5, -1,1
circle 3, 3, 0, 2
line -5,-5, -1,-1
obox 5,-5, 1, -1
mill
clear
```

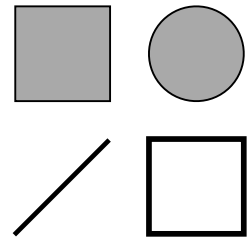

Figure 3.2: Example script to create four basic shapes. The resulting structures are shown on the right

options implemented into the 'runscript' program. Extra care must be taken not to damage the microscopes through errors in the code.

3.2 Structure variables and loops

In theory it is possible to define all structures in a script using absolute dimensions and positions. A more flexible approach is to parameterize the structures with key variables that correspond to important structure

characteristics. Than use a combination of loops and simple mathematic functions to create the structures through a logical expression. The main part of scripting logic comes from this combination of loops and mathematic operations. This allows automatic creation of ordered structures, e.g. an array of triangles. This approach increases the complexity of the script. However, once finished it decreases the time for prototyping greatly. Here the biggest factor are reduced optimisation times. The machine has a great cache of etching and parameter files available. These are calibrated for bulk applications. With increased resolution additional effects become important, e.g. thin natural oxide layers, proximity etching effects and redeposition[1]. These effects must be accounted for on a structure to structure basis.

Loops are one of the basic tools during this process. In the scripting environment a loop is created through a label or starting sequence and an 'if goto' trigger. A loop label is always indicated with a colon, e.g. 'loop1:'. When the if goto trigger is processed in the script, it checks a variable and, if true, goes to a specific label. The script then continues at this specific position. For example, when the 'if (n<>nmax) goto loop1' is processed, the value of n is compared with $nmax$ and, if they are equal, the script continues to process the commands after the position 'loop1:'. An example script using a combination of loops and variables is found in illustration 3.3.

1 These were especially important in the nanoantenna chapter. Hence these effects are discussed in detail there.

```
n=1
nmax=3
l=2
h=5
loop1:
box -n+l/2,h,n*l/2,h-l
h=h-3
n=n+1
if (n<>nmax) goto loop1
mill
clear
```

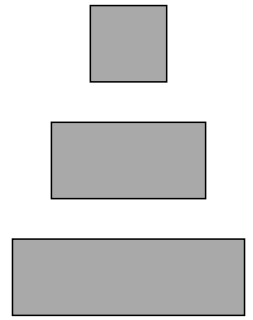

Figure 3.3: A sample script to create a series of blocks with increasing width. The script is shown on the left, while the resulting structures are shown on the right.

4 Small scale production of high precision optical components

After centuries of successful application in all fields of science, light microscopy still is an important analytical tool. The main reasons are ease of use and the ability to image samples without further preparation. In biology, for example, the ability to observe living organisms *in vivo* is of great interest and scientific value.

The possible applications of light microscopy have steadily been advanced over the recent years, and a variety of new light-based microscopes have been developed. The labelling of soft matter with fluorophores has opened a completely new field of microscopy with many applications in the life sciences. In addition, light microscopes were developed which have the ability to resolve beyond Abbe's law [Abb73]. These are coined super resolution microscopes.

One super resolution technique commercially available is structured illumination microscopy. For the microscope to successfully work with different colour labels, a special calibration sample is required. Normally, fluorophore bead based samples are used. However, these have some limitations, e.g. bleaching, random distribution of beads, number of fluorophores used simultaneously.

Nanostructuring allows the creation of high resolution optical components. Here, a nanotextured aperture is proposed. The aperture, in conjunction with colour filters, solves all problems posed by bead based setups. It is thereby possible to create a fully automated calibration process with a higher resolution and no limitations for the number of fluorophores used simultaneously.

The production of the required nanoapertures was first tried employing conventional lithographic methods. However, the size of the elements,

100 nm in diameter, and an aspect ratio near to one proved too challenging for simple lithographic approaches. The development of a sophisticated lithographic structuring setup, however, is not feasible for small scale production.

Focused ion beam microscopes can reach the required resolution easily. However, automated production of any scale is not the typical application for dual beam devices. The topic hence offered a great opportunity to explore the production capabilities of the device. A production and structuring add-on capable of patterning large areas was developed, and a workflow for small scale production created.

4.1 Misalignment in multi colour fluorescence imaging

Multi colour fluorescence imaging is a powerful imaging technique with many applications. In general, misalignments between different colour signals occurs. This mismatch must be corrected by software algorithms for the final micrograph to yield useful results. A focus lies on the OMX Blaze[1], as the nanoapertures produced are used in the shift calibration of this microscope.

The misalignment between different colour channels has multiple causes. There are errors produced by the chromatic aberrations of the lens systems. This leads to images with slightly different magnifications.

More advanced systems use multiple detectors for high speed simultaneous image acquisition of multiple colour channels. This significantly reduces the acquisition time per image. This setup is used in structured illumination fluorescence microscopes, e.g. the OMX Blaze. This microscope captures 15 images per micrograph per colour channel. Image acquisition time is already a bottleneck in these applications. Hence every enhancement in performance has a great effect on the resulting micrographs. Using more than one detector, however, results in additional mismatches between the colour channels. The light travels along different optical paths and thereby

1 A super resolution microscope employing multi colour fluorescence and structured illumination

mismatches between both channels occur. In addition, it is mechanically not possible to align the CCD chips of the detectors in a way that their pixels match each other. The effects of misaligned colour channels can be seen in illustration 4.1A.

4.1.1 Calibration samples

The mismatch alignments of multi colour fluorescence signals require calibration samples. For a landmark based algorithm features with characteristic properties are needed. These features must have a fixed position, a good spread over the sample and a distinct signal for every colour channel. In the past, bead based samples were used. These beads were labeled with multiple fluorophores and then attached to a substrate.

However, using fluorescent bead based samples is not the optimal solution. First, the fluorophores are prone to photo bleaching. This limits the maximum amount of time and/or number of pictures available for a single calibration. In addition, the beads are randomly distributed on the surface. This can introduce additional errors in the alignment. Aggregations and variance in fluorescence can add an extra noise to the automated image alignment process. Most bead based calibration processes require a manual landmark selection to work with high accuracy. This makes a fully auto-

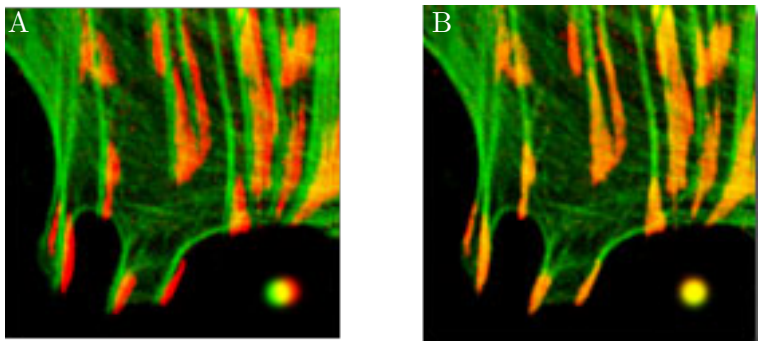

Figure 4.1: A: A mismatched image of a Tahr ovary cell stained with Alexa 488 and Alexa 568 B: The realigned image. [Oly12]

mated process impossible. Finally, in order to calibrate multiple spectral lines, for each colour a different flurophore must be present on the bead. This limits the final signal or decreases the resolution, depending on the scanning parameters. In addition, different calibration samples are needed for every combination of colours used in the system.

4.1.2 Nanotextured calibration samples

The approach presented in this work proposes a nanostructured shutter similar to the device used by Fore et al. [For07]. The nanoaperture is back illuminated with white light. A colour filter used in front of the aperture sets the colour. This creates a calibration source with distinct features of a uniform brightness. Through nanotexturing it is possible to ensure that the features are uniformly distributed over the calibration area. In comparison to fluorescent beads the nanoaperture method offers a higher brightness and is not affected by photo bleaching.

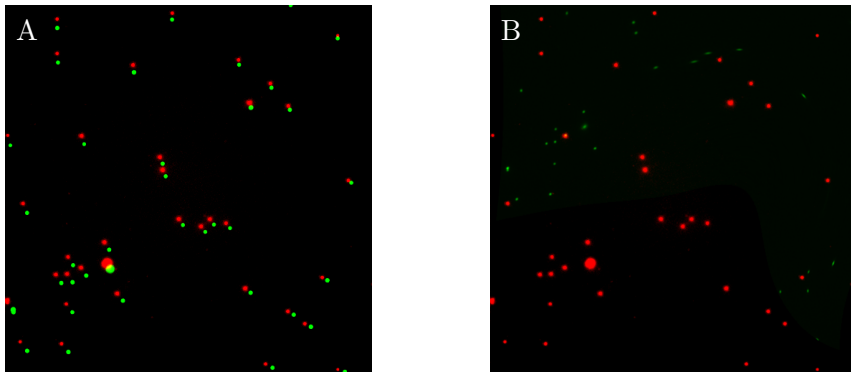

Figure 4.2: A: A picture of a alignment sample. The sample consists of beads with affiliated fluorophores. B: Realigned picture

4.2 Nanoaperture prototyping and production

The nanostructures should cover a large area in respect to the smallest elements. E-beam lithography can structure large areas, but struggles with the creation of small features with a high aspect ratio. On the other hand, a focused ion beam microscope is a great tool to drill small holes (100 nm) with high precision. Creating 22,500 of them, however, is not a default application and would require a lot of work using the manual user interface. In addition, the possibility of human error is high, significantly limiting the throughput and aperture quality.

Nevertheless, a focused ion beam device was chosen as a tool for the nanoaperture project. The automatisation possibilities with scripting software were explored for small scale production. The rapid prototyping capabilities of a focused ion beam device offered a significant reduction in process development time. For example, the hole size and form can be checked directly after a finished process without any additional process time.

A challenge was the area over which high definition features were required. Small structures are created under a high magnification, thereby limiting the maximum area. By decreasing the magnification the structuring of larger areas is possible. However, a decrease in magnification reduces the achievable resolution and structure quality as well. In lithographic setups this problem is solved by rasterising large elements and using a stage to connect high magnification write fields. The process is generally referred to as stitching. The focused ion beam device used for this process did not feature any stitching routines. Therefore, a script was developed which combines the automated creation of nanostructures with a self-written stitching algorithm.

4.2.1 Design

The layout of the aperture is shown in illustration 4.3. The overall size of the optical component is 15 mm times 15 mm. The basic design includes guiding lines and labels for the user. For readability under the microscope the writing is mirror inverted. The aperture functionalities are provided

by 100 nm diameter holes. These are arranged on a rectangular grid in the centre of the aperture and cover an area of 1.5 mm times 1.5 mm. The distance between two holes is 10 µm. In the middle a more densely packed area with a distance of 5 µm between the holes is created over an area of 50 µm times 50 µm.

4.2.2 Materials and substrate preparation

A 150 µm thick silica glass for optical components with a diameter of 50 mm was used as a substrate. This allowed to create five apertures on one substrate. The substrate was cleaned using an ultrasonic bath (Sonorex Ultra). There, it was first processed for 15 min in acetone and afterwards for 1 min in ethanol. The transfer between both cleaning fluids was done without drying the substrate in between. Afterwards, the fluids were removed from the substrate using pressurised nitrogen.

The guiding elements were prepared using a standard positive photolithographic process. A layer of photoresist (ARP 5350-25, Allresist GmbH) was spin coated with 5000 rpm onto the substrate. The resist was cured on a hotplate for 5 min at 110 °C. Substrates were exposed using a mask and an ultraviolet light source. The resist was developed in a 2:1 solution of developer (AR 300-50, Allresist GmbH) and water for 14 s. The substrates were then coated with 5 nm tantalum followed by a gold layer of 100 nm thickness using sputter deposition (CLAB 600, Leybold). The tantalum acts as a sticking layer, while the gold was chosen as a non optical transparent material with good ion milling qualities and chemical stability. Excess material as well as the resist mask were removed in a lift-of process using an ultra sonic bath with a remover (AR 300-70, Allresist GmbH). Afterwards, the substrates were washed again with ethanol and dried with nitrogen.

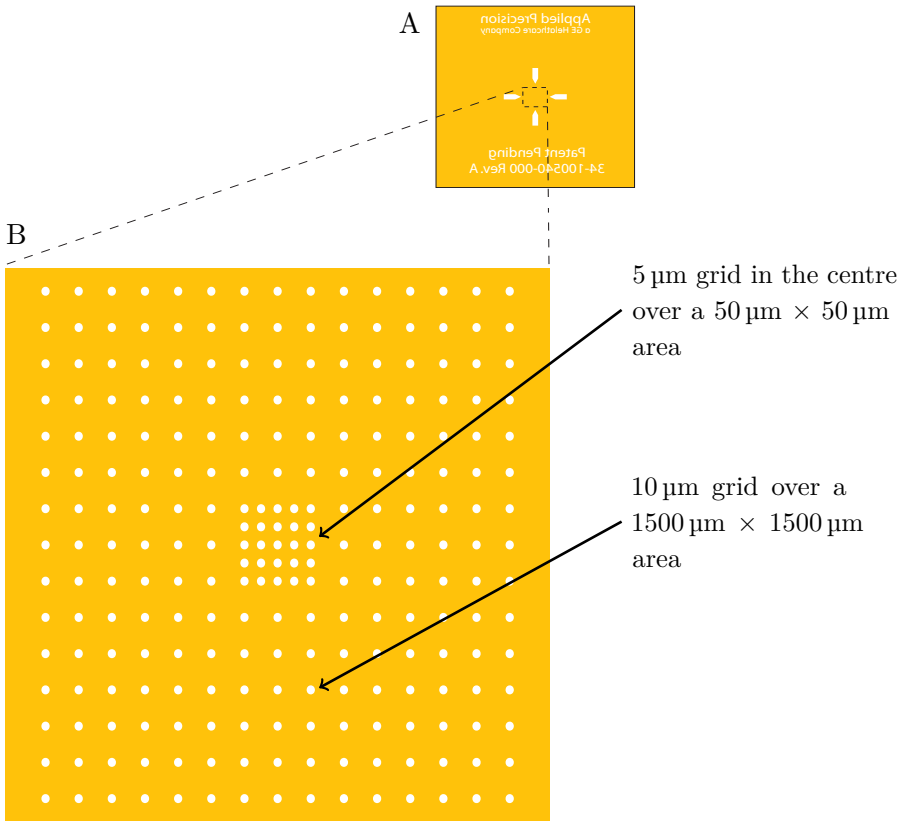

Figure 4.3: A: A sketch of the calibration mask. The writing is mirror inverted to be a readable under the microscope. B: A magnification of the central area of the aperture. The nanoholes are arranged in a rectangular grid. In the exact centre the grid has a higher density.

4.2.3 Focused ion beam milling parameters

For small features, especially holes redeposition and enhance edge etching effects are dominant factors[1]. Therefore, the calibration times and milling rates, predefined in the application file, cannot be used. Instead a series of tests was performed in order to optimise the shape of the hole and the general output result.

An ion beam current of 28 pA at 30 kV was used for the milling. This beam current was chosen for multiple reasons. It is possible to achieve the required resolution with a good margin of error. The nominal beam diameter is below 3 times the hole diameter. On the other hand, the current is high enough to achieve good mill rates. Milling a single hole takes around a half second time.

In the focused ion beam device the beam current is controlled by an aperture wheel. During operation this aperture is also sputtered by the ions. Production of the first batch of optical components was estimated to require about 500 h of continuous exposure.[2] Thereby a wear of the aperture was expected. For the 28 pA current two apertures are available, offering a replacement if needed.

The best results were achieved with 50 nm diameter, 2 µm deep circular structures. When milling small holes, redeposition becomes a dominant effect, because the angle under which sputtered atoms can leave the hole decreases with its depth. The holes achieved with theses parameters were 100 nm in diameter with very defined, steep walls. The high milling depth in respect to the gold layer ensured that no material was redeposition at the bottom of the holes.

Besides the main milling parameters beam astigmatism has a strong influence on the quality of the nanoapertures. Even slight errors in stigmation lead to elliptical structures. After a rough correction at small magnification, high resolution images are needed for fine tuning. Even at low beam energies the dose per area at high magnifications is high enough to modify

1 An in-depth discussion of enhanced edge etching and redeposition is found in chapter 5.3.1 and 5.3.3, respectively.

2 five hours per aperture, five apertures per substrate, 20 substrates in total.

the sample surface. This makes correcting the stigmation of the ion beam difficult. Therefore, as part of the automation routine, a small test area of dots is written and controlled with the electron beam to check for an effective calibration.

4.2.4 Scripting automatisation

For the production all structures needed to be created automatically. Only through automation, production using a focused ion beam device becomes viable. The most simplistic scripts have the following components: A settings header, a structure drawing part and finally an exposure part.

The structure drawing script, using the parameters for the nanoholes, is shown in illustration 4.4. It creates an array of 10 × 10 holes with a distance of 5 µm between them. The parameters for the holes are defined first. Then two loops are used to create an array of the necessary structures at specific locations. The mill commands as well as a global settings preamble are defined in other parts of the routine. The scripts shown in illustration 4.4 is used to define the elements for the densely packed centre of the nanoaperture.

A slightly modified version of this script is used for the holes around the central area. There, the distance between the holes is increased to 10 µm and the number decreased to 25. This makes it possible to keep the write field size constant.

4.2.5 Stitching routine

A challenge for the nanoapertures production was the scale difference between the holes and the entire patterning area. It is possible to work with large write fields, but then the resolution of the features suffers. The patterning engine has a limited digital resolution of 4096 points per line. This value divided by the write field width is the smallest possible distance the machine can process. In addition to this resolution decreasing aspect of low magnification, there is another problem with large structures. The patterning hardware only supports a limited number of points before an overflow warning is triggered. This either breaks the patterning process

```
setpatinfo 2, AU
d=0.05
xdist=5
ydist=5
m=0
mmax=10
nmax=10


loop2:
n=0
    loop1:
    circle (n*xdist) -22.5, (m*ydist) -22.5, d, d

    n=n+1
    if (n<>nmax) goto loop1

m=m+1
if (m<>mmax) goto loop2
```

Figure 4.4: Source code for a grid of nanoholes with a diameter of d=100 nm.

or prevents it from starting. For larges structures this is circumvented by increasing the beam energy. Changing the beam energy increases the spot size and thereby reduces the number of points needed to cover the same area. Alternatively, it is possible to set a blur. Blur is an artificial widening of the beam spot. This also reduces the number of patterning positions needed. For the nanoholes both options are not viable. The effective maximum beam diameter is already in use and the resolution offered by a high magnification required.

This challenge was overcome by implementing a stitching routine into the automation process. Stitching refers to segmenting a large write field into several smaller ones, which can then be patterned with a high magnification. This circumvents the resolution problems occurring for large patterns. The patterning point overflow is also solved by stitching. Through the segmentation process the number of points used simultaneously is decreased.

The stitching is implemented by adding an additional scripting level to the process. This script acts as a control layer. It calls subscripts for the nanostructures (previous chapter), starts the milling and moves the stage between exposures. Here the nanoaperture script is called first, then the starting position is exposed. Afterwards, the stage is moved to the right, again a pattern is written, then the stage is moved up and the pattern is written again.

The stitching script is based on four separate loops that control the movement of the stage. Each loop effectively controls movement in one direction (x,y,-x,-y). The loop variables are used as factors in stage move commands. For the nanoapertures the stage movement follows a rectangular spiral starting in the centre and extending outwards.

The stage movement has a limited resolution. Each step creates a small positional error. The stitching script uses a relative position system. Thereby the error accumulates and increases with each step. The error can be negated or at least significantly reduced with additional calibration structures. Using these, it is possible to create an absolute positioning system. However, using additional landmarks for the stitching would increase the complexity of the process and automation significantly. For the nanoapertures this level of accuracy is not required. In addition, the structures with the highest errors are at the outer borders of the overall aperture. The slight mismatch of these does not impact the quality of the calibration process in the super resolution microscope.

The stitching source code is shown in illustration 4.5. The code starts with defining the variables for the stitch move. Here u and v are intermediate variables used to create the spiral movement. The variable c counts the number of repetitions and thereby is directly connected to the overall area.

4.2.6 Process runtime improvements

The overall runtime of the patterning process is critical in making the production of components with a focused ion beam device viable. Therefore, the nanoaperture process was analysed for possible process time improvements.

It was found that the time needed to create the features in the software was up to six times greater then the time required for exposing them. Per

```
u=0
v=0
c=1
cmax=10

loopC:
  loopU:

    mill
    sleep 500

    getstagepos
    xnew=x+0.050
    stagemove x, xnew
    sleep 1000

  u=u+1
  if (U<>c) goto loopU


  loopV:

    mill
    sleep 500

    getstagepos
    ynew=y+0.050
    stagemove y, ynew
    sleep 1000

  v=v+1
  if (v<>c) goto loopV


  loopUm:

    mill
    sleep 500

    getstagepos
    xnew=x-0.050
    stagemove x, xnew
    sleep 1000

  u=u-1
  if (u<>-c) goto loopUm

  loopVm:

    mill
    sleep 500

    getstagepos
    ynew=y-0.050
    stagemove y, ynew
    sleep 500

  v=v-1
  if (v<>-c) goto loopVm
c=c+1
if (c<>cmax) goto loopC
```

Figure 4.5: Source code for the rectangular spiral stitching move

default patterns are generated new during each stitching step, then exposed and then cleared for the next stitching step.

To improve processing time, the segmentation for stitching was changed. By using the symmetry of the pattern it was possible to use the same set of once created features multiple times. The modified stitching process then became: Create a pattern, expose it, move to next location, expose the same pattern again. In effect the superstructure of the nanoaperture was created by the stitching routine and effectively controlled through stage movement. Through these changes the processing time was reduced from 300 min per aperture to 54 min.

4.2.7 Production interface

In order to produce multiple apertures on a single substrate an additional scripting layer was introduced. The layer acted as an intermediate between the focused ion beam microscope software and the scripting environment. The script was designed to allow a seamless integration with the existing focused ion beam software. After starting, the script enters a settings phase. In this phase the complete microscope control is still available to the operator. At this point the script can be ordered to read out machine variables and commit them to memory.

In order to transfer the relevant settings to the script the operator is tasked to drive to the substrate positions marked for patterning. There, last optimisations should be performed using the microscope software. For example, on large substrates the stage height for the eucentric distance can differ between both ends. After all settings needed for patterning at a position are checked, the scripting window is used to read out and save the position data. The operator can then search for the next pattern position. Saving these positions as points of interest in the focused ion beam software greatly reduces the time needed for quality control after a process is finished. After all position are transferred to the script an overview window is displayed. Here the positions can be checked and the automated process started.

4.3 Results

First prototypes were analysed in order to determine the available potential as calibration samples in the OMX|Blaze microscope. The prototypes were created with the focused ion beam device using the final parameters for the nanoholes. Theses prototypes were structured on smaller substrates with no additional lithographic preparation. The first tests only checked for visibility of the nanoholes under the microscope. The results were positive, as the nanoapertures were clearly visible and had evenly distributed brightnesses. Microscopy images of the finished apertures are shown in illustration 4.11. While the first prototypes were created semi manually, all subsequent samples were created fully automated.

4.3.1 Structuring results

The quality of the automated structuring process was analysed using the scanning electron microscope of the dual beam. Results of the automated structuring are shown in picture 4.6 and 4.7. The focused ion beam milling creates smooth holes with very steep walls. Through the scripting automation it was possible to create these holes in highly ordered arrays. It is, however, not possible to image the complete array of nanoapertures on a single micrograph. The low magnification of an overview picture does not offer the required resolution for 100 nm sized holes.

High resolution imaging was performed on single nanoholes. A high resolution picture of a single nanohole is shown in illustration 4.8. For these images the immersion imaging mode was used. The immersion modus offers a detector setting labeled "down hole visibility". With this setting it is possible to take micrographs of the insides of the nanoapertures. The focused ion beam process milled through the gold layer and into the substrate. In the centre a high depth region with a diameter of 72 nm is visible where even substrate material was removed. The outer rim of the nanoaperture is visible as well. Its diameter is 120 nm. Between the outer radius and the deep milling crater in the centre some gold is left. It is not possible to measure the thickness of the gold layers left, or make any assumptions on the optical transparency of the material between both radii.

However, the resulting pictures are clear indicators that nanoapertures with a diameter below 100 nm were successfully created.

4.3.2 Focused ion beam automation

In order to increase throughput, five apertures were created on a single substrates. Therefor a 50 mm diameter substrate was used. The substrate was first prepared lithographically creating five sets of guiding structures simultaneously. The design for the guiding structures is shown on page 27. A photomask was created for parallel processing of these guiding structures and is shown in illustration 4.9. A finished substrate is shown in illustration 4.10.

The high resolution features were created with the focused ion beam device. After loading the prepared substrate in the dual beam device and performing the initial alignments, the scripting routines allowed structuring of all five apertures automatically without further instructions from the operator. The focused ion beam processing of the system finished within in about 5 h. The operator was only required for one hour, with most of the time consisting of venting and pumping the vacuum chamber. This automation allows it to create small batches of 20 completely finished substrates (100 apertures) in 2 weeks.

4.3.3 Calibration using nanostructured shutters

The nanoapertures are successfully used for colour channel calibrations. For the OMX|Blaze it was possible to implement completely automated alignment routines. This is possible because the nanoaperture features have exactly known positions and a uniform brightness. Measurements and calibration results were provided by Thomas Huser and are based on a software developed at UC Davis.

For the calibration, pictures for the different colour channels are taken. The alignment procedure subsequently transforms one image into the other, looking for the best fit. The resulting parameters are then used to transform other images taken with the microscope. A sample alignment is shown in picture 4.11.

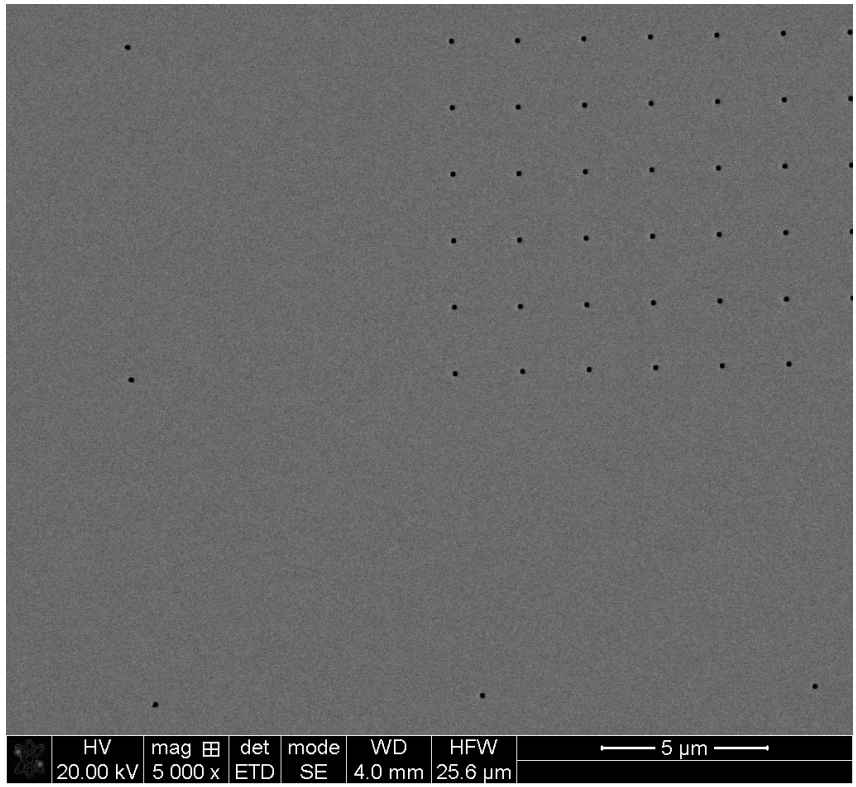

Figure 4.6: Scanning electron picture of nanoapertures created with a focused ion beam. The micrograph shows the edge of the higher density holes.

The automated alignment has a high resolution and repeatability. From the images in illustration 4.11 an alignment resolution of 0.056 pixels ± 0.019 pixels could be determined. This corresponds to an average alignment accuracy of 4 nm. The detailed results of alignment calculation are visualised in graphic 4.12.

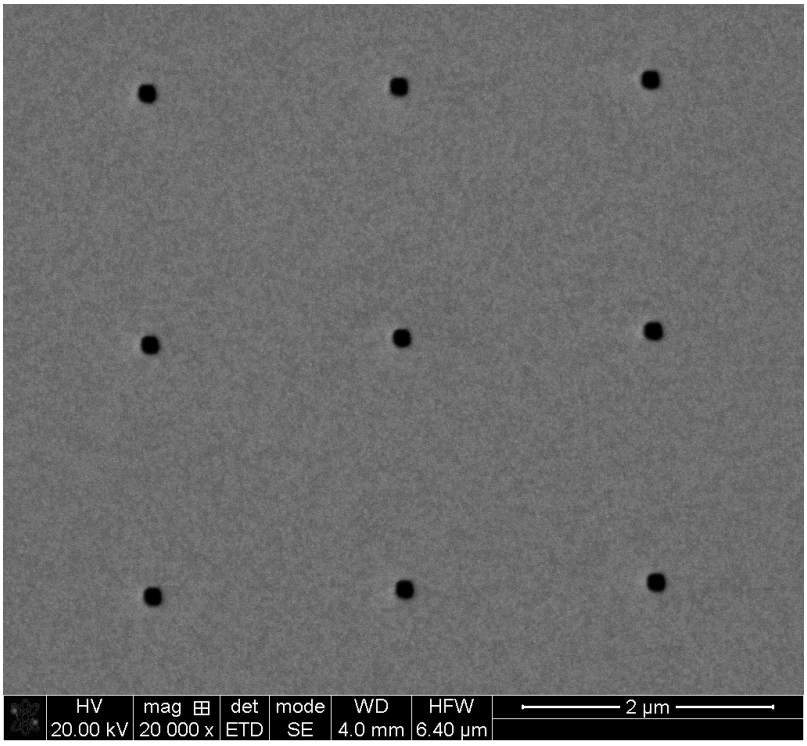

Figure 4.7: Scanning electron picture of nanoapertures created with a focused ion beam.

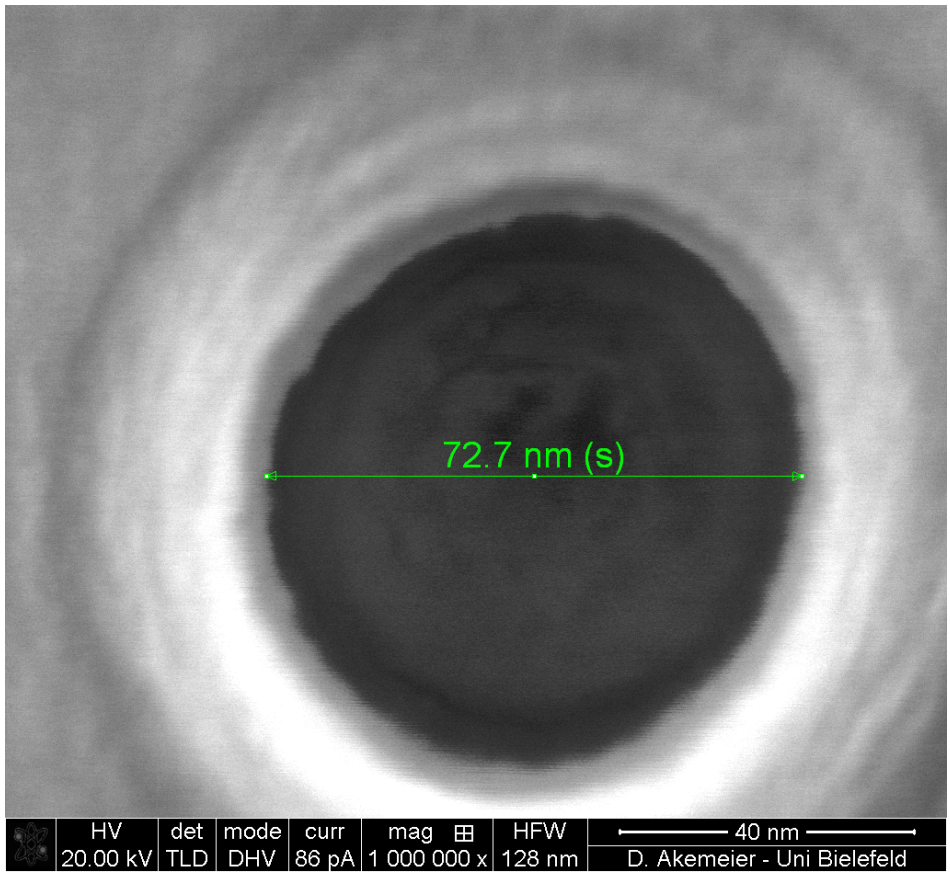

Figure 4.8: Scanning electron picture of a nanohole created with a focused ion beam. The micrograph was created using a "down hole visibility" mode. The inner area, where a deep mill into the substrate is visible, has a diameter of d=70 nm. The outer rim has a diameter of d≈120 nm.

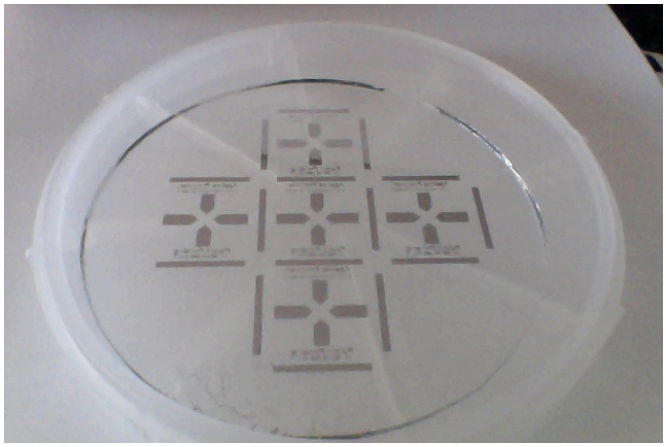

Figure 4.9: Alignment mask for the multiple apertures.

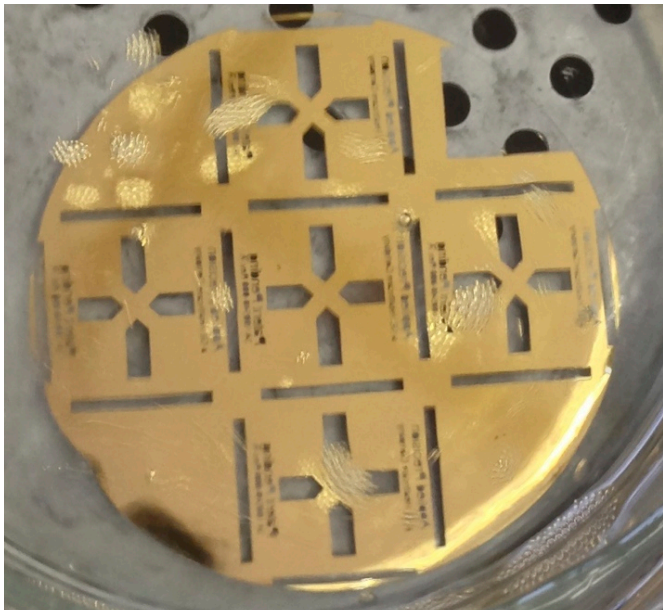

Figure 4.10: A finished substrate, photographed during the final cleaning step.

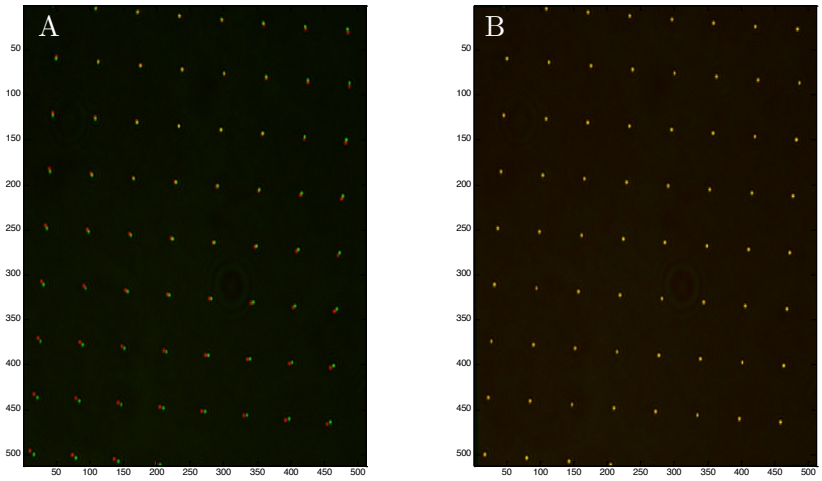

Figure 4.11: A: A superposition of images for two different colour channels attained with the nanotextured calibration structures. B: The overlaid images after the automated calibration routine.

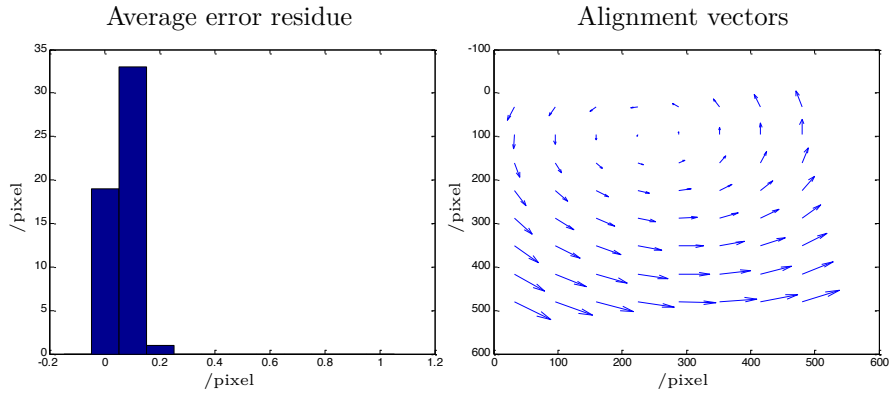

Figure 4.12: The diagram on the left shows the accuracy of the alignments and the spread of its error. The accuracy can be determined as 0.056 pixels ± 0.019 pixels. The corresponding resolution is 4 nm. The diagram on the right shows the corresponding alignment vectors.

4.4 Summary and Outlook

The optical quality of components was always a limiting factor in light microscopy. While the quality of macroscopic materials (lenses, mirrors) has already reached its maximum through the usages of high precision machinery and deposition techniques, the improvements offered through nanotextured components are not yet fully explored. The prototyping and production of nanotextured materials is still challenging and expensive. Up to now it is only feasible for large quantities, thereby limiting the applications of custom built optical components.

As part of this work it was demonstrated that for prototyping and small scale production a dual beam device is a viable alternative to lithographic structuring. However, in order to use the focused ion beam device for this new purpose some customisations are necessary. These were developed in a scripting environment and are explained in this work. While my work presented here focusses on aperture production, the overall framework (stitching, integration with imaging software) is easily transferable to other applications.

With the developed scripting environment it was possible to create nanotextured apertures each consisting of 22,500 holes with 100 nm in diameter. The apertures are an integral part of the calibration process in a structured illumination microscope from Applied Precision the OMX|Blaze. The microscope uses lasers of various wavelength for excitation and can thereby take, in combination with the structured illumination setup, super resolution images of more than one fluorescence signal. A calibration is needed to correct for the occurring mismatch between different colour channels. For that, the aperture is illuminated with white light and a filter is used to set the desired colour. The calibration transformation is then computed from the resulting images.

This new approach offers many advantages over the state of the art method using fluorescent bead based calibration samples. They are not affected by bleaching and thereby can be used for long exposures, yielding higher resolution images. The nanoapertures are made out of non oxidising materials and can be safely stored for long times without problems. Through nanotexturing the features are homogeneously distributed and

have a uniform brightness distribution. Additionally, the colour signal is produced through a filtered white light source. There is no limit to the number of colours which can be calibrated at the same time. In addition, no specialised samples are needed for each combination of fluorescence markers used. The use of nanostructures increases the overall resolution of the alignment process when compared to bead based alignments. Finally, by having ordered features in comparison to randomly distributed beads, it is possible to implement a fully automated colour calibration routine. These routines are implemented in the OMX|Blaze microscope. There, a resolution of 4 nm is reached.

The focused ion beam device offers a great platform for rapid prototyping. The ability to create patterns and analyse them in one device decreases the development time significantly. Creating all structures through parameterised scripts gives an additional fine control during the optimisation process and allows for easy reproduction of once attained parameters. Focused ion beam patterning allows the creation of nanotextured elements with a very high resolution. The tie-in with a stitching routine makes it possible to stretch these pattern over large areas. Through scripting automatisation the production of medium sized batches (100 apertures) becomes viable.

The big advantage of focused ion beam based production over traditional lithographic processes is its tight interlocking with prototyping. Techniques developed for creating prototypes are directly transferable to the production process with very little modifications. This greatly reduces the development time and thereby costs. Thus, it becomes viable to create highly specialised elements for various applications and even tailor the components specially to the user's needs. Here a focused ion beam may become similar to a 3D printer in traditional prototyping. While 3D printers start to revolutionise traditional prototyping and production - a specialised dual beam device may offer the same advantages, but with nanometer resolution.

5 Focused ion beam structured nanoantennas for higher harmonic generation

The development of coherent light sources (lasers) was paramount in opening up new technological and scientific fields, e.g. compact discs and confocal laser microscopes. For nearly all applications a shorter wavelength means higher resolution or higher data density. The transition from compact discs to blue-ray discs is a straight forward example. Modern excimer lasers have achieved wavelengths down to 128 nm [Lor79, Bas02]. In order to achieve coherent radiation of even shorter wavelength, frequency doubling and higher harmonic generation can be used [McF05].

Frequency doubling was first reported by focusing a high energy rubidium laser on quartz crystals [Fra61]. Later, higher order harmonics generation in noble gases was shown using a CO_2 Laser [Bur77]. Since then higher harmonic generated radiation has been used in a wide range of technical applications. Shorter wavelengths, achieved by higher harmonic generation, lead to shorter pulse durations and open up applications in the attosecond regime [Dre01]. This temporal resolution can be used in new types of metrology, e.g. measuring electron interactions [Uib07]. Higher harmonic generation can be used as coherent light sources in the extreme ultraviolet spectrum, for example in high precision spectroscopy [Ude02]. Here, pushing into the extreme ultraviolet spectra could increase the resolution by one order of magnitude [Kan10]. This method is still limited by poor conversion rates and the required current densities ($> 10^{13}\,\mathrm{W\,cm^{-2}}$) for the higher harmonic generation. One way to overcome these problems are sophisticated laser setups including external enhancement cavities [Goh05].

An alternative strategy was proposed by Kim et al. [Kim08], which

used nanotextured plasmonic antennas as a tool for generating extreme ultraviolet light. Using the local field increasing properties of antennas, energy densities in the range needed for higher harmonics generation could be obtained directly from a laser resonator. The size of optical antennas needs to be considerably below the size of the wavelength, for a 820 nm Ti:sapphire laser this is approximately 160 nm. The antennas are bow tie shaped and require a gap with a structure width of at least 20 nm between the wings. This makes lithographic structuring of those elements challenging. However, all structures can be created through surface milling, using a dual beam device.

This chapter describes the steps necessary to create these structures - the considerations, limitations and the interplay between fast prototyping methods and mathematical simulations required for optical nanoantenna structuring with a dual beam device.

5.1 Theoretical Background

5.1.1 Basic light matter interactions

In solids the basic interaction propagation of light is described by the macroscopic Maxwell relations [Jac02]. In SI units they can be written as

$$\begin{aligned} \nabla \cdot \mathbf{D} &= \rho_{\text{ext}} \\ \nabla \cdot \mathbf{B} &= 0 \\ \nabla \times \mathbf{H} &= j_{\text{ext}} + \frac{\partial}{\partial t}\mathbf{D} \\ \nabla \times \mathbf{E} &= -\frac{\partial}{\partial t}\mathbf{B}. \end{aligned} \tag{5.1}$$

Here $\mathbf{E}$ is the external electric field, $\mathbf{D}$ the displacement field, $\mathbf{B}$ the external magnetic field and $\mathbf{H}$ the magnetising or auxiliary magnetic field. The electric vector fields $\mathbf{E}$ and $\mathbf{D}$ are connected through the polarisation

P, with

$$\mathbf{D} = \varepsilon_0 \mathbf{E} + \mathbf{P}, \tag{5.2}$$

with ε_0 being the vacuum permittivity. Similar dependencies exist for magnetic fields through the magnetisation **M** and the vacuum permeability μ_0. Here the relevant equation is

$$\mathbf{H} = \frac{1}{\mu_0}\mathbf{B} - \mathbf{M}. \tag{5.3}$$

If polarisation and magnetisation can be understood as a form of material response, the susceptibility tensors χ_E and χ_M can be used to describe their relations with the vector fields

$$\begin{aligned} \mathbf{M} &= \chi_M \mathbf{H} \\ \mathbf{P} &= \varepsilon_0 \chi_E \mathbf{E}. \end{aligned} \tag{5.4}$$

When assuming a linear response the equations (5.2) and (5.3) can be further simplified using equations (5.4) to

$$\begin{aligned} \mathbf{D} &= \varepsilon_o \varepsilon \mathbf{E} \\ \mathbf{B} &= \mu_0 \mu \mathbf{H} \end{aligned} \quad . \tag{5.5}$$

Magnetic materials have a high AC resistance and are therefore not suitable as optical antennas. Hence, only non magnetic materials are considered, leading to a $\mu = 1$. Therefore, magnetic influences are omitted in the following paragraphs. This is discussed in detail in section (5.9).

5.1.2 Higher harmonic generation with intense laser fields

The effect of higher harmonic generation only occurs for high laser field strength. For strengths above $> 10^{13}\,\mathrm{W\,cm^{-2}}$ the linear response approximation is no longer valid (5.4). In this case, higher order influences of the

susceptibility $\chi^{(2)}$ must be considered [Boy02]. The induced polarisation can be written as

$$P = \varepsilon_0 \chi^{(1)} \mathbf{E} + \varepsilon_0 \chi^{(2)} \mathbf{E} + \varepsilon_0 \chi^{(3)} \mathbf{E} + \varepsilon_0 \chi^{(4)} \mathbf{E} + \dots \quad . \tag{5.6}$$

Here, ε_0 is the vacuum permeability and $\mathbf{E}$ the electric field of the laser pulse. This perturbative approach works well for the description of second and third order harmonic generation.

For higher laser intensities the predicted conversion rates no longer match the experimental results. A typical higher harmonics spectrum is shown in illustration 5.1. The first section is described by the perturbative approach using equation (5.6). The plateau (region 2) and the cut off (region 3) can be described using a semi classical model.

This semi classical model was first proposed by Corkum [Cor93]. It is based on the assumption that electrons removed by a strong laser field have a high probability to recombine with their originating atoms. The bound electron is evaluated quantum mechanical. After tunnel ionisation from the atom, a classic approach is used to determine the evolution of the electron wave packet. For simplicity the laser field is also considered classically. The generation process is divided into three subprocesses: ionisation, acceleration and recombination.

The laser field deforms the atomic potential and lowers the coulomb barrier. Thus, the possibility for tunnel ionisation increases. The tunnel efficiency is dependent on the local field amplitude, with the highest ionisation rate at maximum amplitude. Directly after ionisation the electron wave packet follows the direction of the laser field away from the atom. Half an optical cycle later the electric field changes direction and the electron is accelerated back towards its parent nucleus. The energy acquired by the electron is given by

$$U_p = \frac{e^2 \langle E^2 \rangle}{4 m_e \omega^2} \quad , \tag{5.7}$$

with e the electron charge, m_e the electron mass and ω the laser frequency. If the electron recombines with its parent nucleus a bremsstrahlung like

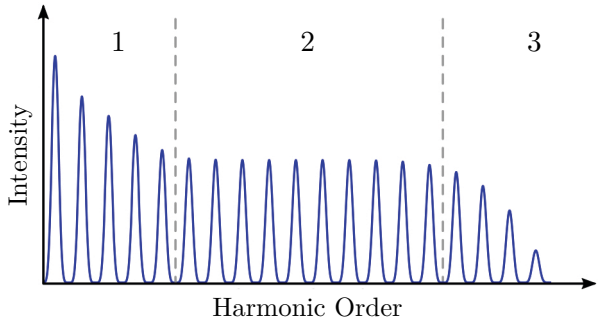

Figure 5.1: A typical higher harmonics spectrum. Section one depicts the perturbative regime, section two the higher harmonic plateau and section three the cut off.

radiation is emitted. This radiation occurs at odd harmonics of the fundamental laser frequency. The maximum electron energy can be calculated to $3.17U_p$. The maximum photon energy is

$$E_{max} = 3.17U_p + I_p \quad , \tag{5.8}$$

with I_p the atom binding energy. These results fit well with empirical measurements, where U_p lies between 3.0 and 3.2 [L'H93, Sch97].

5.2 Designing optical antennas for higher harmonic generation

Antennas in the radio and microwave regime are a well known field with many applications [Joh84]. Electromagnetic waves excite standing waves in the antenna's conductors. The best energy transfer takes place near the resonance frequency. In order to tune into the resonance frequency, the wavelength should be on the order of two times the antenna length $\lambda = 2 * d$. However, the resonance frequency is slightly shifted to $\lambda = 0.95 * 2 * d$ due to dampening.

At optical frequencies this effect is much more pronounced. The elec-

trons can not instantly follow the changing field. This leads to a greater dampening effect and thereby decreases the resonance length of the antenna significantly. In addition, the antenna material affects the final resonance frequencies, e.g. the resonance length of a gold antenna excited with a 600 nm laser is at approximately 140 nm.

The basic design of the bow tie antennas is sketched in illustration 5.2. This specific antenna is composed of two triangular wings with a length of l and an opening angle of α. Both tips face each other with the distance or gap g between them. This specific antenna design acts as a field concentrator. The antenna collects the laser field and can create a very high field strength (above $10^{13}\,\mathrm{W/cm^2}$) between its tips, if the parameters, especially g, are chosen correctly.

Starting from the basic design, finite element simulations were performed by Pfullmann et al. at Hannover University [Pfu12]. The simulations were used to determine resonance length of specific antenna/laser configurations. In addition, the simulation gave information about the size of possible field enhancements between the tips. Working from these results, first configurations of the antennas were proposed and further tested. The two driving factors for optimisation were maximum field enhancement and technical feasibility.

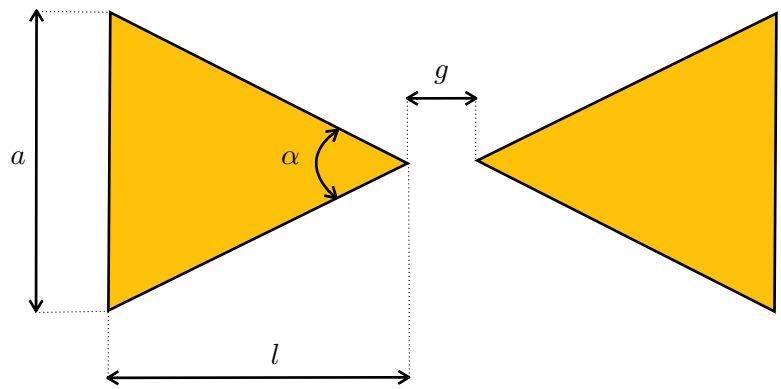

Figure 5.2: A simplified picture of the design for the nanoantennas.

5.2.1 Thermal stability

The maximum field strength attainable with a bow tie shaped nanoantenna is dependent on the resonance of the antenna with the driving field and the overall excitation power used. However, the energy deposited by the laser can lead to thermal destruction of the antenna. Numerical simulations of the nanoantennas were performed in order to optimise the thermal stability in regards to the field enhancement obtained.

In general, for resonant excitation with incident intensities above $10^{11}\,\mathrm{W/cm^2}$ the antennas start to melt. The antennas are excited with short pulses, so that, the deposited energy is only sufficient to melt small parts of the antennas. The substrate then acts as a cooling medium and rapidly cools the antennas back to environment temperature. However, even picoseconds in liquid phase are enough to modify the structure of the elements [Koc05]. This modification decreases the antenna performance.

Field enhancement simulations with a fixed excitation wavelength were performed. In the first simulations only the resonance length of the antennas was varied. A plot showing field enhancement for different antenna lengths is shown in illustration 5.3. In this case the resonant antennas show the highest field enhancement effects.

Resonant antennas are more susceptible to thermal destruction. Another set of simulations, taking into account the maximum excitation energy before thermal damage occurs, was carried out. The results are shown in illustration 5.4. In this case slightly out of resonance nanoantennas show a higher maximum field strength. They are therefore more technologically viable. For an excitation wavelength of 600 nm the optimal antenna length was found to be 160 nm, as opposed to the resonant length at 140 nm.

5.2.2 Materials for optical antennas

When considering materials for nanoantenna applications different material properties must be considered, such as resistance and chemical stability. In addition to heating and dampening characteristics, ohmic losses should be as low as possible. For high AC environments, like coupling light into nanoantennas, the resistance of the materials is determined by the skin

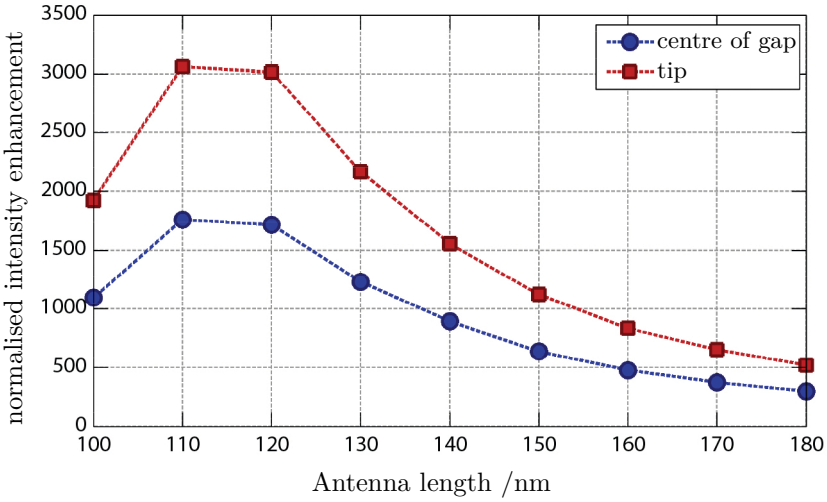

Figure 5.3: The normalised intensity enhancement within the feed gap of bow tie shaped antennas over the antenna wing length or resonant length carried out at a fixed excitation energy. The antennas resonant with the excitation wavelength show the highest effect [Pfu12].

depth. In general, the skin depth is given by

$$\delta_{\text{skin}} = \sqrt{\frac{\rho}{\mu f}}, \tag{5.9}$$

with ρ the resistivity, μ the magnetic permeability and f the frequency. Due to the strong influence of the magnetic permeability all magnetic materials are discarded ($\mu = 1$). For materials at optical frequencies the skin depth can then be written as

$$\delta_{\text{skin}} = \frac{c\sqrt{\text{Re}(\varepsilon(\omega))}}{\text{Im}(\varepsilon(\omega))} \qquad \text{[Mai07]}. \tag{5.10}$$

A high real part increases the reflectivity and thereby reduces possible losses. More important, however, is a small imaginary party, which accounts

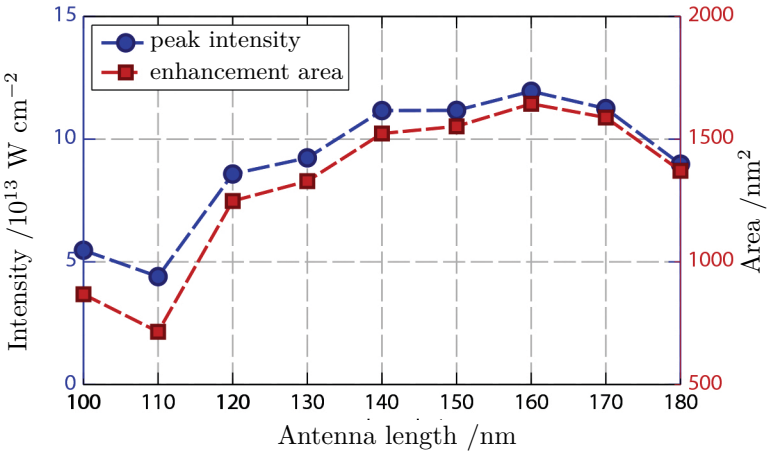

Figure 5.4: Intensity enhancement in the feed gap versus antenna wing length. This calculation takes the thermal stability of the nanoantennas into account. Non resonant antennas have worse conversion rates, but they can sustain a higher excitation intensity without taking damage. An optimal antenna length was found at 160 nm wing length [Pfu12].

for a low ohmic dampening. The occurrence of plasmonic resonance is also dependent on the ohmic dampening. Optical constants for most noble metals are found for example in [Joh72].

First, the laser excitation was considered. 630 nm laser are widely available therefore this values was chosen as a starting point. In this excitation regime gold, copper, silver and aluminium are suitable materials. Gold, copper and silver have very similar characteristics, with copper having slightly better conducting properties and silver having a better reflectivity.

The chemical stability of the antenna material is important as well. Silver and copper have very good dielectric characteristics, but they form natural oxide layers. Due to low skin depth at high frequencies these oxide layers may create additional dampening effects. In addition, oxide layers may be problematic in the structuring process. Oxides and metals have very different etching characteristics and rates. Hence, the fine-tuning of a structuring process is much more challenging for a compound system, which

can lead to a decreased final resolution. Therefore, gold was chosen due to its superior oxidation resistance.

Aluminium was the other interesting material, which in theory would be able to yield similar results to gold. Aluminium forms a thin oxide layer, but this layer is only several atoms thick and should not negatively impact its optical properties.

Structuring tests were performed on gold and aluminium layers in order to examine the ultra high resolution structuring properties. Here, gold showed the superior ion milling properties.[1]

5.2.3 Sticking layers and substrate material

For many lithographical processes additional sticking or sacrificial layers are needed. Normally a thin chrome or tantalum layer is used to increase the mechanical stability of the gold thin films. Otherwise the gold layer dissolves during the structure transfer step.

The focused ion beam patterning process proposed for the nanoantennas is a complete direct write process. Therefore, no photoresist is used during any part of the structuring. Hence, no sacrificial layers are needed.

Omitting the sticking layers has additional advantages. Each further component would create an additional source for inhomogeneous milling, thereby reducing the overall resolution. In addition, the sticking layer could hinder the heat dissipation into the substrate.

Another aspect of the materials selection process was the substrate material. The high laser loads create a significant amount of heating in the nanoantenna. Hence, a material with a high heat conductivity is required. In addition, the substrate must be an insulator and transparent to the excitation laser.

Therefore, artificial sapphire was chosen as a substrate material. Sapphire is an excellent insulator with a high heat conductivity. Single crystalline (001) polished substrates are commercially available from Crystek and were subsequently used.

1 The thin natural oxide layer of aluminium probably hindered a homogeneous milling process and thereby degraded the structure quality.

5.3 Focused ion beam structuring of optical antennas

The properties of optical antennas are strongly dependent on the absolute size of the elements. Size changes of 10 nm in the antenna length have a strong effect on the resonance and hence the resulting signal. In addition, a gap with a structure width of at least 20 nm is required for the field enhancement effect. Focused ion beam devices have a good milling resolution. Nevertheless, the resolution required for nanoantennas is close to their resolution limit. This high resolution can only be achieved through high magnification, limiting the field of view and the overall patterning area. The lasers used for excitation on the other hand have a spot size between 10 µm and 20 µm. In order to get measurable effects an entire array of antennas must be created with an equal or larger size. For this, approx. 6000 bow tie antennas must be created with nanometer resolution. Automation scripting was proposed as a solution. A scripting routine offers the ability to structure larger areas with reproducible quality and high resolution.

The nanoantennas are small gold triangles of 160 nm length with a 20 nm gap between them. Creating the triangles separately would be a straightforward task. They could be directly milled out of the substrate material. First tests were performed by creating triangular patterns through a scripting routine. These scripts used 'box' and 'polygon' commands to create a milling pattern which removed material until a triangle was left. For first tests two of theses triangles with tips facing each other were created. In the scripting environment it is possible to successively change the distance between those two. However, with these first approaches it was impossible to reliably create 20 nm gaps. The first results had gaps of around 100 nm and are shown in illustration 5.5.

In this chapter, ion beam milling of small features is discussed in detail. Afterwards, the machine and scripting commands used for patterning are analysed. Specific scripts are developed to fine control the exposure parameters and thereby increase the overall resolution of the patterning process.

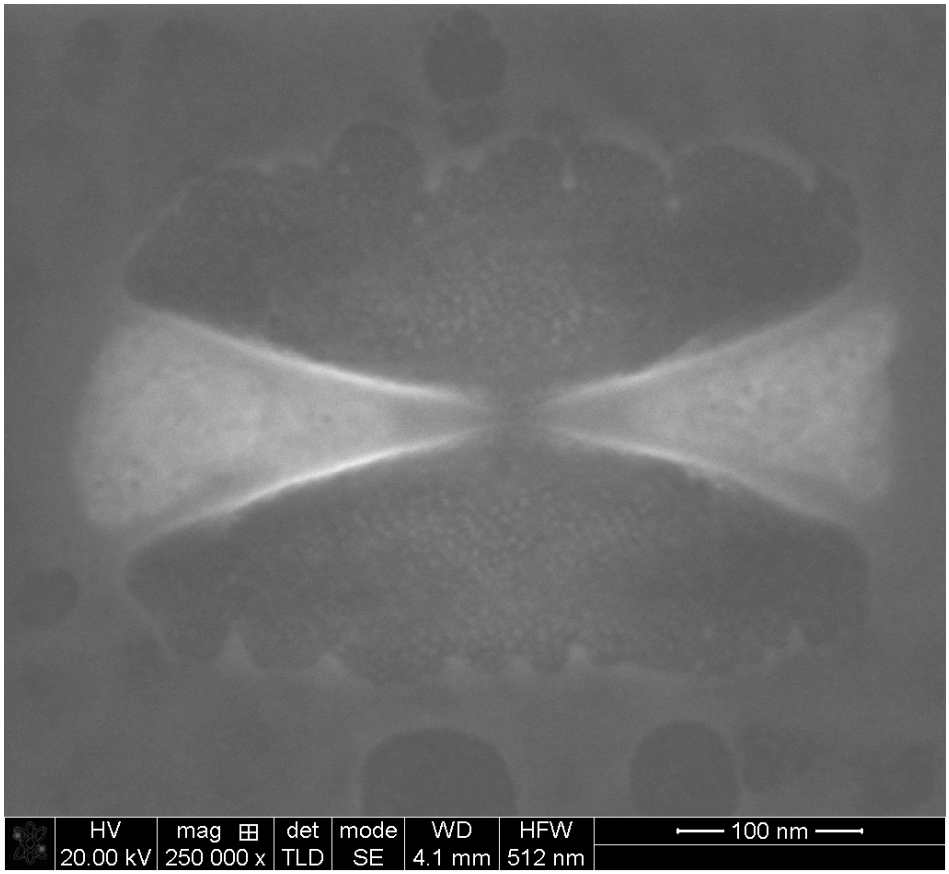

Figure 5.5: A scanning electron microscope image of one of the first bow tie prototypes. This bow tie was produced using basic 'box' and 'polygon' commands only.

5.3.1 Enhanced edge milling

Focused ion beam patterns are created by scanning a surface repeatedly with the ion beam. During each pass surface atoms are sputtered by the beam ions. For homogeneous materials and large areas the amount of sputtered material depends only on the dose per area[1]. On the other hand, for small features additional effects have to be taken into account. One effect governing the mill rate is strongly dependent on the effective cross-section and/or the angle of incidence between the beam ions and the surface, referred to as enhanced edge etching. For the influence of this effect first the differences in milling rate between a perpendicular and grazing incident beam are considered. Second, the implications are transferred to small features.

The milling process is simulated through an atomistic collision model. There, the interactions between the surface atoms and the projectile ions are defined by universal two body potentials [Wil77]. However, not all ions interact with the first layer of surface atoms. Hence, a fixed free path length proportional to the target material density is used. Upon impact with a surface or bulk atom the projectile ions set off collision cascades. A hit bulk atom is then again accelerated within the solid and collides with other bulk atoms. This process continues until the initial energy of the projectile is dissipated through inelastic processes. This may result in an atom leaving the solid, if its energy is still greater than the binding energy. However, only atoms near the surface (free path length) have a chance of leaving the solid. The mean direction of the collision cascades is dependent on the incident angle of the projectiles.

Monte Carlo simulations were performed with the TRIM software [M̈84]. Here, the trajectories of gallium ions, with an acceleration voltage of 30 kV within a gold surface layer, were calculated. For the simulation shown in illustration 5.6A a perpendicular angle of incidence was used. A second simulation for a grazing incident angle projectiles (10°) is shown in illustration 5.6B. For both simulations, 1000 trajectories were calculated. The greater spread of ions near the surface of the material is clearly visible

1 The dose is dependent on the beam current and the integrated exposure time.

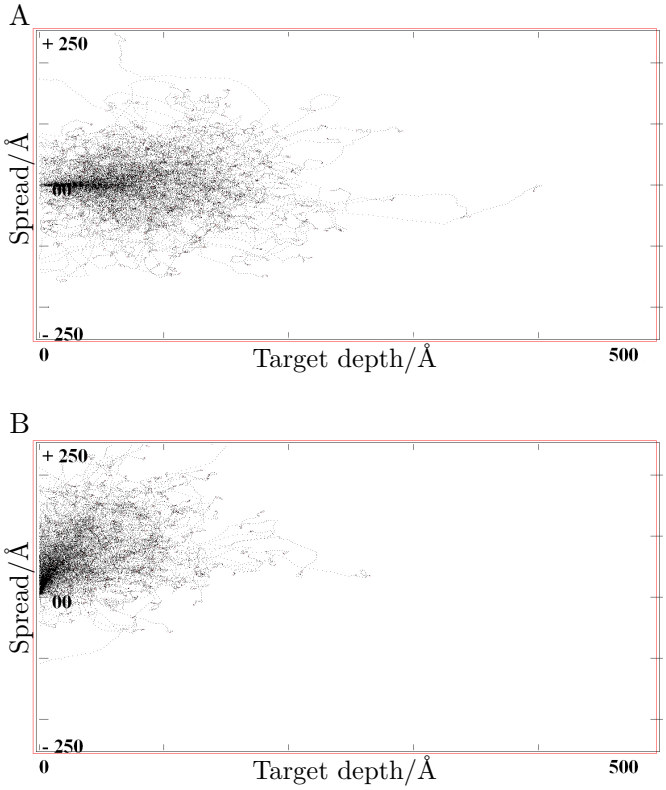

Figure 5.6: Monte Carlo simulations of projectile ion trajectories in gold. The projectile ions for this simulations had an acceleration voltage of 30 keV. The data in plot A was calculated for ions hitting the surface perpendicular, while the ions in plot B had a grazing angle of 10°.

in illustration 5.6B. This already indicated a higher sputter rate. The actual increase in mill rate was also simulated with the TRIM software. Data from the simulations gave a 14 times increase in sputter rate for a specimen tilt of 10° between the surface and the incident beam.

A similar effect is observed when milling features. The mill rate at the edge of a feature is higher than the mill rate for the bulk material in general. Feature milling is depicted in illustration 5.7. When the patterning beam is at the edge location, the effective angle between the incident beam and substrate decreases. Subsequently, the sputter rate increases at feature edges. The effect is similar to the results from the tilted beam simulations. This increase in sputter rate leads to observable changes in finished structures. More material is removed than defined by the structure pattern. The effect is more dominant for small features. There, the edge comprises a greater part of the overall structure area/volume.

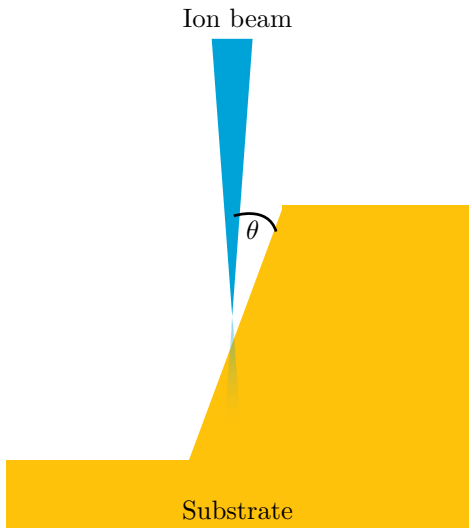

Figure 5.7: Milling of a feature edge with an ion beam. The effective angle θ between the substrate and the ion beam at the edge is very shallow.

For the nanoantennas the patterning was optimised manually. A series of test samples was milled and after each sample the structure quality was

analysed with the scanning electron microscope. Afterwards, the parameters were changed by small amounts until the result was optimal.

5.3.2 Proximity Effect

The proximity effect is a well known complication in conventional lithography. Due to dispersion or inter material scattering, resist next to exposed areas is exposed as well. The actual dose declines with the distance from the exposed area. In conventional lithography the proximity effect becomes a problem when the proximity dose is high enough to expose the resist.

For ion beam direct write lithography a similar effect can be observed. Therefore, the current distribution within the ion beam must be analysed. The ion beam has a gaussian energy distribution and broad tails with a slower decline in intensity [War87, Kub87]. The beam diameter corresponds to the gaussian portion of the current density.

The beam tails are the reason for a small ion dose outside off the actual beam diameter. This leads to slight over-milling at all structure borders and a proximity effect like behaviour. This effect can be amplified through enhanced edge milling described in the previous chapter.

5.3.3 Redeposition of material

During focused ion beam milling material is selectively sputtered from the sample. Not all removed atoms have a trajectory that leads them away from the sample. These atoms have a chance of hitting the sample surface and can reabsorb there. This effect is called redeposition.

Redeposition is a problem in ion beam patterning. The reabsorbed atoms can degrade edges, form shorts between conductors or connect freestanding structures. Though redeposition is an isotropic process, the effect on the final structure is dependent on the layout. For example, when milling holes, redeposition increases the mill time, because material is not removed very efficiently. In case of the nanoantennas, redepositioned material in the gap between both wings could destroy the field enhancement effects.

The effects of redeposition are also dependent on the actual sequence of the milling application. When for example two squares next to each

other are milled sequentially, redepositioned material would be found in the first but not in the second square. While material is redepositioned at the second structuring site, it is removed together with other material when the site is milled. Material redepositioned by the second milling is not removed from the first site, because the milling has already been finished at the first location.

For most processes, the effects of redeposition can be reduced by milling with parallel mode enabled. In parallel mode, all defined patterns are sputtered simultaneously, thus removing any redeposition material directly. In a parallel milling setup only the effective mill rates change slightly.

First tests, however, showed that the bow ties could not be created using the parallel patterning mode. Patterning in parallel mode lacks the fine control options needed to correct other structure degrading effects, e.g. the enhanced edge milling. The reabsorption problem was solved in a different way. The areas critical to the bow tie antennas, namely the gap between both wings, was milled last. This ensured that no material was sputtered into this critical locations.

5.3.4 Effects of scan direction

During the structuring optimisation it became evident that the scan direction has an effect on the bow tie elements. Focused ion beam devices create structures by exposing selected areas with the ion beam. For the exposure the patterns are fragmented into lines parallel to the 'scan direction'. The default 'scan direction' of the HeliosNanolab is from left to right and from top to bottom. Hence, patterns are converted into a bunch of horizontal lines for exposure and are then scanned from left to right.

In case of the nanoantennas the effects of the scan direction could be seen in the finished structures. Although a completely symmetrical pattern was milled, a mismatch between the left and the right side of the structure was visible. This is shown in picture 5.8.

In this case the effect of the scan direction becomes visible through a combination of redeposition and enhanced edge etching. On the left side of the structure the patterning started away from the structure and milled towards it. On the right side it started right next to the structure and

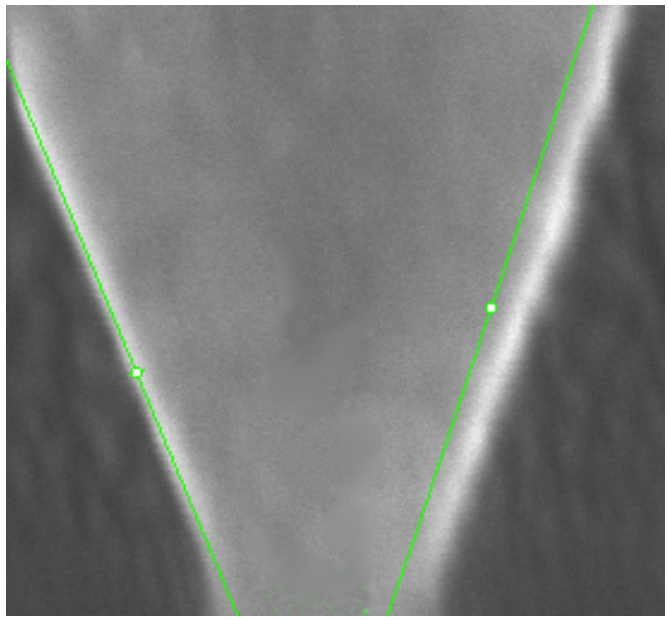

Figure 5.8: The effect of the scan direction on the bow tie elements. On the left side the beam is scanned towards the edge, while on the right side the milling starts at the edge and moves towards the border.

milled towards the right border. When milling a line, the effects of enhanced edge etching are stronger towards the end of the exposure, while the error through reabsorption is weaker. The result is a non-symmetrical patterning result for the bow tie elements, which should be corrected for optimal results.

5.3.5 Script controlled patterning

After analysing the problems arising for high resolution patterning, a modified patterning process was developed. The goal was to reduce the effect of the resolution decreasing factors discussed above. A script was develop which exercised fine control over all patterning parameters and then used the proximity effect in combination with enhanced edge milling

to create the gap.

In order to exercise fine control over the patterning, the machine parameters during pattern creation were analysed first. A focused ion beam device creates patterns by scanning them repeatedly. The relevant parameters during this scanning process are defined in the application file. They are 'dwell time', 'pitch', 'passes', 'overlap', 'beam diameter' and 'beam current'. During exposure a single location is exposed for the 'dwell time'. The exposure location is then shifted by the 'pitch' to the next location. When all positions have been exposed once, the process starts at the first location again. This cycle is repeated for the number of 'passes'. At this point the difference between 'serial' and 'parallel' patterning mode becomes noticeable. Serial milling fist finishes all required 'passes' for one pattern and then moves to the next defined pattern. On the other hand parallel patterning mills one cycle off every defined pattern, finishing all patterns at the same time. The 'beam diameter' depends on the aperture, respectively the beam current. The beam diameter can be further increased by setting a 'blur'. For each current, beam diameter and pitch are modified in order to keep the 'overlap' constant.

The auto script runtime at the Helios Nanolab 600 only had access to some of the above mentioned parameters directly. First and most easily set are beam currents and diameters through setting a fitting aperture. Here, the smallest available aperture (2.8 pA) and respectively the smallest beam diameter were chosen. For this aperture the beam diameter still was given as 9.8 nm. This small beam current resulted in long exposure times (around 70 h), but with a larger beam diameter exposure of the small gaps was not possible.

The parameters 'pitch', 'overlap', 'dwell time' and 'passes' are not directly accessible through the scripting environment. 'Dwell time' and 'passes' are set values depending on the application file, e.g. optimal parameters for gold milling are saved in the 'Au' application file. It is possible to modify application files with a text editor, but for the bow tie antennas only a uniform gold layer is milled. Therefore, this option was not explored further for this project and the default 'Au' application files used for all patterns milled.

On the other hand the 'pitch' and 'overlap' variables offer some additional

control over the spatial milling. For a given pattern the 'pitch' along two perpendicular directions can be changed. In the settings files these are called 'pitch X' and 'pitch Y'. They can only be edited by creating a pattern in the graphical user interface and changing their values in its advanced options. However, this method is impractical, because it makes it time-consuming to even make small changes and does not offer any possibilities for automation through scripting.

A work around method to control the 'pitch' parameter was developed. All high resolution patterns were created through milling multiple parallel equidistant lines. In this setup the distance between the lines has the same influence as the 'pitch' along this direction. This method only allows

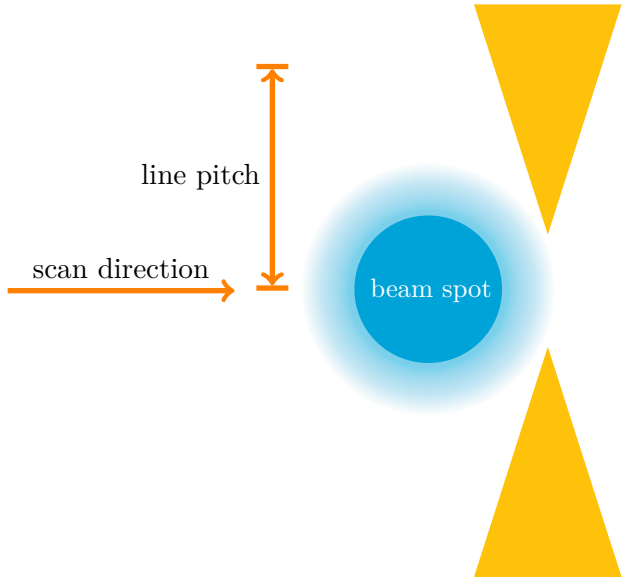

Figure 5.9: Alignment of the scan direction towards the bow tie antenna wings. In addition, the beam spot in respect to the gap is sketched. The gap is never directly exposed and only created through secondary effects (shaded area) discussed in the feature milling and proximity effect chapter. The sketch is not to scale.

direct control over one of the two pitch parameters. Therefore, this script controllable 'line pitch' variable was aligned along the direction were the highest influence of the 'pitch' towards the pattern was expected. In detail the lines were aligned in parallel to the scan direction and hence the 'line pitch' was perpendicular to the scan direction. The overall alignement of the bow tie and the scan direction is illustrated in sketch 5.9. In the same manner an 'overlap' can be created by reducing this distance below the distance of the beam diameter.

Using lines to assemble the high resolution structures has other advantages for the bow tie elements. The line can be arranged such that the centre, where the gap is created, is only milled by a single beam diameter wide structure. This offers the highest possible resolution. In other patterning modes this can not be ensured easily. There the pattern could be segmented in a way that the centre is milled by two beam diameters in the worst case. This would half the maximum resolution. The difference in resolution between optimal and non-optimal conditions is sketched on illustration 5.10A and 5.10B, respectively.

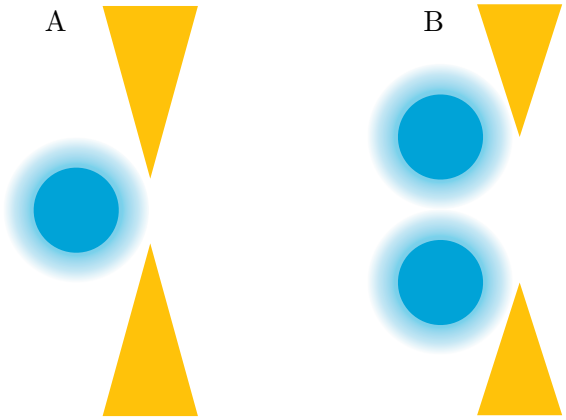

Figure 5.10: Difference between an optimally (A) and non-optimally (B) scanned bow tie and its influence on the gap size.

5.3.6 Opening angle of the bow tie elements

Resulting from the theoretical models, multiple configurations of opening angle and antenna wing length were of interest. However, it was not possible to realise every theoretically possible configuration. Thus, structuring tests on possible opening angles were performed. Then, in an iterative process the focused ion beam produced structures were tuned towards the simulations and vice versa.

Opening angles of up to 120 degrees were explored. It could be shown that with a greater opening angle the minimum gap size increased as well. When the angle increased, the amount of proximity overlap in the centre decreased. This resulted either in not completely divided bow ties or, if the energies were increased accordingly, in much wider gaps. A picture of a high angle bow tie can be seen in illustration 5.11.

In accordance with additional simulations the final structure parameters were chosen as follows: 160 nm as the antenna wing length, 20 nm as gap size and 60° as opening angle. A finite element simulation of expected field enhancements is shown on illustration 5.12.

5.3.7 Detailed patterning process

The general structuring process was divided into two different parts. In the first part the outer rim of the structure was removed by milling rectangular areas in parallel milling mode. These were defined using the 'box' commands. As can be seen from the code (figure 5.13), the rim parameters length, width and thickness were parameterised as well.

After the rim structure was defined, the actual bow tie structures were created. For this, multiple lines were defined with their contour mirroring the negative shape of the bow tie, i.e. a contour consisting of two triangles with their tips facing each other. This is illustrated in illustration 5.14. The source code for this subgroup is shown in figure 5.13.

As can be seen from the code or the sketch in illustration 5.13, only half of a bow tie structure was created with the first script. The bow tie was later completed through the use of 'beam rotation'. Through this step errors introduced by the scan direction could be avoided. This step is part

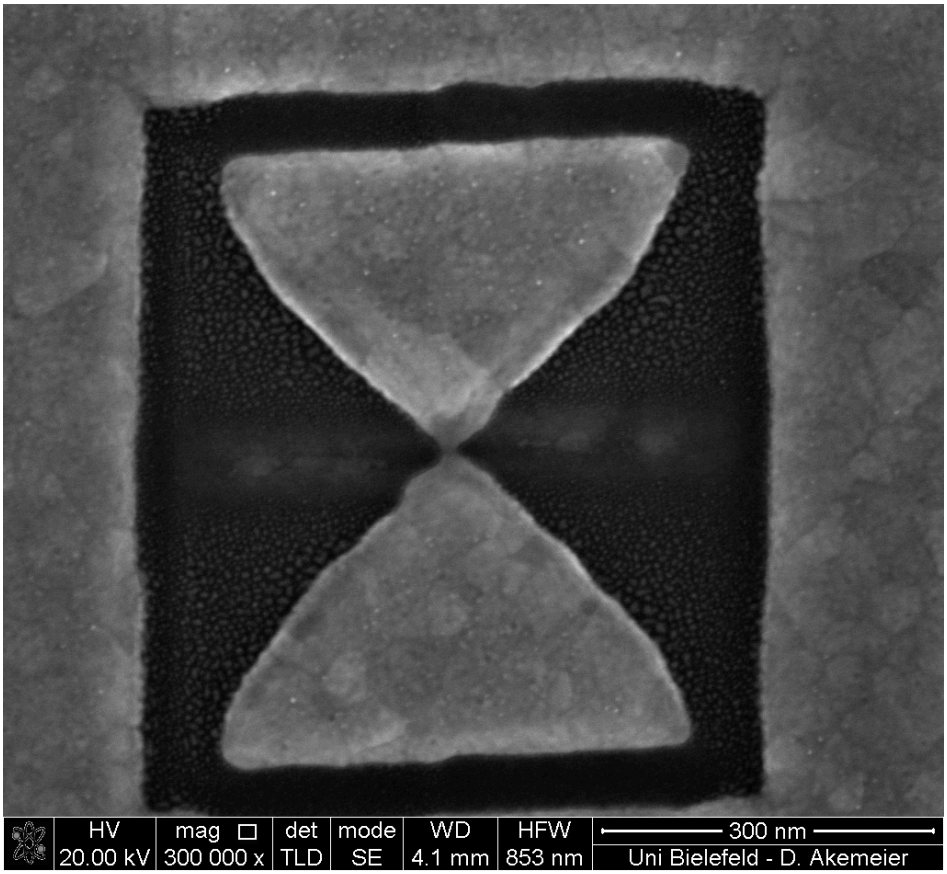

Figure 5.11: Scanning electron microscope image of a high opening angle bow tie. It was produced with the advance algorithms and, therefore, shows well defined edges. The wings, however, are still connected. Testing showed that removing this bridge is not possible without creating gaps much wider than 20 nm.

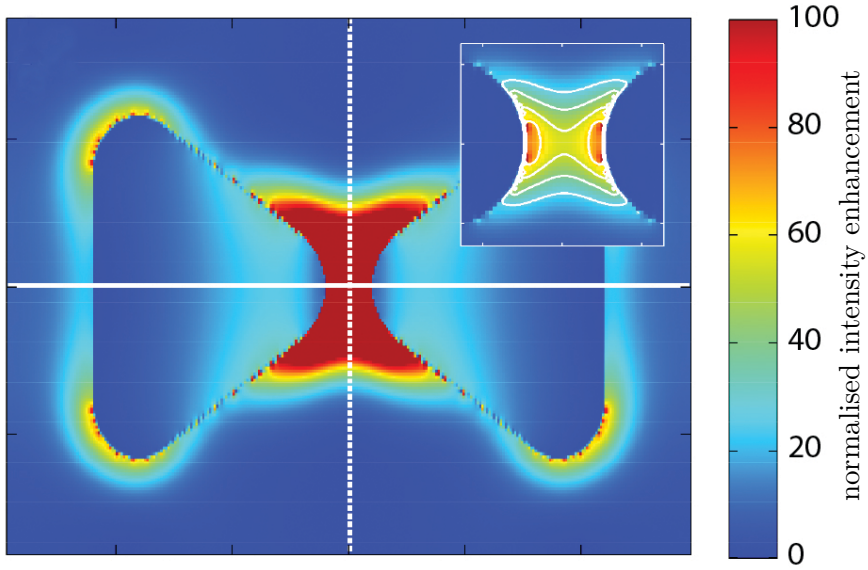

Figure 5.12: A normalised plot of the expected intensity levels. The maximum corresponds to an enhancement of 1500 times. The inset shows a detailed plot of the gap region with a different colour map. It ranges from 0 to 1500×.

of the automation routines and described in the automation chapter 5.3.9.

Creating the bow ties directly through 'line' commands has two distinct advantages over the 'polygon' approach from the first try. The first is fine control over the values for the structure characteristics like pitch, gap, dimensions and indirectly the overlap. By using parameters for these values it is possible to correct for enhanced edge etching effects for the overall structure. By tuning the pitch it was possible to reduce overexposure of the substrate which reduced the redeposition of substrate material. In addition, this gave a better control over the dose deposited on the sample surface. In picture 5.15 the effect of a very high dose can be seen. Although the dose in this test was too high by a factor of two, the overall effect and the tendency of an overexposure is clearly visible.

The second and more important part of using multiple lines is the possi-

```
#basic environment variables are set in the settings subfile
run settings.psc

setpatinfo 0.04, AU

##variables
#bd is the beam diameter

bd=0.01

#y values relate to length of the bowtie structure

ysize=21*bd
ystep=bd

#frame thickness
frame=0.05

#gap factor
g=0.0006

#xsize and xstep are the y values time tan 15 degrees

xsize=ysize*0.255993401
xstep=-g+ystep*0.255993401


n=1
nmax=21


###create a small box around the bowtie
box -xsize -frame ,-ysize-frame, -xsize, ysize+frame
box -xsize  ,-ysize-frame, 0, -ysize
box -xsize  ,+ysize+frame, 0, +ysize


#### first half  bow tie structure

loop1:

line -xsize-(2*frame), ysize-(n*ystep),-xsize+(n*xstep) ,ysize-(n*ystep)
line -xsize-(2*frame), -ysize+(n*ystep),-xsize+(n*xstep) ,-ysize+(n*ystep)
n=n+1

if (n<nmax) goto loop1

line -xsize-(2*frame), 0,-xsize+(n*xstep) ,0


result=1
```

Figure 5.13: Source code for the smallest building block of the bow tie array. This code only creates a half of a bow tie structure. In order to complete the bow tie, beam rotation is used.

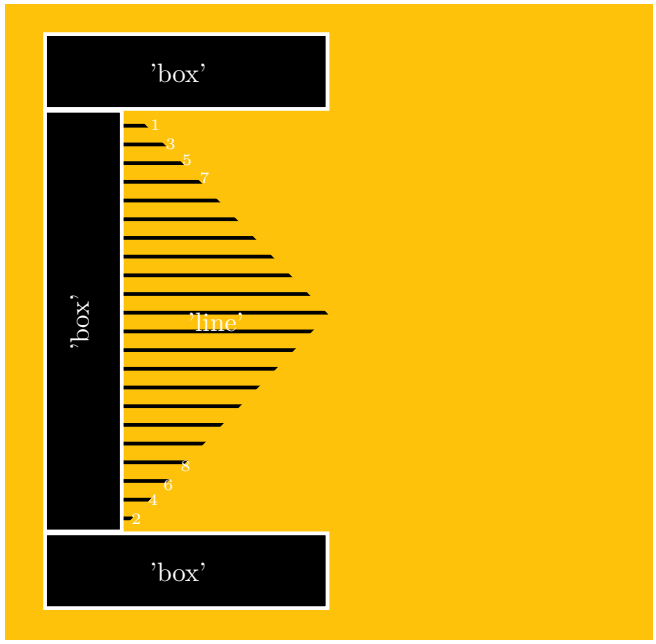

Figure 5.14: A sketch of the milled areas with the respective 'box' and 'line' commands from the script 5.13. The numbers indicate the sequence in which the lines were milled. The line in the centre is milled last.

bility to control the sequence of the exposure. For this, the serial milling setting was used. In this environment each feature is exposed in turn according to a number given during pattern creation. By default these numbers are according to the order the pattens are created in. It is possible to change pattern numbers through scripting commands, but in this case it was easier to create them in the desired order. The order was chosen in such a way that exposures alternated between both ends of the triangles and then progressed towards the middle. In detail the starting line was the line at the top, then it moved to the line at the bottom, then back to the line next to the top line and so forth. This is shown by numbers in illustration 5.14.

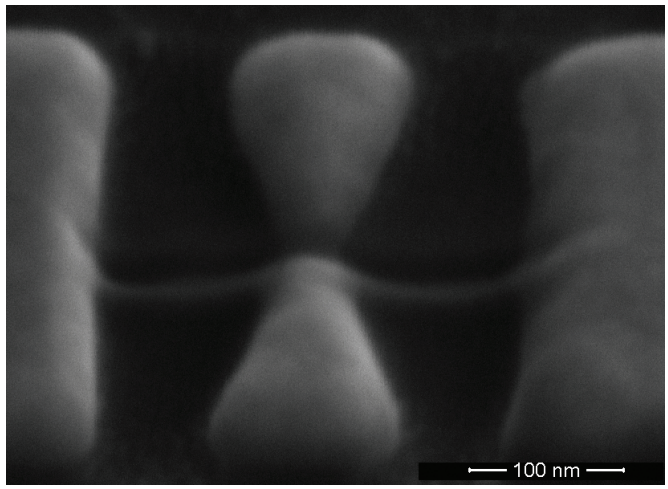

Figure 5.15: Example for an overmilled bow tie element. The thin line next to the gap is composed of redeposited material.

This exposure sequence had two advantages. First, by removing the central area last, redeposition could be negated for this area of the structure. This is important, because in the gap redeposited material has the strongest negative influence on the antennas.

Second, due to the exposure sequence most of the extra material removed by enhanced edge etching is in the central area. By maximising both the proximity and enhanced etching effects at the centre, it is possible to create the gap indirectly. This allows to create a feature below the resolution possible with a direct mill process.

5.3.8 Effect of beam astigmatism

To further increase the resolution of the system, controlled astigmatism was tested. A perfectly destigmated beam has a circular beam spot. When only changing the stigmation along one axis the circular spot with radius r becomes an elliptical spot with the radii r_x,r_y. If the stigmation is changed along the x-axis, r_x is greater than r while r_y equals r.

When comparing the elliptical beam profile to a circular one, two effects can be observed. First, the overall area of the beam spot increases. This is the main reason for the structure degrading effects of astigmatism. However, there are differences in the curvature radius. A circle has a constant curvature radius, while the curvature of an ellipse is dependent on the position. At the point k where the long axis would intersect with the rim, the curvature radius becomes minimal. A circle with radius r is compared with an ellipse with the radii r_y,r_x for the short and long axis, respectively. The curvature radius of the ellipse at the intersection point k is smaller than the circles.

This decrease in curvature can be used in the patterning process. For this purpose the beam spot is elongated parallel to the lines that create the bow tie shape. This way, the decreased curvature radius at the point k is used for patterning the gap. This effectively reduces the beam diameter available for the bow tie structuring and thereby increases the resolution further. The difference is sketched in illustration 5.16.

The patterning parameters had to be adjusted to the new beam shape and spot size. First, an elliptic beam shape, with the long axis parallel to

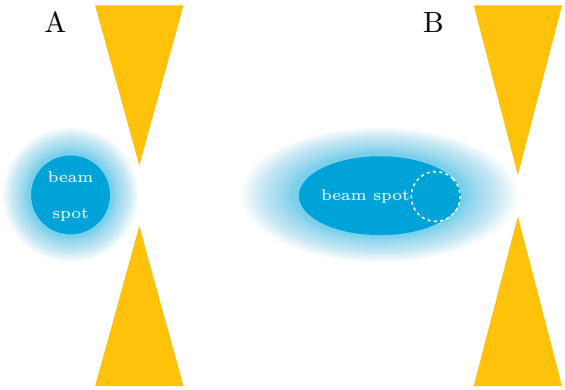

Figure 5.16: A: A circular beam spot used for bow tie patterning under optimal configuration. B: A beam spot selectively deformed by stigmation to increase resolution and decrease the effective beam diameter (white circle).

the scan direction, was created through the stigmator settings. Afterwards, test exposures were performed until the resulting bow tie elements again showed the desired shape and gap size. Pictures of the resulting elements are shown in section 5.4.

5.3.9 Automatisation

The automatisation process was divided in three pyramiding loop processes, with the resolution increasing with every loop level. The main loop (stage stitching loop) moves the stage in a stitching move. Instead of starting an exposure directly, it runs the next higher level loop (beam stitching loop). The beam stitching is also a stitching loop, but only uses the beam shift to move the exposure area. The beam stitching loop then runs the next higher loop (beam rotation loop) at each position. The beam rotation loop uses the beam rotation and mill commands to create a single bow tie element out of the half tie patterns described in section 5.3.7. The pyramid organisation of the scripts is visualised in illustration 5.17.

Beam rotation loop

First, a half tie pattern as detailed in section 5.3.7 is created by loading the corresponding subscript. The automatisation loop starts with exposing this structure. In order to complete the bow tie structure, a beam rotation of 180° is set. Afterwards, the pattern is exposed again.

Changing the beam rotation tilts the entire field of view by changing the overall scanning direction of the patterning beam. The effects of changing the scan rotation on the locations of already finished patterns are exactly like an eucentric rotation of the stage. Thus, after a beam rotation of 180° the position of the finished half tie is flipped vertically and is now on the right side of the write field, while the positions of the patterns stay on the left side. Exposing same pattern again completes the bow tie structure. The effects of changing the beam rotation are further visualised in illustration 5.18.

Working with the beam rotation during the automation process for the bow tie elements has two advantages. First, this corrects the effects of

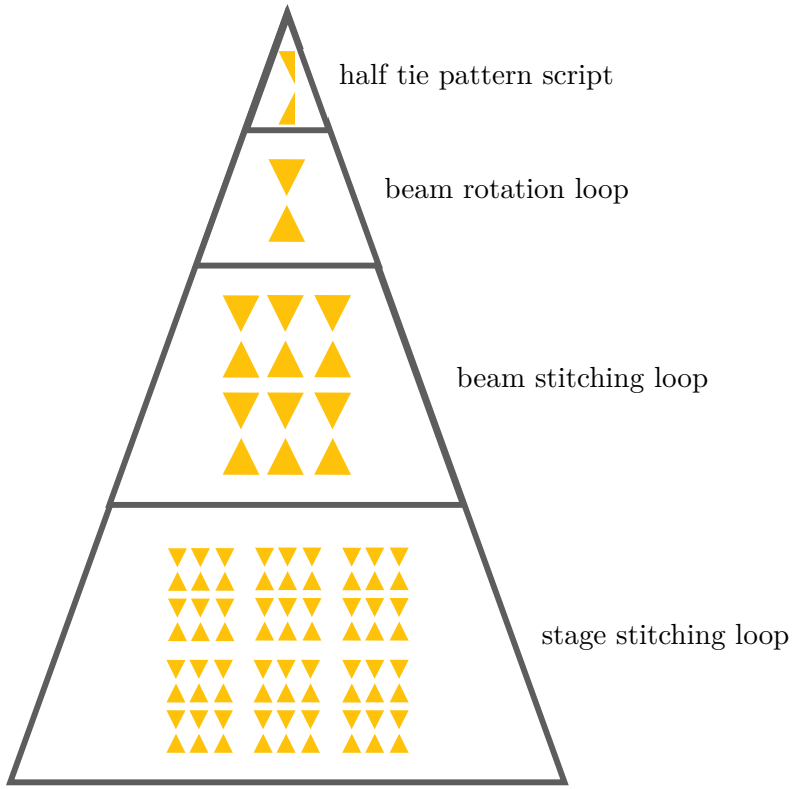

Figure 5.17: Organisation structure of the bow tie automation script.

the scan direction on the structuring process. As described in the pattern section, scanning from the border towards the bow tie is beneficial to the structure quality. By using the beam rotation both parts of the bow tie structure are milled with the favourable scan direction. The second advantage is a decrease in overall processing time. By reducing the entire bow tie pattern to a less complicated pattern exposed twice, no new patterns must be created after the first. This is similar to the improvements for the nanoaperture process developed in section 4.2.6. This decreases the overall processing time by a factor between 10 and 20 depending on the size of

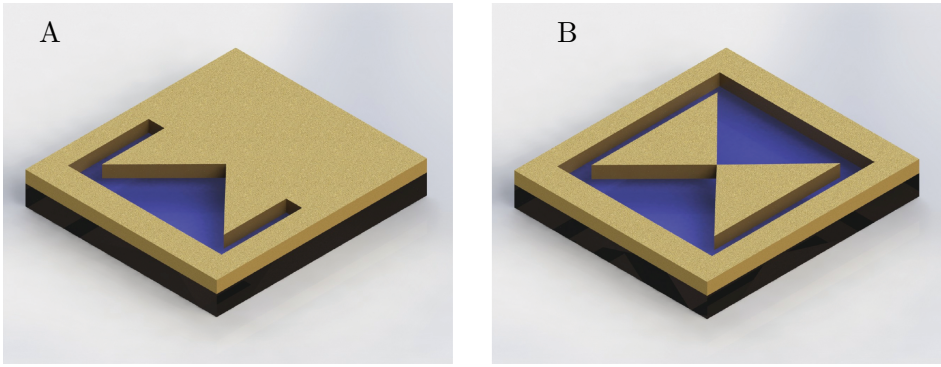

Figure 5.18: A rendered image of the two step bow tie creation process using the beam rotation. In order to create the bow tie structure the same structure (picture A) is exposed twice. The beam rotation is changed by 180° between the two exposure steps. With this trick, double exposure of the same pattern creates a complete bow tie element.

the bow tie pattern. Even with this time improvement the entire process took 14 h. Without this decrease in processing time the creation of bow tie structures with a focused ion beam microscope would not have been feasible.

Beam stichting loop

The next step in the automatisation process is merging the beam rotation loop with a small area stitching loop. The beam stitching loop uses the beam shift in order to create an array of 15 bow ties. This allows to stack a small array of bow ties with maximum density.

In case of the bow ties it is not possible to perform a stitching with the stage movement only. A bow tie structure has a width of 200 nm, while the stage move repetition accuracy is given as 450 nm for 40 successive moves. It would be possible to correct for possible stage positioning errors by including a margin of 450 nm around the structures. This is impractical, because it would decrease the overall antenna density by one order of magnitude. Therefore, an intermediate stitching with the beam shift is

necessary. The accuracy of the beam shift is dependent on the magnification, but for practical purposes it is below 10 nm.

The source code for the beam stitching is similar to the source code of a stitching done with the stage. The differences arise from the different speeds with which the operations are performed. A change in the beam shift is done without any mechanical movements. Therefore, no sleep commands between two shifts are needed. However, due to a bug within the focused ion beam software, not every beam shift command is applied. This problem was circumvented by adding additional loops to the beam stitching loop. They check if the stitch command was successful and if not return it to the set beam shift part. A relevant extract of the beam stitch source code is seen in illustration 5.19.

Stage stitching loop

In the last step of the automation process, stage movement was used in order to create nanoantennas over an area of 20 µm × 20 µm. After each beam stitch loop the stage was driven to the next sample position. There the beam stitch loop was started again in order to create the next cluster of nanoantennas. In accordance with the stage movement accuracy, a margin was defined around the antenna clusters. The stage stitching was performed in a rectangular spiral-like pattern. Therefore, a stitching application similar to the one for the nanoaperture was used (chapter 4.2.5).

```
#variables
#no computed
#variables used
beamstepx=0.208
beamstepy=0.52
r=0
s=0
stichcount=0
stichmax=3
#error counters
start:
errR=1
errU=1
errL=1
errD=1




stichcount=stichcount+1
##########################
beamright:

  #write first half tie

  br1:
  setbeamrot 0.68
  getbeamrot beamrot
  if (beamrot<>beamrot)
     goto br1:
  mill
  sleep 1000


  #write second half

  br2:
  setbeamrot 180.68
  getbeamrot beamrot
  if (beamrot<>beamrot)
     goto br2:
  mill
  sleep 1000

##########################
#Set beam shift and check
   settings

getbeamshift
xbnew=xbeam+beamstepx
dump

bs1:
  setbeamshift xbnew, ybeam
  getbeamshift
  dump
  errR=errR+1

if (errR>50) goto end:
if (xbnew+0.05<xbeam) goto
   bs1:
if (xbnew-0.05>xbeam) goto
   bs1:


r=r+1
if (r<>stichcount) goto
   beamright:
```

Figure 5.19: Part of the beam shift stitching code. This script includes additional loops to check if beam variables were applied by the machine.

5.4 Results

A specialised patterning process for a dual beam microscope, with a high level of control over all relevant parameters, was developed for the bow tie production. Using this process it was possible to create high resolution elements that achieved all structural requirements for higher harmonic generation. The improvements possible through the new structuring method can be seen from a direct comparison of two bow tie elements. First evaluation results are shown in picture 5.5, while picture 5.20 shows a bow tie structure created through the advanced script.

By fine-tuning the depth parameters it was possible to completely remove the gold around the bow tie structures without sputtering the sapphire substrate. Oversputtering can be seen in the trenches around the freestanding elements on earlier results. The effects of the scan direction are visible in direct comparison between the final bow tie and the extract shown in Figure 5.8. It is clearly visible that, using the beam rotation, it is possible to create a uniform edge quality on both sides of the structure. By including and actively using the enhanced edge etching effects as well as astigmatic patterning it was possible to reliably create 20 nm gaps. The element shown in illustration 5.20 is even below this value and has a gap size of 16 nm.

The material microstructure becomes a limiting factor for structure sizes below 20 nm. Gold grows in polycrystalline layers. The size of single grains is dependent on the deposition method and the temperature. Sputter deposited gold has a grain size between 10 nm and 20 nm. The grain boundaries have different sputter rates than the grains. The achieved resolution was only possible due to fine control and correction of different errors occurring during patterning. It is not possible to correct the effects of grain bounderies with software, due to their irregular distribution. Thus, once their effects on the patterning process becomes noticeable, the resolution becomes limited. One possible solution for this problem would be to use mono crystalline gold films [Hua10].

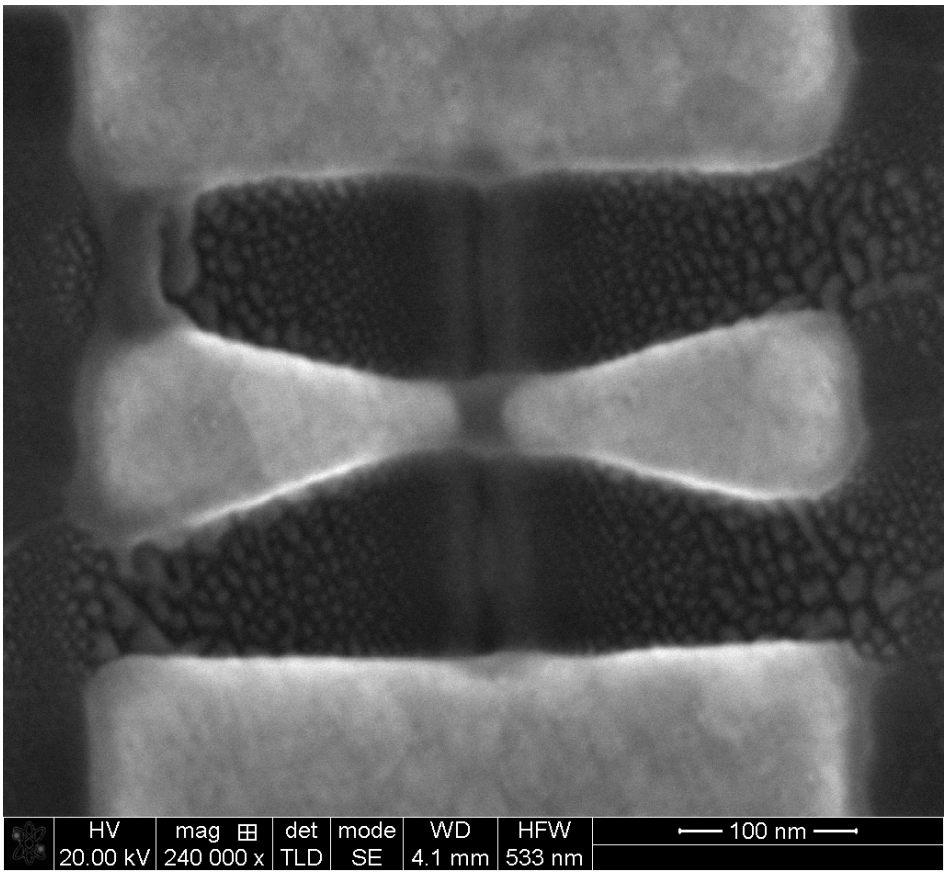

Figure 5.20: A single bow tie created with the latest version of the script. The effect of redeposition is clearly visible in the image. Redepositioned material is found at the outer sides of the bow tie, while no material is present at the centre gap location. This is in accordance with the expected behaviour for the redeposition effect. For this element a gap size of 16 nm was achieved. Substrate material was sputtered slightly around the gap in order to ensure insulation of both wings from each other.

5.4.1 Automation results

Through scripting automation it was possible to create active areas in the size regime of the laser focus. For this arrays of bow tie elements over areas up to 20 µm × 20 µm were created. The results of the automation process are shown in picture 5.21.

Most of the automation challenges were scripting related and could thereby be solved through changes in the programming. However, two errors appeared independent of the script version used. The first was a malfunctioning of the ion source after long exposures. During the time the exposures for the bow tie project were done, the liquid metal ion source was near its lifetime expectancy. Thus, it was impossible to maintain emission for long runtimes and the patterning stopped mid process[1]. This left some bow tie arrays partly finished. However, it was still possible to create enough arrays for the higher harmonics generation experiments.

Another problem with the automation routine resulted from the irresponsiveness of the electronics. Due to the high amount of commands issued by the script, the electronic within the dual beam microscope or the main control software was not always able to process all commands. This was already discussed for the beam shift in section 5.3.9. In the case of the beam stitch it was possible to solve this through additional readout routines. After the checking loops found that a command was not processed, they waited a short time and returned the script to a point before setting the command.

However, for the mill command there is no possibility to check if a milling operation was performed. Hence, not all bow tie elements are milled. This can be seen in picture 5.21. All groups of 15 bow tie elements are exposed using the exact same subscript. When the mill command is not processed, a block of substrate material is left standing. This skipping of certain mill processes is a random event. It was possible to reduce the amount of missmilled structures through additional sleep times in the software, but it was not possible to completely remove the effects of this software glitch.

Even with the above mentioned problems, the overall quality of the struc-

1 The ion source shut down after 24 to 48 hours.

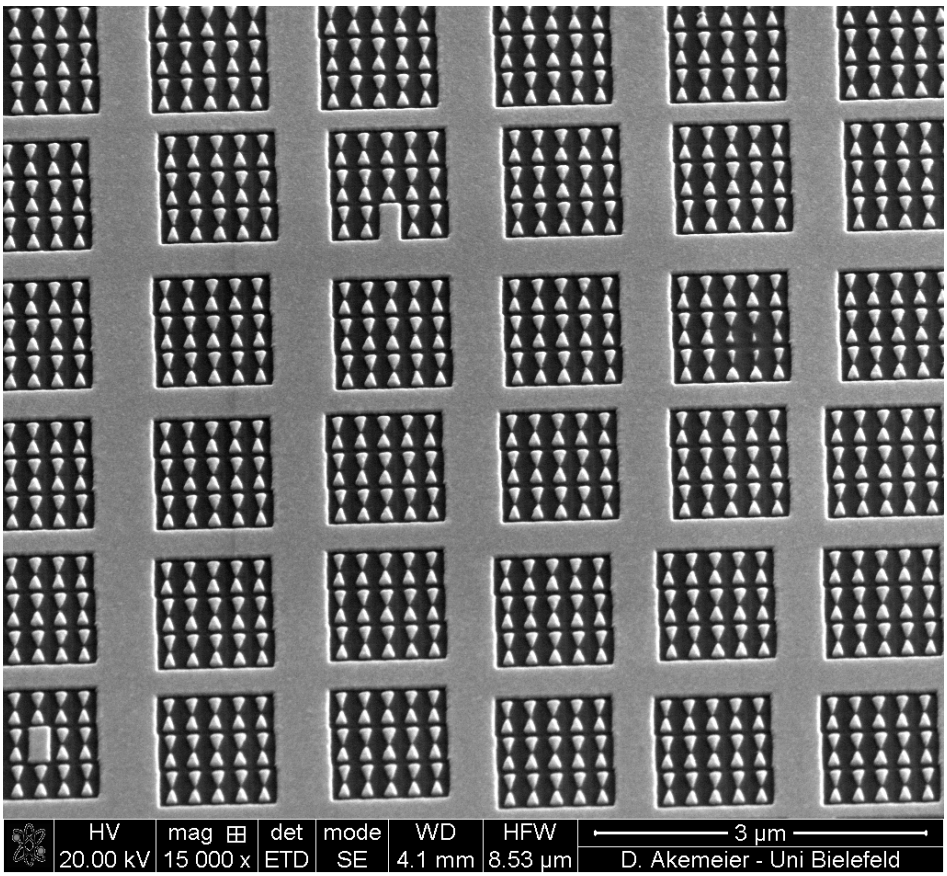

Figure 5.21: An array of bow tie antennas. The bow tie groups cover an area of 20 µm × 20 µm. The errors in some groups are a result of glitches in the electronic of the focused ion beam device and occur at random times.

tures and the throughput was acceptable. Multiple areas of 20 µm × 20 µm were patterned. The patterns were arranged on a matrix with extra characters denoting row and column. Theses character are visible under a light microscope and helped localising the overall pattern during the measurement. A finished matrix of multiple bow tie arrays is shown in picture 5.24.

5.4.2 Higher harmonic measurements of focused ion beam produced nanoantennas

The measurements were performed in a higher harmonics setup at the University of Hannover by Nils Phulmann. The experiment used a femtosecond pulsed laser to illuminate the bow tie structures through the sapphire substrate. From the other side a gas jet of xenon atoms was directed at the nanoantennas. The experiment is described in detail in the thesis of Nils Pfullmann [Pfu12] as well as in the publications by Pfullmann et al. [Pfua, Pfub].

The laser system employs a self-built Ti:sapphire oscillator with an operating wavelength of 820 nm and an output power between 270 mW and 400 mW. The oscillator delivers pulses with a pulse duration < 10 fs. A double chirped mirror and a pair of fused silica wedges are used to compensate for the dispersion of the setup. The beam is finally focused on the bow tie substrate with a variety of achromatic lenses.

The bow tie substrate is housed on a two dimensional translation stage in a vacuum chamber. The laser beam illuminates the bow ties through the sapphire substrate. The xenon gas is directed towards the substrate through a micro needle from the opposite side with an adjustable distance between the gas nozzle and the substrate. A confocal monochromator is used to select the resulting radiation. Finally a photo multiplier tube in combination with a photon counter is used to measure the signal behind the exit slit.

The gas feed onto the substrate in the setup was additionally characterised. The gas atoms act as emitters and have a large influence on the overall signal. The number of emitters scales directly with the number of contributing atoms squared. The gas nozzle was characterised using a

velocity map imaging spectrometer [Epp97]. In combination with mass flow measurements through the nozzle the number of atoms at the substrate location was calculated. Only atoms in the vicinity of the antenna gap can contribute. Around 200 bow tie cavities are illuminated simultaneously by the laser spot, resulting in 5.9×10^5 atoms in the active area.

From the number of active atoms the expected reduced harmonic conversion rate can be calculated using a conservative approximation for the excitation volume. A rate of

$$\frac{C_{\text{nano}}}{C_{\text{conv}}} \sim 7 \cdot 10^{-4} \tag{5.11}$$

was found. Here, C_{nano} denotes the conversion rate of the bow tie system and C_{conv} the bulk conversion rates. In comparison, Sivis et al. reported a reduced intensity of $\lesssim 10^{-8}$ [Siv12]. On the other hand the group of Kim et. al stated $\sim 8 \times 10^{-4}$ atoms in their interaction volume, leading to conversion rates of $\sim 10^{-4}$. Using the volume approximations of Kim et al., a conversion rate of 10^{-2} was found for the Hannover experiments.

5.4.3 Thermal stability measurements

The thermal stability of the system was measured to gather data on the destruction thresholds and maximum excitation energies usable. The intensity was increased until a drop in the signal became visible. Scanning electron microscopy images as well as energy disperse x-ray measurements were performed afterwards. The resulting images are shown in figure 5.22.

The laser provides an output power of up to 300 mW. Depending on the achromatic lens used for focusing on the sample, the peak intensities vary. A smaller lens leads to a higher peak intensity. The actual peak intensities on the substrate were computed theoretically from the reconstructed pulse profiles. They range from $1.8 \times 10^{11}\,\mathrm{W\,cm^{-2}}$ for a 200 mm lens to $1.4 \times 10^{12}\,\mathrm{W\,cm^{-2}}$ for a 80 mm lens. The measurements showed that all antennas started degrading above a threshold peak intensity of $10^{12}\,\mathrm{W\,cm^{-2}}$. In accordance with the theoretical predictions, antenna with long wings (200 nm) proved to be much more stable (chapter 5.2.1), while short antennas with only 140 nm wing length were destroyed around

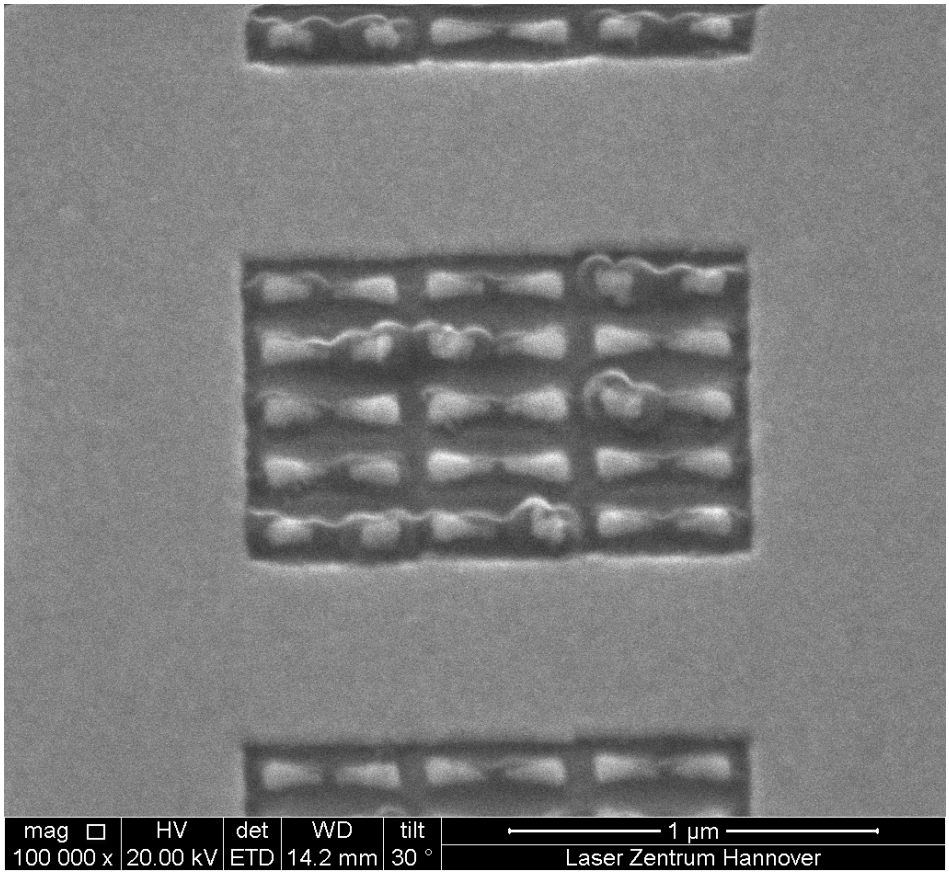

Figure 5.22: Scanning electron microscopy image of bow tie elements after the stability testing. Above the threshold, sample modifications in form of the line-like features between the bow ties are found.

$5 \times 10^{11}\,\mathrm{W\,cm^{-2}}$.

Time resolved measurements were performed on the nanoantennas. They showed an initial decay for all laser intensities. Directly after the start of the measurement the third harmonic signal was at maximum strength. Then the signal decayed exponentially until it reached a stable plateau. Through the short pulses of the laser excitation the antennas melt only partly or at the tips. This results in an initial reformation and a slight degradation of the signal. After a short timespan the antennas find a stable equilibrium position [Kim12].

The experimental results are in good accordance with the results of the theoretical predictions for the heat dissipation in the nanoantennas from chapter 5.2.1. The real nanoantenna show a slightly higher damage threshold. This difference can be explained through the simplicity of the used model. Taking a non uniform temperature distribution into account, the damage threshold is increased by 8% [Baf11].

A picture of elements after the stability test is shown in illustration 5.22. Bridge-like structures can be seen over the gap area. Energy-dispersive x-ray spectography revealed that these structures most likely consisted of substrate material. The optical breakdown limit and subsequent reshaping for sapphire is found above a peak intensity $1.4 \times 10^{13}\,\mathrm{W\,cm^{-2}}$ [Lin96]. This intensity can be reached within the feed gap of the bow tie elements.

5.4.4 Third and higher harmonic generation

The higher harmonic experiments were performed in three steps. First, the third harmonic signal was recorded. This measurement was used as an indicator if higher order harmonic generation is possible with the produced nanostructures and to measure the field enhancement effect created by the nanoantennas. In a second step, maps of the substrates with multiple arrays were obtained. Finally, higher harmonic generation was measured over a wide spectrum on a well defined array of bow tie antennas.

First, the non linear response of the antennas was evaluated. The resulting spectra of incident laser power over third harmonic signal are shown in illustration 5.25. These measurements can be used to analyse the field enhancement of the nanoantennas. The values of the nanotextured elements

were compared with those of an unstructured substrate. For the bow tie elements, field enhancement effects of up to 300 times were found.

The area is scanned with a piezo stage and a small laser power. From the resulting third harmonic signal a map of the sample is reconstructed. On this map the antenna clusters become bright spots. The map is used during the higher harmonic generation experiments to find the antenna clusters. A map is shown in illustration 5.23. The map corresponds to the antenna array shown in the scanning electron micrograph 5.24.

Finally, the higher order harmonic generation was performed. Therefore, a noble gas was injected into the feed gap trough a gas nozzle. For this measurements xenon was used. The noble gas increases the overall conversion efficiency for higher harmonics signals of the system to observable levels. However, additional spectral lines created by atomic line emission of the xenon are found in the spectrum.

The results of the higher harmonics generation experiment are illustrated in picture 5.26. The grey shaded areas correspond to higher harmonics of the driving laser. The orange bars indicate plasma lines of the xenon gas, with their height relative to their strength. A strong xenon fluorescence is visible

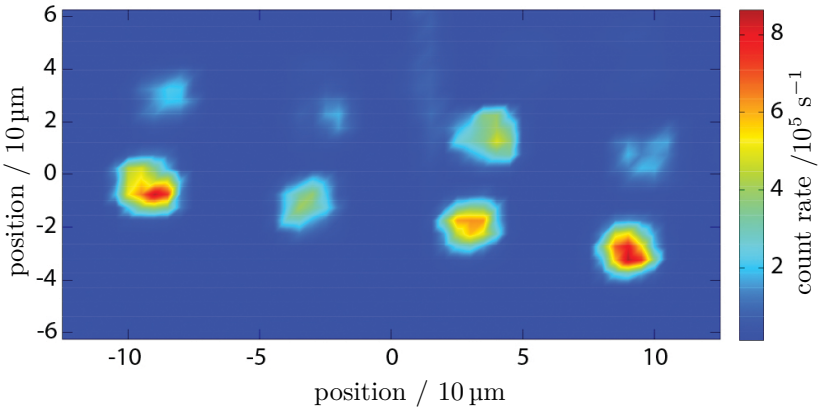

Figure 5.23: Third harmonic map of the sample shown in illustration 5.24. The bottom line of bright spots corresponds to the left line of bow tie arrays on the electron microscopy picture.

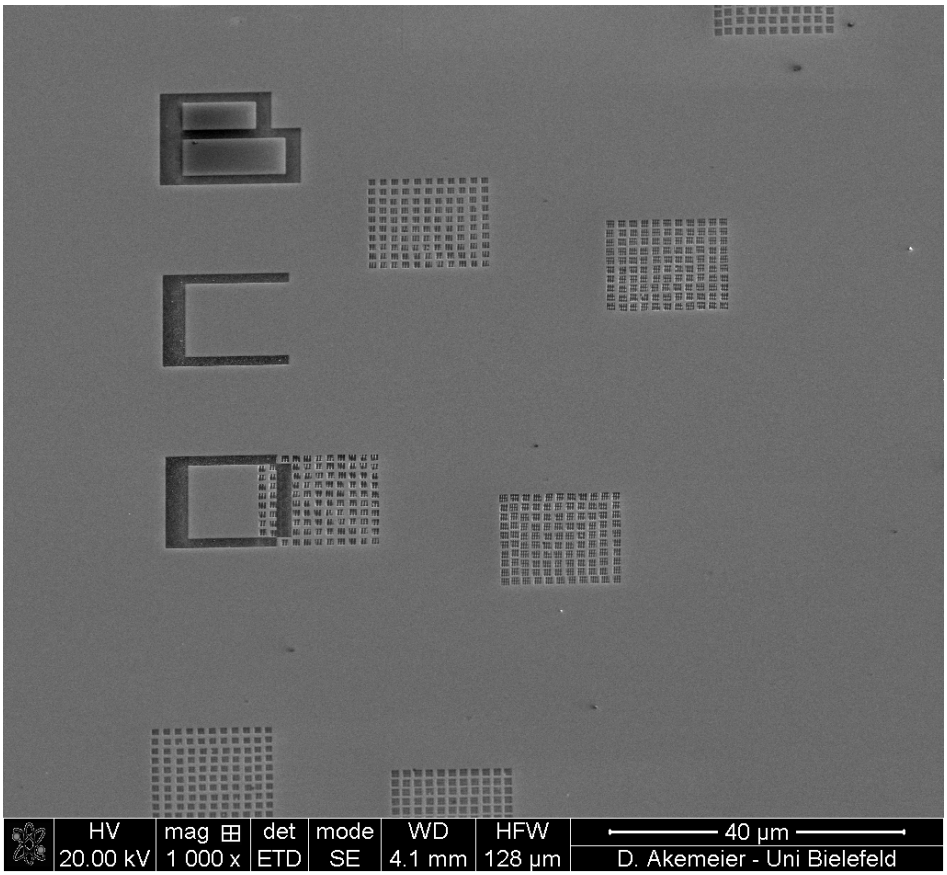

Figure 5.24: Multiple arrays of bow tie antennas. The letters on the left are a guiding structure for the final measurement and visible under a light microscope. Due to an error in a variable tracking the stage position the bow ties are not positioned perfectly. This was corrected in later versions. However, because the exposure of a complete array takes around 50 h of machine time, this array was used for measurements.

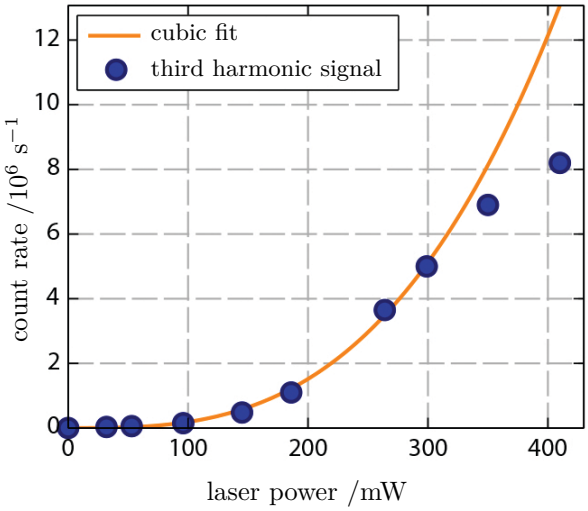

Figure 5.25: Third harmonic response of the bow tie antennas.

at the peak at 104 nm and was also reported by Schafer et al. [Sch97]. The measurements show high count rates at the positions of the ninth and eleventh higher harmonic. The signal at the position of the seventh harmonic is very weak. This effect could arise from the low conversion efficiency of the grating for this spectral range.

A detailed scan of the area around the 7th harmonic was performed using a different grate. The scan is shown in illustration 5.27. In addition, a correction for the diffraction efficiency of the grate was performed. In this measurement the peak of the 7th harmonic is clearly visible.

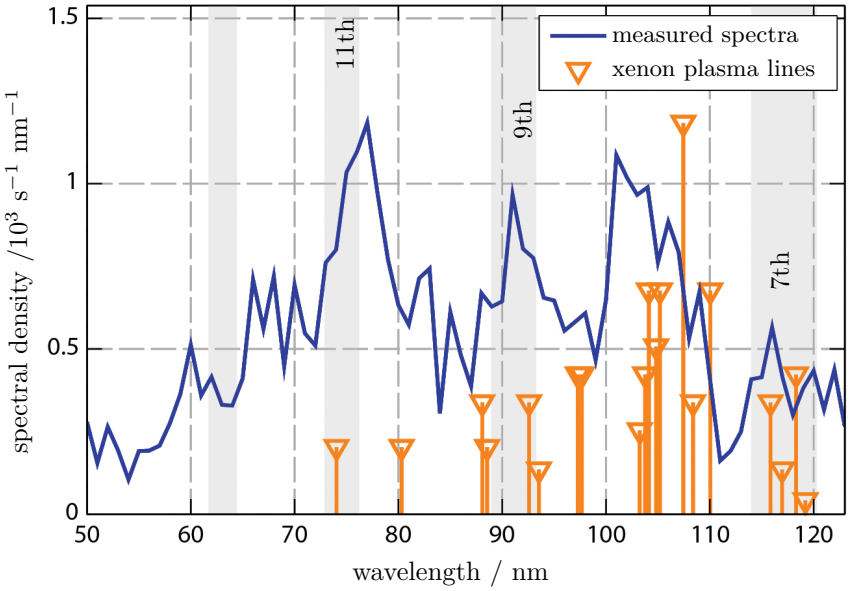

Figure 5.26: Spectral emission of 170 nm long bow tie antennas in a xenon atmosphere with 200 mbar backing pressure. The grey shaded areas indicate higher harmonics of the driving laser. The highest photon count is found at 76 nm, which is close to the eleventh harmonic.

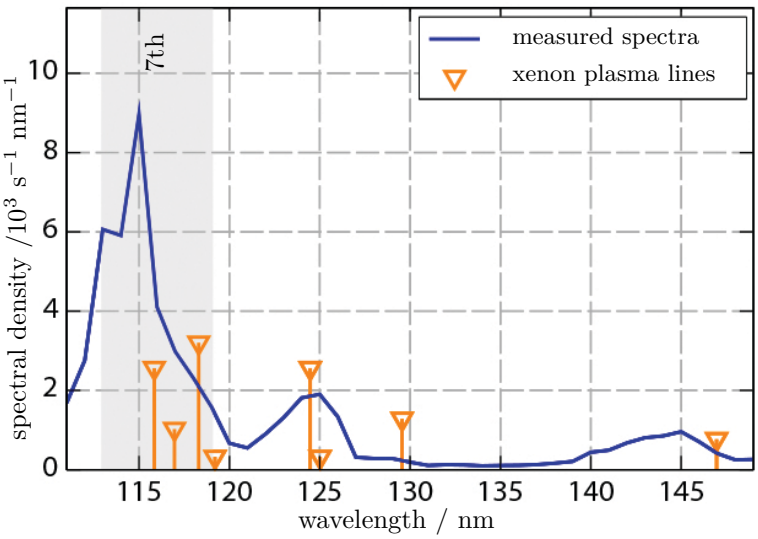

Figure 5.27: Spectrum of the region around the location of the 7th higher harmonic of the driving laser. This measurement was done with xenon gas at a pressure of 200 mbar. In addition, the data from this measurement is corrected for the diffraction efficiency of the grate.

5.5 Summary and Outlook

Nanostructured antennas are a possible tool to achieve further miniaturisation of short wavelength coherent light sources. The required structure dimensions as well as the overall structure quality for the nanoantennas is near the resolution limit of state of the art lithography processes [Iwa09]. For example, the next generation of intel processors released this year has a structure width of 22 nm. While resist-based lithography can achieve the required resolution, the optimisation of these lithography processes is time consuming. In order to make small changes on the layout or design of the structures, an entire sample must be completely processed, including resist preparation, exposure and finally structure transfer processes. Therefore, the patterning of the optical antennas was done with a script assisted focused ion beam patterning routine. The challenges arising from patterning nanometer sized elements are still offset by the advantages of the fast prototyping environment available in a dual beam device. For the nanoantennas especially the possibility to make rapid changes to the design allowed a strong integration with the theoretical predictions.

In order to create nanometer sized objects with focused ion beam milling, the pattern generation process in a focused ion beam device was analysed in detail. First, the influence of the sample topology and milling of features was analysed. The increased sputter rate found at edges was afterwards corrected for in the final process. Second, the effect of reabsorbed material was discussed. To minimise its influence on the overall pattern quality the timing of the sub milling processes was adjusted accordingly. The effects of the rasterisation of patterns by the focused ion beam device was analysed. Here, differences in structure quality between the left and right side of a structure were found. This was solved in the automation routine by using the beam rotation in such a way that the more favourable rasterisation was used at all times.

Afterwards, an automatisation routine was developed using the scripting environment provided by the focused ion beam device. The software created for bow tie prototyping is discussed in detail. Not all options needed to solve the problems observed during the process analyses are directly accessible through the scripting environment. Therefore, specific

workaround procedures were created and discussed. An additional effort was made to circumvent limitations created through the control hardware of the focused ion beam device. Afterwards, the script was optimised in the overall processing time, using tricks devised for the automated aperture production. Additional code was included to retain the fast prototyping possibilities, by keeping all needed parameters easily accessible.

Using the developed scripts, bow tie shaped antennas were structured successfully into a 50 nm thick layer of sputter depositioned gold. A 20 nm gap between both wings of the bow tie was achieved, resulting in an aspect ration of 2.5 to 1 between the film thickness and the smallest features. The antenna length and the opening angle were optimised in accordance with theoretical predictions to a length of 170 nm for a single wing and an opening angle of 60° was found to be optimal.

Using the nanoantennas it was possible to generate extreme ultraviolet radiation. The third harmonic signal was used to determine the field enhancement. Enhancements of up to 300× were found. Measurements of higher harmonics were performed under xenon atmosphere. Here, the spectra found could be partly attributed to atomic line emission. However, distinct peaks at locations where a higher harmonic radiation was expected were also part of the spectra. Higher harmonic signals up to the 11th harmonic were found. Final measurements on the coherency of this radiation are yet to be performed.

In order to achieve even higher harmonic signals and better conversion rates the fields strength at the gap location must be increased. This can be done by decreasing the distance between the tips. The focused ion beam process was already thoroughly optimised. Not much additional resolution can be gained at the milling site. However, one resolution decreasing factor is the quality of the thin film. The grains of the polycrystalline gold film have the same size regime as the gap. Patterns milled in mono crystalline gold layers already show significantly improved resolution [Hua10] and could offer a perfect substrate material in further experiments.

6 Focused ion beam tomography of a mouse kidney glomerulus

In recent years, the introduction of low acceleration voltage electron optics has sparked interest in scanning electron microscopy for soft matter [Rou09]. Low energy electrons allow imaging with a high surface sensitivity. The combination of surface sensitive imaging and high resolution milling provided by a dual beam microscope can be used to obtain 3D image data.

Within the scope of this work the methodology was tested on different biological samples and their preparation, milling and imaging parameters were optimised. The main interest was in the reconstruction of biological tissue. The most detailed work was done on mouse kidney tissue focussing on the glomerular region. The aim was to elucidate the tissue architecture of a healthy mouse glomerulus with a large field of view. Knowing the 3D architecture of a tissue sample is essential for understanding its physiological functions. In case of the glomerulus, insight into the ultrafiltration taking place at the blood urine barrier was envisioned. Furthermore, structural changes on cellular or tissue level often result in pathologic alterations and dysfunction of these structures.

6.1 Background

6.1.1 Kidney histology

In mammals, urine is filtered from the blood circulation in the kidney. The primary filtrate is formed in the glomerulus that is encapsulated by Bowman's space and enclosed by Bowman's capsule. A sketch of the glomerulus is found in illustration 6.1. In the glomerulus the primary filtrate is formed by ultrafiltration across the glomerular filtration barrier,

which consists of fenestrated endothelial cells, the basement membrane and the slit diaphragm between the podocyte processes [Nea05]. The foot processes and the slit membrane are localized at the basolateral site, while a well-developed cell body faces the urinary space [Pav03]. Alterations in the structure and morphology of this delicate structures as well as changes in their number and size have been associated with renal and systemic diseases [Bee11].

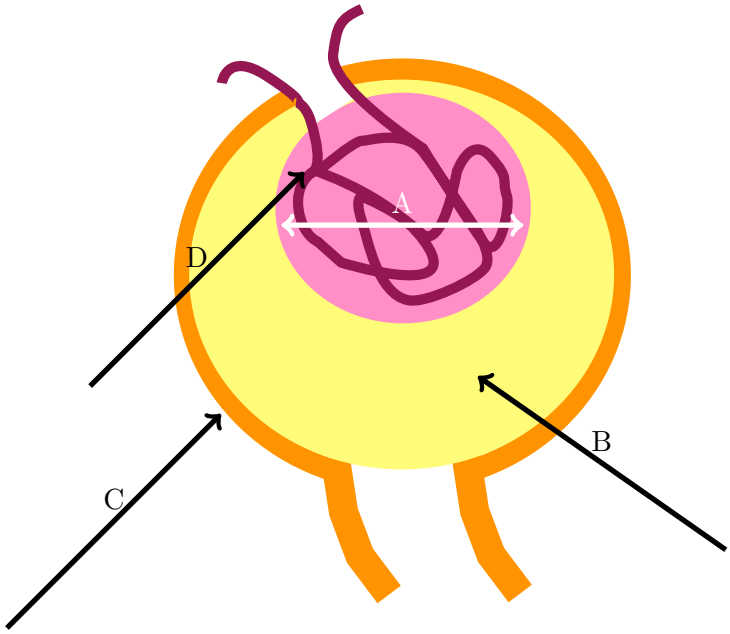

Figure 6.1: Sketch of the glomerular region. Pointer A indicates the glomerulus, pointer B the Bowman's space, pointer C the Bowman's capsule and pointer D glomerular capillaries.

6.1.2 Approaches to analyse and reconstruct renal tissue

Up to now, different approaches were used to analyse and reconstruct renal tissue. Among them methods such as magnetic resonance imaging or light and electron microscopy. In previous studies the total number and sizes of

glomeruli in perfused rat kidneys was analysed by Beeman et al.[Bee11], but without obtaining cellular resolution. Proximal tubules were reconstructed manually from microscopic serial sections [Xia03]. In addition, a distinct part of the rat glomerulus, namely the area around a single capillary, was reconstructed by serial sectioning electron microscopy [Nea05].

The clear disadvantage of these analytical methods is that multiple imaging techniques were used to cover the range of scales from whole organ to macromolecular ultrastructure. In addition, these methods require different preparation techniques, making it impossible to create a high resolution image from the exact same volume. While some of those methods relied on serial sections for volume information, all sections were prepared ex situ and lack the slice resolution possible through focused ion beam milling. Real three dimensional reconstruction has another advantage by enabling direct measurements of numbers, surface areas and volumes. In contrast to the indirect estimates that can be made using stereology [Hoy03].

6.1.3 Tomography with a dual beam microscope

Dual beam tomography is a combination of focused ion beam sectioning and electron imaging. In contrast to other sectioning methods, the same device is used for sectioning and imaging. This increases the resolution and simplifies alignment routines. In addition, there is no risk of loosing sections during a transfer process.

For 3D tomography a series of cuts is performed with the ion beam. By taking an electron image after each cut, an image stack is obtained. A simplified sketch of the process is shown in illustration 6.2. Electron imaging is performed with a low accelerator voltage mode. From the image stack a 3D model of the sectioned volume can be reconstructed.

During the last years this method has been applied in different areas of cell biology, e.g. for the reconstruction of chicken embryo retinal tissue [Bus11], neuronal cell reconstruction [Kno08], whole organ analysis of arthropods [Les10], analysis of *Plasmodium* infected erythrocytes [Med12] or angiogenesis in zebrafish embryos [Arm09].

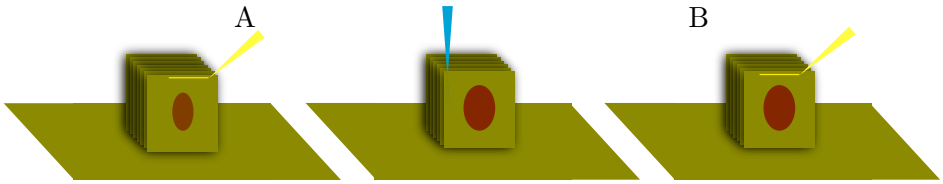

Figure 6.2: A sketch of the sectioning process in the dual beam device. First, an image of the front face is taken with the electron beam. Afterwards, the ion beam is used to remove this surface. Then another image is taken and the process is repeated.

6.1.4 Resolution window

Dual beam tomography is a recent development and there is still room for optimisation. However, the technique already has a lot of interesting applications. This is due to the unique resolution to volume ratio accessible. The resolution of dual beam tomography is dependent and limited by both, the imaging resolution of the electron beam and the milling resolution of the ion beam.

A scanning electron microscope can achieve sub nanometer resolution under optimal conditions with high contrast samples. However, the resin embedded tissue samples do not offer a high contrast and are barely conducting. The possible resolution is further reduced by the requirements for the tomography process, a low accelerator voltage to increase the surface sensitivity and the orientation of the sample towards the electron optic. The electron imaging is only important for the resolution in 2 dimensions (x and y). The resolution in the third dimension (z) is limited by the accuracy of the ion milling and the surface sensitivity of the electron imaging. The resolution of the ion beam was determined as 4 nm during the acceptance test. However, while it is possible to mill resin with a high resolution, it is not the optimal material. In addition, for subsequent electron imaging smooth surfaces over a wide areas are needed. This results in a slight over-milling. From the experience with transmission electron lamella preparation, the milling resolution is estimated to be 10 nm.

The volume accessible with dual beam tomography is dependent on the

resolution and the actual sectioning method. In the simplest case, without image stitching, the maximum field of view in x- and y-direction is between 150 µm and 200 µm. In the z-direction the volume can be larger. Here, the maximum values are dependent on the time available and the sample. Tomograms with millimetre length in the z-coordinate were recorded by Armer et al. [Arm09].

The possible resolution and volume values of dual beam tomography can be compared with other established tomography methods. While transmission electron tomography has an advantage of resolution, the possible volumes are very limited. On the other hand, microcomputer tomography can scan huge volumes, but the resolution is in the micrometer regime [Chi13]. Dual beam tomography thereby opens a new field with nanometer resolution over a block of 150 µm × 150 µm × 150 µm or bigger in z-direction. This allows imaging of multiple cells, while still being able to resolve membranes and organelles.

6.2 3D reconstruction of a mouse kidney glomerulus

6.2.1 Tissue preparation

Before imaging, the samples must be prepared for the tomography process. This preparation step is dependent on the material used. Tissue sample must be dehydrated and embedded in a an epoxy resin. Epoxy samples have a good ion beam milling behaviour and form smooth surfaces suitable for imaging when milled [Koc09]. The process is similar to soft matter preparation for transmission electron microscopy and also increases the conductance of the material. For imaging it is important that the sample withstands continued high current electron imaging without charging.

All animal experiments were performed at the university of Frankfurt under approval number G09-23 of the regional council of Freiburg. An epoxy embedding process is used for the kidney samples. Additional, steps were performed to increase contrast and conductivity of the samples. The best results were obtained using the following protocol.

First, wild type mouse kidneys were harvested from between 8 to 12 week old adult mice. The kidneys were perfused with fixative. Then, small

kidney tissue blocks of 2 mm × 2 mm × 2 mm were prepared and fixed in 2.5 % glutaraldehyde in 0.1 M sodium cacodylate buffer (pH 7.2) for 1 h at room temperature. Afterwards, tissue pieces were washed twice in 0.1 M sodium cacodylate buffer. Tissue pieces were postfixed using 1% osmium tetroxide/1.5% potassium ferricyanide in 0.1 M sodium cacodylate for 1 h at room temperature. After 3 x 10 min rinsing in 0.1 M sodium cacodylate buffer the samples were incubated in 1% tannic acid for 1 h at room temperature as previously described by [Bus11]. After washing with distilled water for 3 × 10 min samples were en bloc stained with 0.5% uranyl acetate at 4 °C over night. Sample dehydration was performed in a graded series of acetone (60% - 100%). The samples were embedded in epon resin and cured at 60 °C for at least 24 h in an eppendorf vial.

6.2.2 Micromachining and identification of glomeruli

Before the micromachining, access material was removed. Therefore, the epon block containing kidney tissue was cut free from the eppendorf vial and was then trimmed by hand using a conventional razor blade. An image of the epon block is found on illustration 6.3A. Afterwards, semi-thin sections were cut and stained with toluidine-blue. Through these cuts the glomeruli within kidney tissue were identified. Afterwards, ultrathin sections were cut for transmission electron microscopy analysis of the ultrastructural preservation of the kidney tissue and the quality of the staining protocol.

A single glomerulus was picked and further micromachined. Using an EM UC7 ultramicrotome (Leica AG, Wetzlar, Germany) a pyramid shaped cut was created around the glomerulus (illustration 6.3C). At the top a cuboid with an area of 100 µm x 100 µm and a height of 100 µm including the glomerulus was trimmed out of the epon block. Afterwards, the top 2 mm of the epon block was sawed of. The plain bottom surface of the emerging pyramid was glued on a standard scanning electron microscope sample stub, using carbon tape and Leit-C-Plast (Plano GMBH, Wetzlar, Germany). A rendering as well as a photography of the finished sample is shown on illustration 6.4.

To enhance conductivity of the samples their sockets were carefully painted with conductive silver, grounded with the sample stub and dried

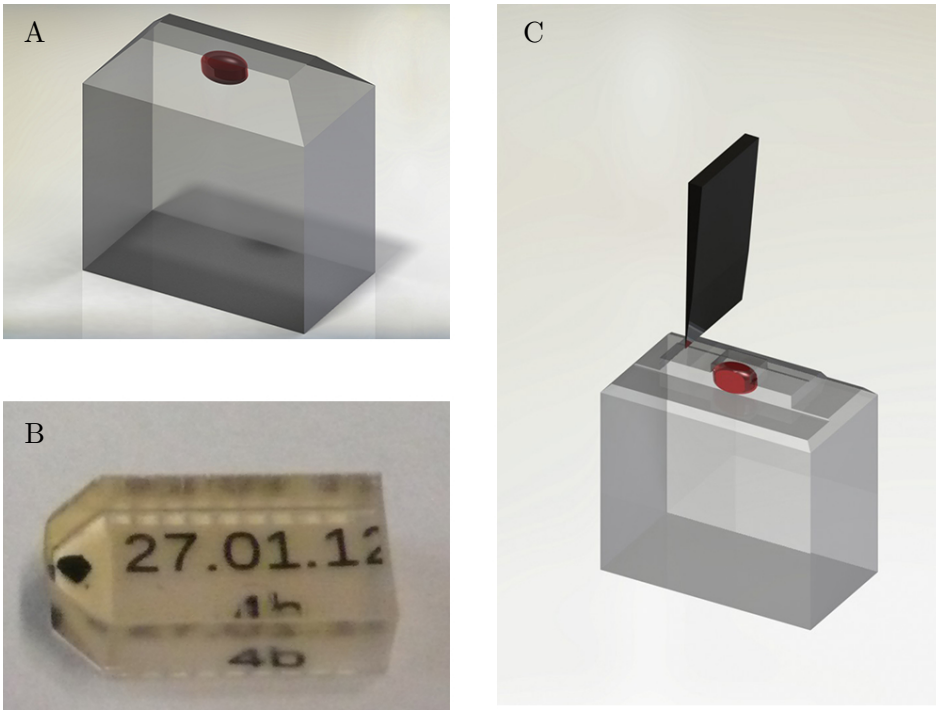

Figure 6.3: Illustrations of the preparation steps. Picture A shows a rendering of the epon block with the gloerulus in red. On Picture B the actual epon block with the black stained kidney tissue is visible. Picture C shows a model of the pyramid cut epon block. In order to prepare the glomerulus (red) for dual beam tomography a series of cuts was performed with a razor blade (rough trimming) and a microtome (fine trimming) until the glomerulus was visible under a light microscope.

overnight. Finally, an additional gold layer of ≈30 nm was sputtered on the samples using a conventional sputter coater (Agar Scientific, Essex, United Kingdom). The gold layer improves the conductivity and uniformly covers all areas of the sample, including the glomerulus.

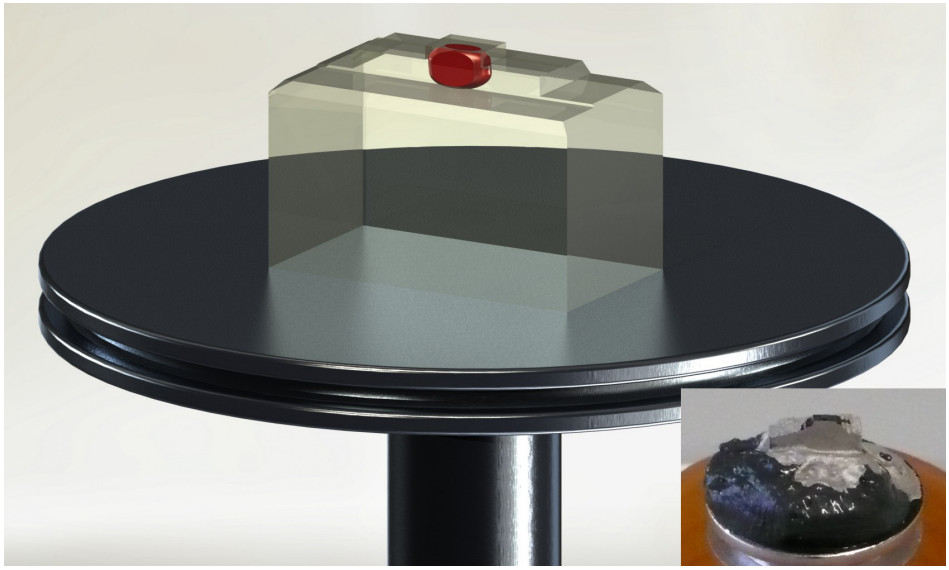

Figure 6.4: Rendered image of the micromachined glomerulus on top of a sample holder ready for dual beam tomography. A finished sample is seen on the photograph in the lower right corner. On the photograph the epon block is glued onto the sample holder with carbon tape and conducting silver.

6.2.3 Serial sectioning and imaging

After the micromachining the sample was studied in the Helios NanoLab dual beam microscope. First, the front surface containing the glomerulus was aligned parallel to the scanning direction of the electron beam. Then the stage was brought into coincident height and tilted to 52°. At this angle the ion beam is parallel to the sample front face while the electron beam is oriented with an angle of 52° to the block face for imaging.

After this initial alignment the cuboid containing the glomerulus was identified using scanning electron imaging. In order to reduce shadowing to increase signal and to reduce drift, block material around the glomerulus was removed with a high beam current of 6.5 nA. Trenches were milled on the left and right sides of the glomerulus. A scanning electron image of the

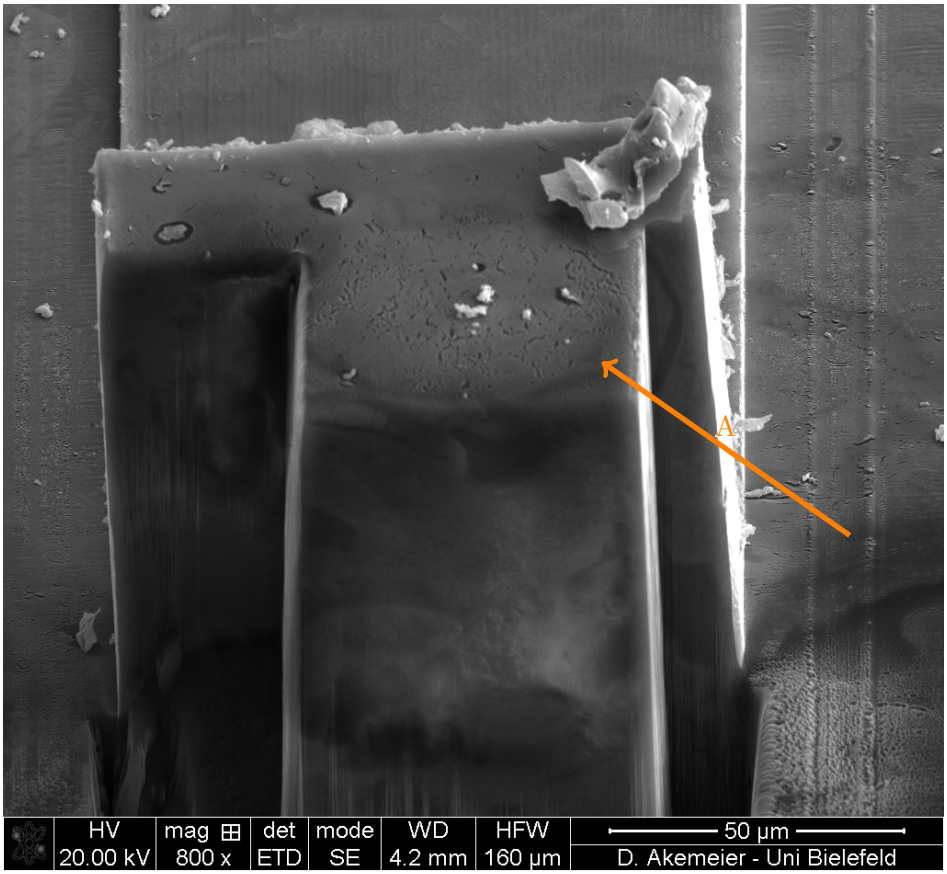

Figure 6.5: Scanning electron picture of the epon embedded glomerulus. The glomerulus is visible in the middle (pointer A).

block after this preparation step is shown in illustration 6.5. The locations where material was removed are clearly visible on the picture by the holes left at the bottom of the block.

When milling inhomogeneous materials, the different milling rates may result in streaks on the imaged surface (curtaining). To reduce these effects a sacrificial platinum layer of 300 nm was deposited on the top surface of the

sample using the gas injection system. Additionally increasing the milling time per slice shifts curtain-deformations to peripheral parts of the block face, not relevant for imaging and reconstruction.

As a final preparation step the front surface was polished with a decreased ion current (2.8 nA). The polished front face is depicted in illustration 6.6. Serial sectioning and imaging was performed by sequential milling and imaging of the emerging sample surface. In contrast to the bulk rough cutting of excess material, the target volume was finely sputtered by removing slice after slice. For this purpose, an etching mode called 'cleaning cross section' was used. This application automatically segments the target volume into slices according to the ion beam spot size. The chosen beam current resulted in slice thicknesses between 30 nm and 100 nm. The thickness was fine controlled through the 'yshift' parameter in the advanced settings of the pattern. By acquiring SEM images after each slice, a complete dataset of images of a specific volume was obtained.

Scanning electron microscope images were acquired with a low accelerator voltage of 3 kV to increase surface sensitivity. Other studies showed optimal imaging parameters at 2 kV [Arm09]. However, testing with our machine revealed a significant drop in resolution when switching to an even lower acceleration voltage. To get contrast rich images from the heavy metal staining an in-lens back scattered electron detector was used. It was found that for kidney samples the optimal images were obtained between electron currents of 0.79 nA and 1.1 nA. A scanning electron micrograph of the polished front surface using these parameters is shown in illustration 6.6.

6.2.4 Image processing

The raw image series were converted into the mrc container file format using the ImageJ software. Afterwards, the mrc files were imported into the Amira software package (FEI Company, Eindhoven, The Netherlands). The use of the mrc format is not necessary for the segmentation, but it allows an easier data transfer between different segmentation software programs. While the segmentation was mostly done using Amira, movie creation and image rendering was performed with the Avizo software package (Visualisation Science Group, Merignac, France).

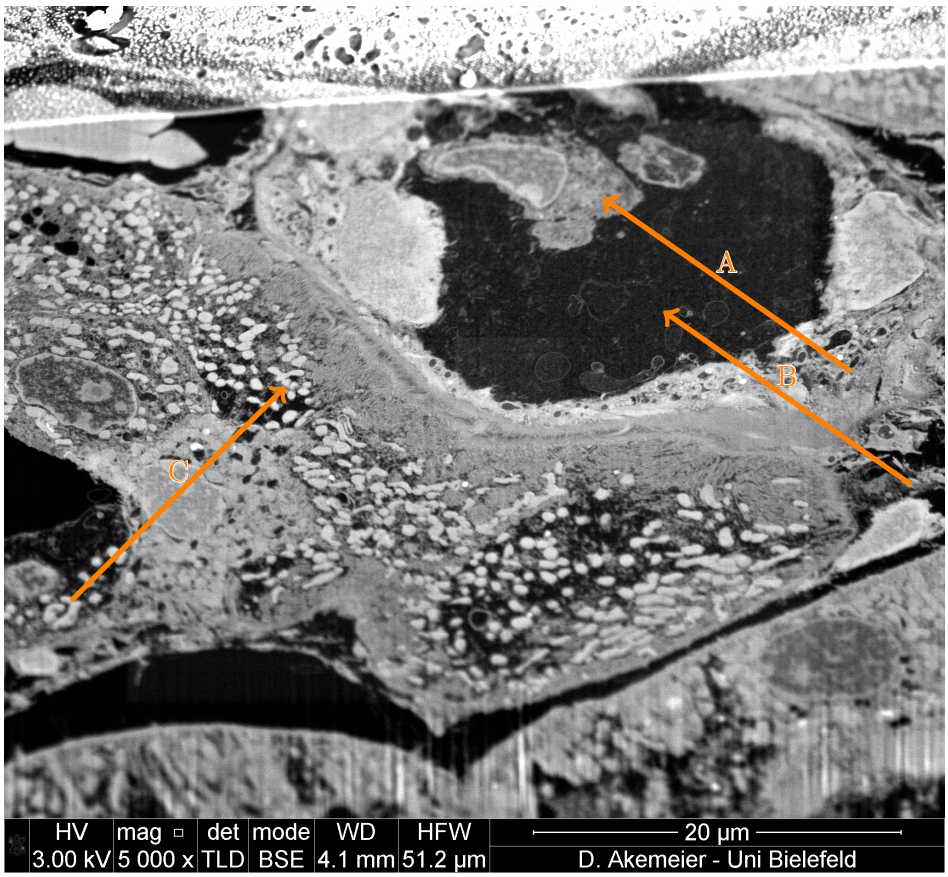

Figure 6.6: High resolution image of the polished front face of the epon block containing the glomerulus. Pointer A indicates the glomerulus, pointer B the Bowman's capsule and pointer C indicates heavely stained mitochondria.

To faciliate comparisons of the scanning electron microscopy images with transmission electron micrographs, the contrast of the images was inverted. The series of two-dimensional images were stacked to create a three-dimensional volume. Afterwards, the image alignment routine was used. This routine corrects small shifts between pictures that are the result of image drifts. During imaging the samples are tilted relative to the electron beam. Hence, the y-dimension of the image pixels is compressed. This is corrected through an angular correction routine.

6.3 Results

6.3.1 Reconstruction of the overview stack

As a measure for the resolution of the overview stack, a biological structure was chosen. In the overview stack single podocyte feet processes were clearly visible and usually had a diameter of at least two pixels. Having a pixel size of 50 nm, this sets the practical resolution of the overview stack to ca. 100 nm. The images for the overview stack were acquired at 2500× magnification and the total analysed volume was $2.7 \times 10^4\,\mu m^3$. The voxel size was nearly isotropic with 50 nm in x-, 63.5 nm in y- and 58.1 nm in z-dimension.

The volume of Bowman's space was cropped from the entire stack, which comprised images of the whole glomerulus and its surrounding capsule. Exemplary images from the stack are found in illustration 6.7. Afterwards, semi-manual segmentation of capillaries, podocytes and the urinary space was performed using the segmentation editor implemented in the Amira software.

The overview stack contained eight complete podocyte cells as well as three unconnected capillaries. Images from the stack are shown in illustration 6.7. Three podocyte cells (pink, red, blue), a capillary (green) as well as the urinary space (yellow) between podocytes and capillaries were reconstructed as a 3D model and are shown in illustration 6.8.

The volume and surface area of segmented objects can be measured using Amira. Podocyte surface areas were smaller than the surface area of the capillary and of the urinary space, whereas the volume of the podocytes

were similar to the volume of the capillary and larger than the volume of the urinary space. The measured values are found in table 6.1.

Table 6.1: Surface and volume measurements of the overview stack

	Area /nm^2	Volume /nm^3
Podocyte	1.38×10^9	2×10^{11}
	8.3×10^8	2.3×10^{11}
	7×10^8	2.9×10^{11}
Capillary	2.19×10^9	3.2×10^{11}
Urinary space	2.95×10^{10}	2×10^{11}

The total volume of the urinary space, filling the complete Bowman's space, would be larger, but for clarity of the 3D model only a part was segmented. Certain structural features, which are impossible to analyse exclusively from 2D sections, can be readily interpreted from the 3D reconstructions. Apart from direct cellular contacts that podocytes form with adjacent cells and capillaries, they possess long and thin cellular extensions that contact distant cells and capillaries, creating an intercellular network within the glomerulus. The cellular extension can be seen on Figure 6.9.

When analysing the interface between reconstructed podocytes and capillaries, prominent cavities between the basement membrane and the podocyte foot processes were found. These were located underneath the podocyte cell body at the interface between podocyte and capillary. Illustration 6.10 shows a magnified image of this interface, with the cavities indicated by arrows. Furthermore, the urinary space was reconstructed, and it was found to be continuous between podocytes as well as podocytes and capillaries. The reconstruction can be seen on Figure 6.8B.

6.3.2 Reconstruction of the high magnification stack

After analysing the overview stack images of the glomerulus, a second image stack using a 6.4 fold higher magnification (16000×) was acquired, which allowed identification and analysis of a specific area of the glomerular

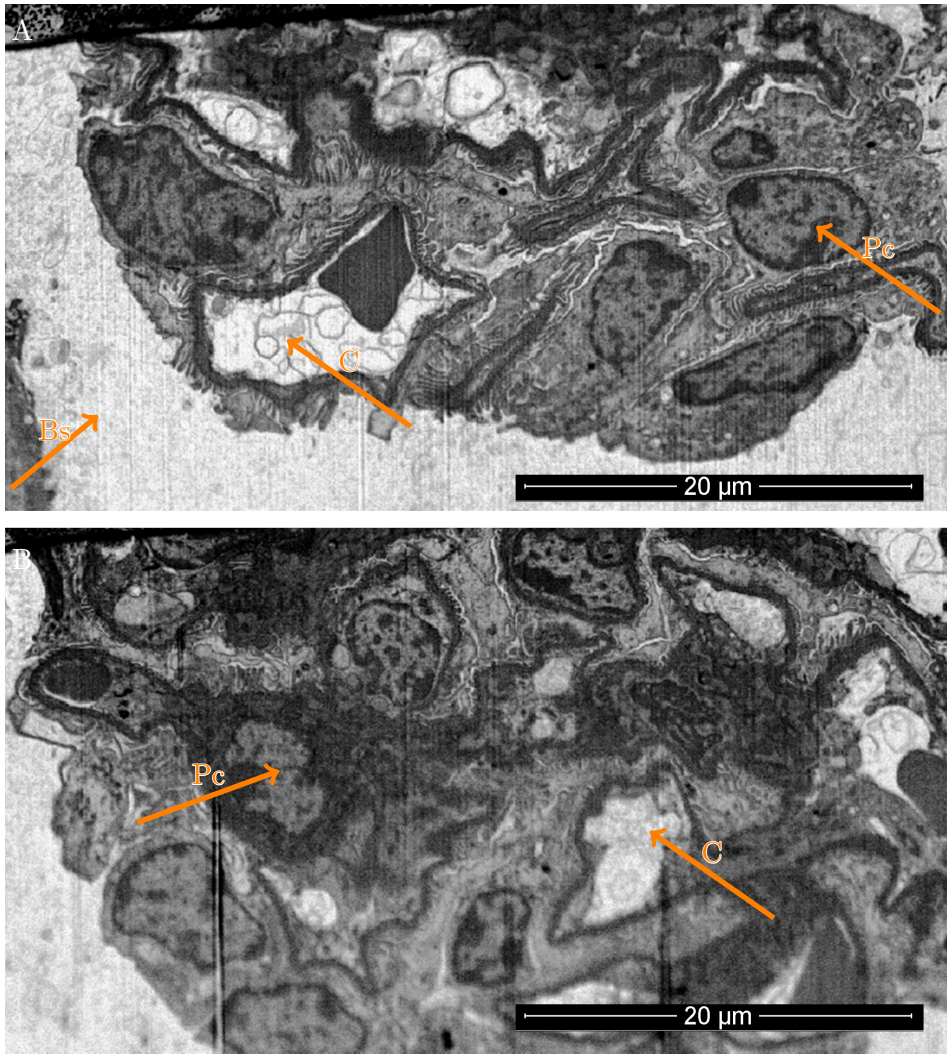

Figure 6.7: Electron micrographs from the cropped and inverted overview stack. Picture A is picture 101 of the image stack, picture B the last image of the stack with image number 202. On picture B the Bowman's space is clearly visible (Bs). On both pictures capillary (C) and podocye cells (Pc) are visible.

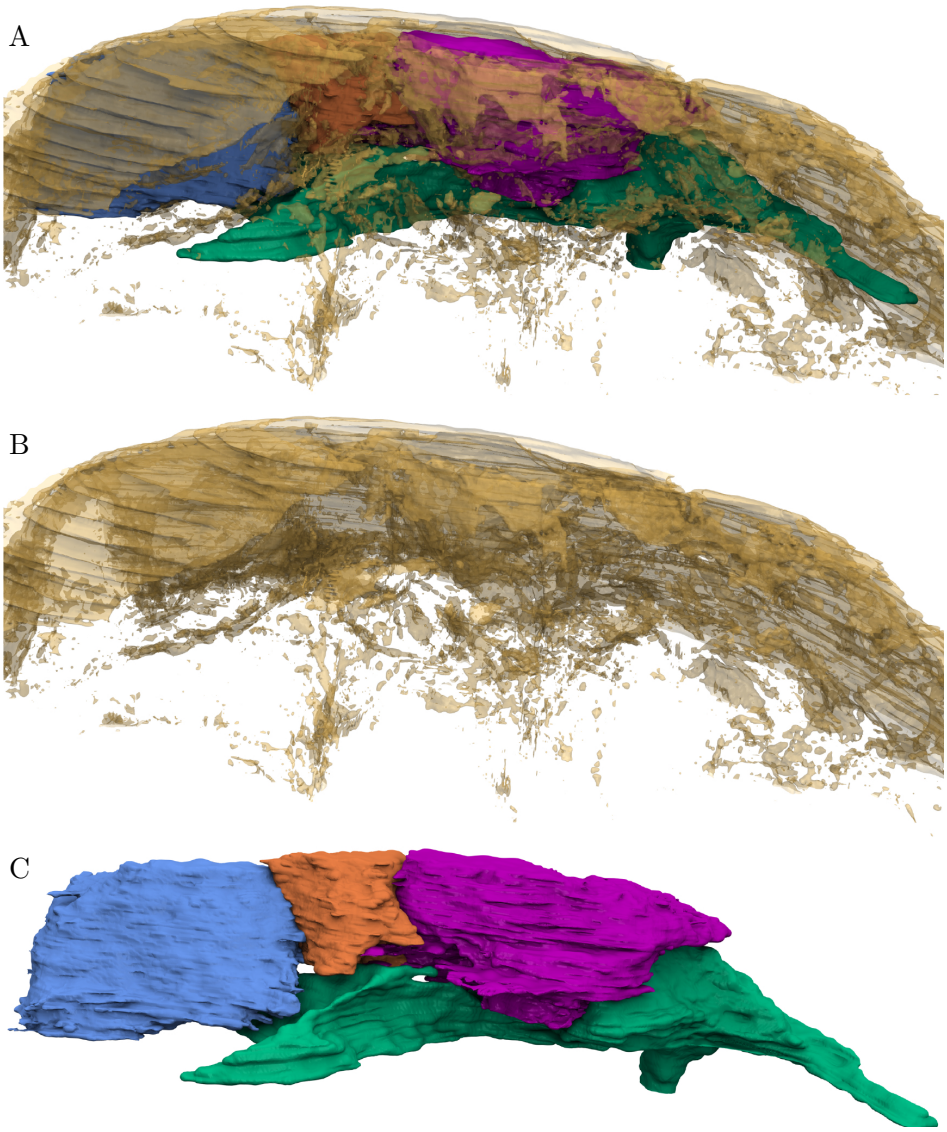

Figure 6.8: 3D visualisation of parts of the glomerulus from the overview image stack. A: A surface rendered 3D volume displaying the urinary space (yellow), a capillary (green) and three podocyte cells (pink, red, blue). B: A surface rendered 3D volume displaying the urinary space. Note the complicated network the urinary space forms inside the glomerulus by connecting the interior of the glomerulus to Bowman's space that surrounds it. C: A surface rendered 3D volume displaying a capillary (green), and three complete podocyte cells.

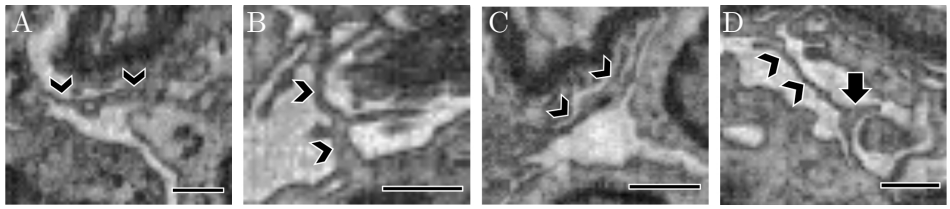

Figure 6.9: Electron micrographs from different locations of the overview stack highlighting cellular podocyte extensions (arrowheads) that exist throughout the glomerulus. On subimage D a synapse-like structure (fat arrow) was found. Scale bars: 1 µm.

filtration interface between podocytes and capillaries.

In this image stack the voxel size was 6.3 nm in x-, 7.9 nm in y- and 33 nm in z-dimension. The overall analysed volume was 136 μm^3. For the high magnification stack, biological membranes were chosen as a feature specific measure for the resolution. Single lipid bilayers usually consisted of 3 pixels in the images, which results in a practical resolution of $\approx$ 18.9 nm.

In the high magnification stack it was possible to visualise the 3D structure of the filtration barrier between capillaries and podocytes. The podocyte cell body, basement membrane and endothelial fenestrations were semi-manually segmented. Endothelial fenestrations (orange), the centre of the basement membrane (blue) and a part of a podocyte cell body (green) were segmented (Figure 6.11). From the 3D reconstructions it was possible to deduce further structural features of the interface between podocytes and capillaries. Endothelial fenestrations form a complex network on the inside of the capillary (Figure 6.12A). Furthermore, it was possible to clearly resolve the central part of the glomerular basement membrane (blue) (Figure 6.11). In the 3D reconstructions podocyte feet processes formed distinct channels between the feet processes and the glomerular basement membrane (Figure 6.12 A-B).

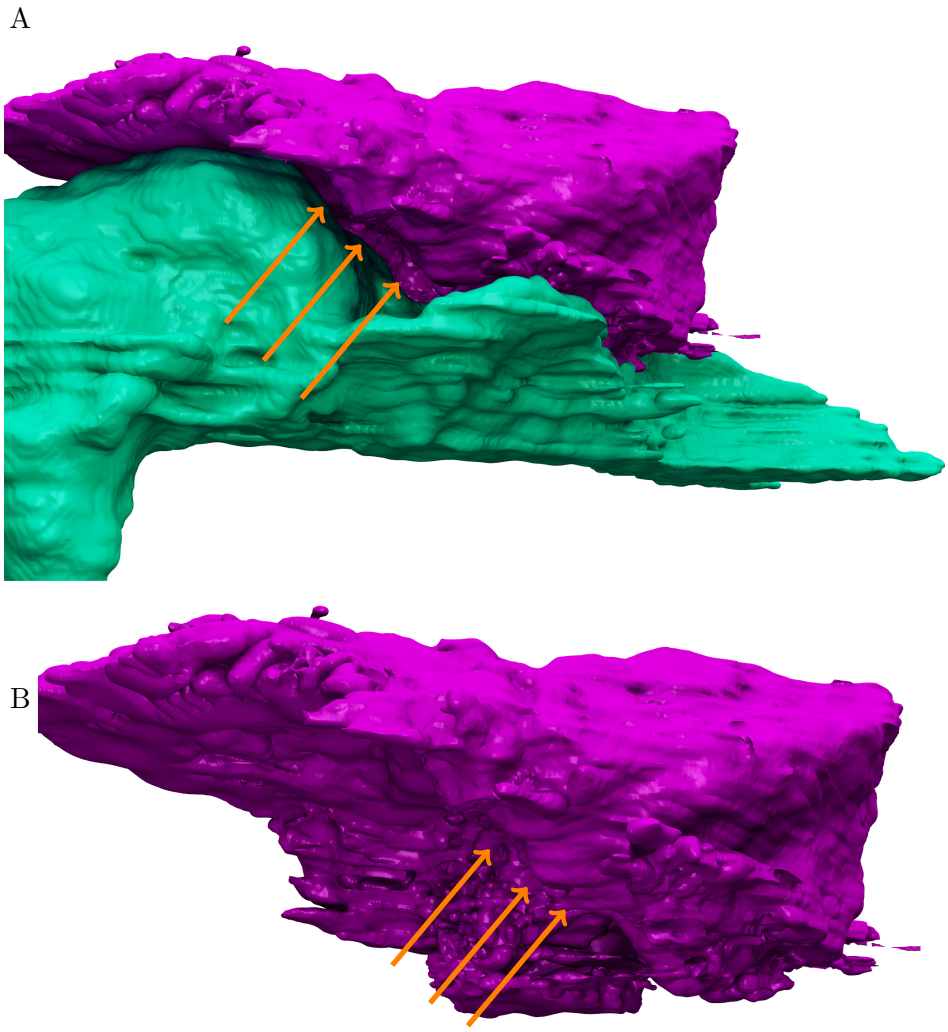

Figure 6.10: Magnified images of the interface between a podocyte cell and a capillary. A: The podocyte and the capillary with arrows pointing at the location of the cavity. B: The podocyte cells with arrows indicating the same region. The capillary is connected to the urinary space, which can be seen by the rendering of the urinary space in illustration 6.8B.

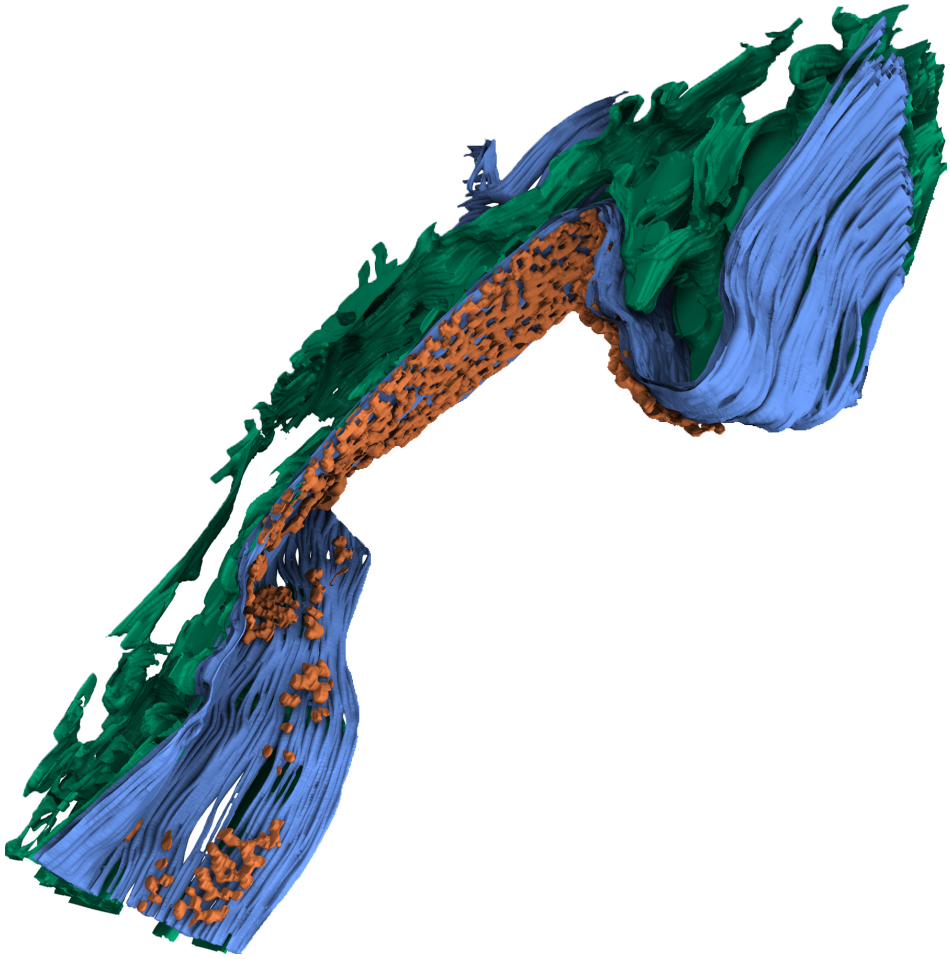

Figure 6.11: Reconstruction of the filtration membrane, with the endothelial fenestration in orange, the basement membrane in blue and part of the podocyte cell body in green. A further magnified view of the middle area with the high density of fenestrations is shown in illustration 6.12.

6.3.3 Biological interpretation of the datasets

The interpretation of the obtained data from a cell biological point of view was done in close cooperation with Christoph Wigge from the Buchmann Institute for Molecular Life Science, Goethe University Frankfurt. The glomerular volume analysed for this work is the largest analysed volume of wild type mouse glomerulus with scanning electron resolution ever done.

The ultrastructural analysis of the glomerulus revealed morphological features that have not been described before. In the overview stack long ($> 1\,\mu m$) and thin ($< 150\,nm$) podocyte extensions were found. They contact distant cells and capillaries form an intercellular network inside the glomerulus. In one case, podocyte extensions appeared similar to a neuronal synapse, but the remaining structures were uniformly stained and further microscopic features could not be recognised. These structures were found infrequently throughout the glomerulus and the probability of detecting them in ultra thin 2D kidney sections is very low. This might explain why they have not been described previously. Electron micrographs of the corresponding features are found in illustration 6.9.

On the biological function of these structures one may only speculate. They may increase tissue stability or serve in signal transduction between podocytes. Furthermore, when analysing the 3D reconstruction of the filtration barrier, podocytes directly adjacent to capillaries were found that form a cavity between their cell body and the capillary endothelium (Figure 6.10). These cavities may form a reservoir where primary filtrate is collected, but the physiological function of this remains unclear. Since the surface area of the podocyte forming this reservoir is almost twofold larger ($1.38 \times 10^9\,nm^2$) than the surface area of the other podocytes ($8.3 \times 10^8\,nm^2$, $7 \times 10^8\,nm^2$) and a pronounced number of podocyte feet processes are facing in this reservoir, it is very probable that this has a specific role in further filtration.

In addition, the reconstructed urinary space was found to be continuous from the inside of the glomerulus to the outside of Bowman's space. In rats it has been previously described that small pores ($1.3 \times 0.3\,\mu m$) exist that hinder filtrate flow from the subpodocyte space into Bowman's space [Nea05]. In the large reconstructed volume, structures similar to these pores

were not found. If these pores were present in wild type mouse kidney, the probability of identifying them is higher in a large reconstructed volume.

In previous studies the alignment of serial sections was performed manually, which is also a source of artefacts. In addition to that, Neal et al. [Nea05] used perfusion fixation whereas in this study small kidney tissue pieces were fixated using a bulk fixation protocol. It is possible that these structures were not found due to fixation artefacts occurring in the protocol. It is well known that chemical fixation especially of tissues creates fixation artefacts, because of slow diffusion of the fixative. To avoid these effects and to preserve native morphology, cryo fixation methods are the standard in structural biology. There are promising approaches to apply these methods to dual beam microscopes [Rig12].

The ultrastructural analysis of the filtration barrier in the high magnification stack revealed that the surface rendered 3D view of the complex network of endothelial fenestrations had a different appearance than that of critical point dried scanning electron microscope images. Conventional scanning electron microscope images are most likely visualising fenestrations longitudinally, whereas here a cross sectional view was reconstructed. In the cross section profile they appeared as alternating spherical tissue tubes interspersed with holes. This resulted in fenestrations of elongated shape as well as tubular tissue in between, as shown in the reconstruction. It has been previously described that inside the fenestrations so-called fascines exist that may also be responsible for ultrafiltration [Ros97]. However, in the reconstruction of the endothelial fenestrations these or any other molecular structures that might have a function in further filtration, were observed. In contrast to bulk fixation method, Rostgaard et al. [Ros97] used a vascular perfusion fixation together with an artificial oxygenated blood substitute. In addition, they used another tissue preparation protocol than described here, thus it might be possible that these structures did not stain sufficiently and thus were not visualised in the sample. Furthermore, these single filaments had a diameter of 5 nm - 10 nm, which is below the resolution limit of the image stack of ca. 20 nm.

The slit diaphragm is a thin continuous band of ca. 30 nm width, which covers the capillary in an interdigitating manner. In the reconstruction of the filtration barrier the slit diaphragm between podocyte feet processes

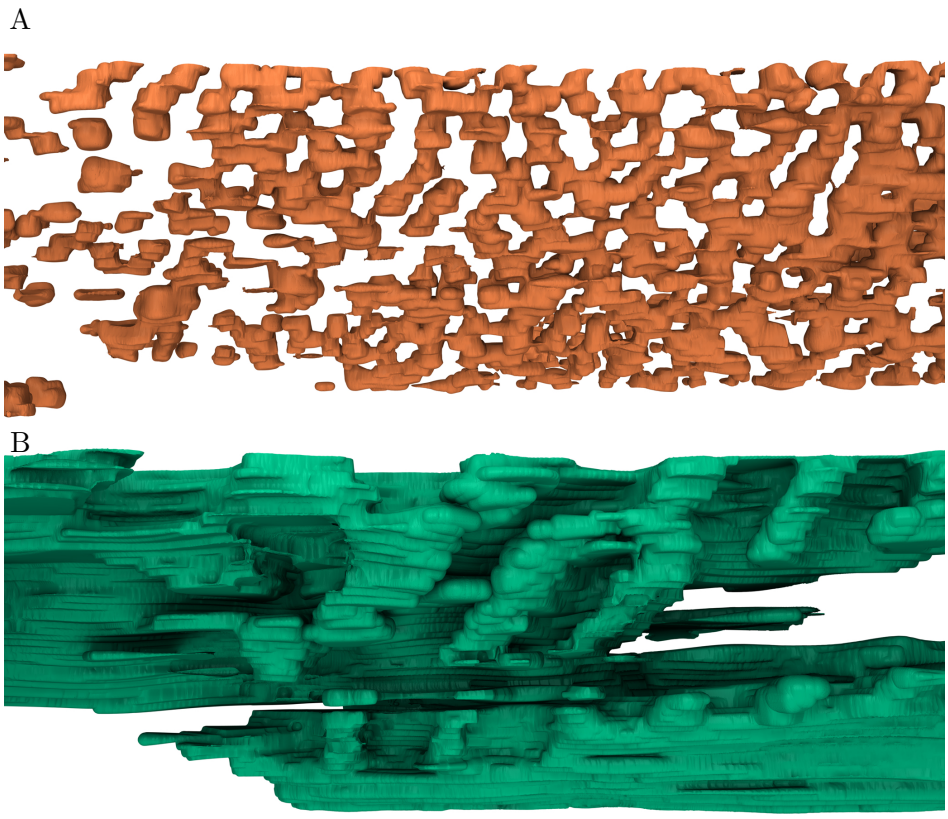

Figure 6.12: A) Surface rendered volume of endothelial fenestrations from illustration 6.11. B) Surface rendered image of the podocyte feet processes from the same region. The podocyte feet processes form channels in z-dimension.

could be identified in some areas as an area of high staining.

Furthermore, in the 3D visualisation of the filtration barrier, podocyte feet processes that face the glomerular basement membrane form a specific network of channels that may conduct the primary filtrate (Figure 6.12).

6.4 Summary and Outlook

The work presented in this chapter demonstrates the possibilities of dual beam tomography. The combination of sequential milling of resin embedded biological material and imaging the surface with a scanning electron microscope allows for structural analysis of glomerular tissue. In addition, it is possible to assess the morphology of the filtration barrier between podocytes and capillaries in detail. The here presented surface rendered 3D structure of a wild type mouse glomerulus as well as the high magnification reconstruction of a specific part of the ultrafiltration interface shows the potential of the method.

In many biological as well as medical applications it is important to quantitatively measure biological structures. These measurments may be volume, surface area or the number of cells or other structures of interest. Especially pathologic alterations are often related to changes in these parameters. Up to now stereological methods have been proved to provide the most accurate results. Nevertheless, the method has two major drawbacks. First, the correct application of the method is not trivial and requires high technical as well as microscopic experience. Second, the acquired results are indirect estimations and not direct physical measurements. The method of dual beam tomography further helps to overcome these limitations and offers the analysis of the 3D morphology of the structure of interest simultaneously. It has been shown that counting synapses with dual beam tomography and stereology gives similar results without the large variability of stereology measurements [MP09]. A further strong advantage of a quantitative analysis of biological structures by dual beam tomography is the simultaneous acquisition of a 3D image stack where morphologic analysis can be performed.

In general, the method of dual beam tomography as an imaging method

can be settled between whole organ micromagnetic resonance imaging and transmission electron tomography. It has a clear limitation in the size of structures that can efficiently be milled and imaged compared to magnetic resonance imaging, but it provides a much better resolution. The possible resolution of dual beam tomography is below transmission electron microscopy imaging. However, transmission electron tomography reconstructions are limited to several hundreds of nanometers in z dimension. Here dual beam tomography was applied on a tissue of interest, namely mouse glomerulus. Previously unseen structural features became visible in this new resolution to volume window.

For future research focusing on further improving the technical aspects of tissue preparation should increase the applications in morphological studies. Especially the combination of dual beam microscopy with cryo focused ion beam has great potential. Furthermore, the application of this method in the study of the structure of pathologic alterations during kidney diseases is promising.

7 Outlook

In this thesis a dual beam microscope was used to work on a wide range of topics. The one connection between all these projects is manipulation and imaging at the nanoscale. A dual beam offers a combination of both in one device. This makes it very flexible. All applications presented here rely on these advantages. However, out of the box a dual beam microscope is lacking some applications to fully utilise its potential. As part of this thesis, these were created either through manual routines (work arounds) or through self programmed scripts. With them the applications described in this work as well as many other were made possible. However, for the average user this is no real option, as creating sophisticated methods for a complex device requires a deep understanding of the device and is time consuming. Therefore, a great improvement for all fields even slightly interacting with dual beam devices (and by now nanotechnology has applications in nearly every field) would be an improved out of the box software environment. By including the software, developed during this thesis and possibly other automation routines into the default software (including a good documentation and software guides), it would be possible to help the scientific process greatly.

The potential for advancing dual beam technology through software alone is great. There are a lot more options for advancement beyond automation routines. There are multiple options to integrate these programs with the rest of the dual beam software. The development of simplified subprograms or building blocks, that interact with the main control interface directly would be ideal.

Their functionality is best described using an example process. Here the creation of bio tomograms is chosen. For better understanding, the buildings blocks approach is compared with a one program solution. In order to record a tomogram, many different operations have to be performed, both

before as preparation and during recording. In the one program solution a separate software is started. This software then takes control over the dual beam device. Using the controls offered by this software, the milling and imaging parameters as well as the preparation cuts are defined. Afterwards, the software performs all process steps automatically. While this is an improvement over manual preparation and image acquisition, the separate program approach has a significant drawback. The flexibility offered by the focused ion beam is lost. However, exactly this degree of flexibility allowed for many of the presented applications in this thesis.

The alternative approach would be to give the user access to a library of subscripts that integrate with the machine. While each of those subscripts starts an automated process, it should be possible to pause the subscripts during execution or after a process is finished and edit process parameters. The subprocesses could for example be arranged in a playlist. This way it would be easy to start only a subsection of the tomography process or exchange a subscript for a better fitting variant. By making these subscripts editable, the flexibility of the system is kept, wile running all scripts in a fixed order emulates the one software solution.

The next step would be to offer users the ability to publish and share subscripts, for example through a specific open access journal, that focusses on these scripts and would act as a database for their documentations as well. It should then be possible to send these publications to the dual beam device, which automatically would add the script to the users script library. Citing a subscript publication in a regular paper would give other users the possibility to easily use methods established in other workgroups, while still giving credit to the author using citations.

Bibliography

[Abb73] Abbe, E: Beiträge zur Theorie des Mikroskops und der mikroskopischen Wahrnehmung. *Archiv für mikroskopische Anatomie* (1873), URL http://www.springerlink.com/index/k7154700k345404p.pdf
(Zitiert auf Seite 21)

[Arm09] Armer, Hannah E J; Mariggi, Giovanni; Png, Ken M Y; Genoud, Christel; Monteith, Alexander G; Bushby, Andrew J; Gerhardt, Holger und Collinson, Lucy M: Imaging transient blood vessel fusion events in zebrafish by correlative volume electron microscopy. *PloS one* (2009), Bd. 4(11): S. e7716, URL http://www.pubmedcentral.nih.gov/articlerender.fcgi?artid=2769265&tool=pmcentrez&rendertype=abstract
(Zitiert auf Seiten 93, 95, and 100)

[Baf11] Baffou, Guillaume und Rigneault, Hervé: Femtosecond-pulsed optical heating of gold nanoparticles. *Physical Review B* (2011), Bd. 84(3): S. 1–13, URL http://link.aps.org/doi/10.1103/PhysRevB.84.035415
(Zitiert auf Seite 83)

[Bas02] Basting, Dirk; Pippert, Klaus; Stamm, Uwe und Ag, Lambda Physik: History and future prospects of excimer laser technology (2002), Bd. 43(43): S. 14–22
(Zitiert auf Seite 43)

[Bee11] Beeman, Scott C; Zhang, Min; Gubhaju, Lina; Wu, Teresa; Bertram, John F; Frakes, David H; Cherry, Brian R und Bennett, Kevin M: Measuring glomerular number and size in perfused kidneys using MRI. *American journal of physiology.*

Renal physiology (2011), Bd. 300(6): S. F1454–7, URL http://www.ncbi.nlm.nih.gov/pubmed/21411479
(Zitiert auf Seiten 92 and 93)

[Boy02] Boyd, Robert W.: *Nonlinear OpticsÂ (Google eBook)*, Academic Press (2002), URL http://books.google.com/books?hl=en&lr=&id=3vHb7WGXmSQC&pgis=1
(Zitiert auf Seite 46)

[Bur77] Burnett, N. H.; Baldis, H. a.; Richardson, M. C. und Enright, G. D.: Harmonic generation in CO2 laser target interaction. *Applied Physics Letters* (1977), Bd. 31(3): S. 172, URL http://link.aip.org/link/APPLAB/v31/i3/p172/s1&Agg=doi
(Zitiert auf Seite 43)

[Bus11] Bushby, Andrew J; P'ng, Kenneth M Y; Young, Robert D; Pinali, Christian; Knupp, Carlo und Quantock, Andrew J: Imaging three-dimensional tissue architectures by focused ion beam scanning electron microscopy. *Nature protocols* (2011), Bd. 6(6): S. 845–58, URL http://www.ncbi.nlm.nih.gov/pubmed/21637203
(Zitiert auf Seiten 93 and 96)

[Chi13] Chityala, Ravishankar; Pudipeddi, Sridevi; Arensten, Luke und Hui, Susanta: Segmentation and visualization of a large, high-resolution micro-CT data of mice. *Journal of digital imaging* (2013), Bd. 26(2): S. 302–8, URL http://www.ncbi.nlm.nih.gov/pubmed/22766797
(Zitiert auf Seite 95)

[Cor93] Corkum, PB: Plasma perspective on strong field multiphoton ionization. *Physical Review Letters* (1993), Bd. 71(13): S. 1994–1997, URL http://link.aps.org/doi/10.1103/PhysRevLett.71.1994
(Zitiert auf Seite 46)

[Dre01] Drescher, M; Hentschel, M; Kienberger, R; Tempea, G; Spielmann, C; Reider, G a; Corkum, P B und Krausz,

F: X-ray pulses approaching the attosecond frontier. *Science (New York, N.Y.)* (2001), Bd. 291(5510): S. 1923–7, URL http://www.ncbi.nlm.nih.gov/pubmed/11239146
(Zitiert auf Seite 43)

[Epp97] Eppink, Andre T. J. B. und Parker, David H.: Velocity map imaging of ions and electrons using electrostatic lenses: Application in photoelectron and photofragment ion imaging of molecular oxygen. *Review of Scientific Instruments* (1997), Bd. 68(9): S. 3477,
(Zitiert auf Seite 81)

[Esc75] Escovitz, W H; Fox, T R und Levi-Setti, R: Scanning transmission ion microscope with a field ion source. *Proceedings of the National Academy of Sciences of the United States of America* (1975), Bd. 72(5): S. 1826–8, URL http://www.pubmedcentral.nih.gov/articlerender.fcgi?artid=432639&tool=pmcentrez&rendertype=abstract
(Zitiert auf Seite 8)

[Eve60] Everhart, TE und Thornley, RFM: Wide-band detector for micro-microampere low-energy electron currents. *Journal of scientific instruments* (1960), Bd. 246, URL http://iopscience.iop.org/0950-7671/37/7/307
(Zitiert auf Seite 11)

[For07] Fore, Samantha; Yuen, Yin; Hesselink, Lambertus und Huser, Thomas: Pulsed-interleaved excitation FRET measurements on single duplex DNA molecules inside C-shaped nanoapertures. *Nano letters* (2007), Bd. 7(6): S. 1749–56, URL http://www.ncbi.nlm.nih.gov/pubmed/17503872
(Zitiert auf Seite 24)

[Fra61] Franken, PA; Hill, AE; Peters, CW und Weinreich, G: Generation of Optical Harmonics. *Physical Review Letters* (1961), Bd. 7(1): S. 118–120, URL http://link.aps.org/doi/10.1103/PhysRevLett.7.118
(Zitiert auf Seite 43)

[Goh05] Gohle, Christoph; Udem, Thomas; Herrmann, Maximilian; Rauschenberger, Jens; Holzwarth, Ronald; Schuessler, Hans A; Krausz, Ferenc und Hänsch, Theodor W: A frequency comb in the extreme ultraviolet. *Nature* (2005), Bd. 436(7048): S. 234–7, URL http://dx.doi.org/10.1038/nature03851
(Zitiert auf Seite 43)

[Hoy03] Hoy, Wendy E; Douglas-Denton, Rebecca N; Hughson, Michael D; Cass, Alan; Johnson, Kelli und Bertram, John F: A stereological study of glomerular number and volume: preliminary findings in a multiracial study of kidneys at autopsy. *Kidney international. Supplement* (2003), Bd. 63(83): S. S31–7, URL http://www.ncbi.nlm.nih.gov/pubmed/12864872
(Zitiert auf Seite 93)

[Hua10] Huang, Jer-Shing; Callegari, Victor; Geisler, Peter; Brüning, Christoph; Kern, Johannes; Prangsma, Jord C; Wu, Xiaofei; Feichtner, Thorsten; Ziegler, Johannes; Weinmann, Pia; Kamp, Martin; Forchel, Alfred; Biagioni, Paolo; Sennhauser, Urs und Hecht, Bert: Atomically flat single-crystalline gold nanostructures for plasmonic nanocircuitry. *Nature communications* (2010), Bd. 1: S. 150, URL http://www.ncbi.nlm.nih.gov/pubmed/21267000
(Zitiert auf Seiten 76 and 90)

[Iwa09] Iwai, H.: Roadmap for 22nm and beyond (Invited Paper). *Microelectronic Engineering* (2009), Bd. 86(7-9): S. 1520–1528, URL http://linkinghub.elsevier.com/retrieve/pii/S0167931709002950
(Zitiert auf Seite 89)

[Jac02] Jackson, John David: *Klassische Elektrodynamik.*, Gruyter (2002), URL http://www.amazon.com/Klassische-Elektrodynamik-John-David-Jackson/dp/3110165023
(Zitiert auf Seite 44)

[Joh72] Johnson, PB und Christy, RW: Optical Constants of the Noble

Metals. *Physical Review B* (1972), Bd. 1318(1970), URL http://prb.aps.org/abstract/PRB/v6/i12/p4370_1
(Zitiert auf Seite 51)

[Joh84] Johnson,Â R.Â C. und Jasik,Â H.: Antenna engineering handbook /2nd edition/. *New York* (1984), URL http://adsabs.harvard.edu/abs/1984mgh..book.....J
(Zitiert auf Seite 47)

[Kan10] Kandula, Dominik; Gohle, Christoph; Pinkert, Tjeerd; Ubachs, Wim und Eikema, Kjeld: Extreme Ultraviolet Frequency Comb Metrology. *Physical Review Letters* (2010), Bd. 105(6): S. 1–4, URL http://link.aps.org/doi/10.1103/PhysRevLett.105.063001
(Zitiert auf Seite 43)

[Kim08] Kim, Seungchul; Jin, Jonghan; Kim, Young-Jin; Park, In-Yong; Kim, Yunseok und Kim, Seung-Woo: High-harmonic generation by resonant plasmon field enhancement. *Nature* (2008), Bd. 453(7196): S. 757–60, URL http://www.ncbi.nlm.nih.gov/pubmed/18528390
(Zitiert auf Seiten 3 and 43)

[Kim12] Kim, Seungchul; Jin, Jonghan; Kim, Young-Jin; Park, In-Yong; Kim, Yunseok und Kim, Seung-Woo: Kim et al. reply. *Nature* (2012), Bd. 485(7397): S. E1–E3, URL http://www.nature.com/doifinder/10.1038/nature10979
(Zitiert auf Seite 83)

[Kno08] Knott, Graham; Marchman, Herschel; Wall, David und Lich, Ben: Serial section scanning electron microscopy of adult brain tissue using focused ion beam milling. *The Journal of neuroscience : the official journal of the Society for Neuroscience* (2008), Bd. 28(12): S. 2959–64, URL http://www.ncbi.nlm.nih.gov/pubmed/18353998
(Zitiert auf Seite 93)

[Koc05] Koch, J.; Korte, F.; Bauer, T.; Fallnich, C.; Ostendorf, a. und Chichkov, B.N.: Nanotexturing of gold films by femtosec-

ond laser-induced melt dynamics. *Applied Physics A* (2005), Bd. 81(2): S. 325–328, URL http://www.springerlink.com/index/10.1007/s00339-005-3212-6
(Zitiert auf Seite 49)

[Koc09] Kochumalayil, J. J.; Kochumalayil, J. J; Meiser, A; Soldera, F und Possart, W: Focused ion beam irradiation: morphological and chemical evolution in epoxy polymers (2009), URL http://journals.ohiolink.edu/ejc/article.cgi?issn=01422421&issue=v41i12-13&article=931_fibimaceiep
(Zitiert auf Seite 95)

[Kub87] Kubena, R. L. und Ward, J. W.: Current-density profiles for a Ga+ ion microprobe and their lithographic implications. *Applied Physics Letters* (1987), Bd. 51(23): S. 1960, URL http://link.aip.org/link/APPLAB/v51/i23/p1960/s1&Agg=doi
(Zitiert auf Seite 58)

[Les10] Leser, Vladka; Milani, Marziale; Tatti, Francesco; Tkalec, Ziva Pipan; Strus, Jasna und Drobne, Damjana: Focused ion beam (FIB)/scanning electron microscopy (SEM) in tissue structural research. *Protoplasma* (2010), Bd. 246(1-4): S. 41–8, URL http://www.ncbi.nlm.nih.gov/pubmed/20169456
(Zitiert auf Seite 93)

[L'H93] L'Huillier, A und Balcou, P: High-Order Harmonic Generation in Rare Gases with a 1-ps 1053-nm Laser. *Physical review letters* (1993), Bd. 70(6): S. 774–777, URL http://link.aps.org/doi/10.1103/PhysRevLett.70.774
(Zitiert auf Seite 47)

[Lin96] Linde, D und Schüler, H: Breakdown threshold and plasma formation in femtosecond laser solid interaction. *JOSA B* (1996), Bd. 13(1): S. 216–222, URL http://www.opticsinfobase.org/abstract.cfm?id=33682
(Zitiert auf Seite 83)

[Lip96] Lipp, S; Frey, L; Lehrer, C; Demm, E; Pauth-

NER, S und RYSSEL, H: A comparison of focused ion beam and electron beam induced deposition processes. *Microelectronics Reliability* (1996), Bd. 36(11â12): S. 1779–1782, URL http://www.sciencedirect.com/science/article/pii/0026271496001965
(Zitiert auf Seite 12)

[Lor79] LOREE, T; SZE, R; BARKER, D und SCOTT, P: New Lines in the UV : SRS of Excimer Laser Wavelenghs. *Quantum Electronics, IEEE ...* (1979), (5), URL http://ieeexplore.ieee.org/xpls/abs_all.jsp?arnumber=1070016
(Zitiert auf Seite 43)

[M̈84] MÖLLER, W und ECKSTEIN, W: Tridyn â A TRIM simulation code including dynamic composition changes. *Nuclear Instruments and Methods in Physics ...* (1984), Bd. 2: S. 814–818, URL http://www.sciencedirect.com/science/article/pii/0168583X84903215
(Zitiert auf Seite 55)

[Mai07] MAIER, Stefan Alexander: *Plasmonics: Fundamentals and Applications*, Springer (2007), URL http://www.amazon.com/Plasmonics-Fundamentals-Stefan-Alexander-Maier/dp/0387331506
(Zitiert auf Seite 50)

[McF05] MCFIGGANS, Gordon: Atmospheric science: marine aerosols and iodine emissions. *Nature* (2005), Bd. 433(7026): S. E13; discussion E13–4, URL http://www.ncbi.nlm.nih.gov/pubmed/15703706
(Zitiert auf Seite 43)

[Med12] MEDEIROS, Lia Carolina Soares; DE SOUZA, Wanderley; JIAO, Chengge; BARRABIN, Hector und MIRANDA, Kildare: Visualizing the 3D architecture of multiple erythrocytes infected with Plasmodium at nanoscale by focused ion beam-scanning electron microscopy. *PloS one* (2012), Bd. 7(3): S. e33445, URL http:

//www.pubmedcentral.nih.gov/articlerender.fcgi?artid=3303842&tool=pmcentrez&rendertype=abstract
(Zitiert auf Seite 93)

[MP09] Merchán-Pérez, Angel; Rodriguez, José-Rodrigo; Alonso-Nanclares, Lidia; Schertel, Andreas und Defelipe, Javier: Counting Synapses Using FIB/SEM Microscopy: A True Revolution for Ultrastructural Volume Reconstruction. *Frontiers in neuroanatomy* (2009), Bd. 3(October): S. 18, URL http://www.pubmedcentral.nih.gov/articlerender.fcgi?artid=2784681&tool=pmcentrez&rendertype=abstract
(Zitiert auf Seite 112)

[Nea05] Neal, Christopher R; Crook, Hayley; Bell, Edward; Harper, Steven J und Bates, David O: Three-dimensional reconstruction of glomeruli by electron microscopy reveals a distinct restrictive urinary subpodocyte space. *Journal of the American Society of Nephrology : JASN* (2005), Bd. 16(5): S. 1223–35, URL http://www.ncbi.nlm.nih.gov/pubmed/15829713
(Zitiert auf Seiten 92, 93, 109, and 110)

[Oly12] Olympus America Inc.: Microscopy ressource center (2012), URL http://www.olympusmicro.com
(Zitiert auf Seite 23)

[Orl96] Orloff, Jon: Fundamental limits to imaging resolution for focused ion beams. *Journal of Vacuum Science & Technology B: Microelectronics and Nanometer Structures* (1996), Bd. 14(6): S. 3759, URL http://link.aip.org/link/?JVTBD9/14/3759/1http://link.aip.org/link/?JVB/14/3759/1&Agg=doi
(Zitiert auf Seite 12)

[Pav03] Pavenstädt, Hermann; Kriz, Wilhelm und Kretzler, Matthias: Cell biology of the glomerular podocyte. *Physiological reviews* (2003), Bd. 83(1): S. 253–307, URL http://www.ncbi.nlm.nih.gov/pubmed/12506131
(Zitiert auf Seite 92)

[Pfua] Pfullmann, N; Waltermann, C; Noack, M und Rausch, S:

Bow tie nano-antenna assisted generation of extreme ultraviolet radiation
(Zitiert auf Seite 80)

[Pfub] Pfullmann, Nils; Waltermann, Christian; Kova, Milutin; Knittel, Vanessa; Bratschitsch, Rudolf; Akemeier, Dieter; Andreas, H; Leitenstorfer, Alfred und Morgner, Uwe: Nano-antenna assisted harmonic generation: S. 1–5
(Zitiert auf Seite 80)

[Pfu12] Pfullmann, Nils: *Nano-antenna-assisted high-order harmonic generation*, Dissertation, University of Hannover (2012)
(Zitiert auf Seiten 48, 50, 51, and 80)

[Rig12] Rigort, Alexander; Bäuerlein, Felix J B; Villa, Elizabeth; Eibauer, Matthias; Laugks, Tim; Baumeister, Wolfgang und Plitzko, Jürgen M: Focused ion beam micromachining of eukaryotic cells for cryoelectron tomography. *Proceedings of the National Academy of Sciences of the United States of America* (2012), Bd. 109(12): S. 4449–54, URL http://www.pubmedcentral.nih.gov/articlerender.fcgi?artid=3311327&tool=pmcentrez&rendertype=abstract
(Zitiert auf Seite 110)

[Ros97] Rostgaard, J und Qvortrup, K: Electron microscopic demonstrations of filamentous molecular sieve plugs in capillary fenestrae. *Microvascular research* (1997), Bd. 53(1): S. 1–13, URL http://www.ncbi.nlm.nih.gov/pubmed/9056471
(Zitiert auf Seite 110)

[Rou09] Roussel, LY; Stokes, D; Gestman, Ingo; Darus, Mark und Young, Richard: Extreme high resolution scanning electron microscopy (XHR SEM) and beyond. *Scanning Microscopy* (2009), Bd. 7378: S. 73780W–73780W–9, URL http://proceedings.spiedigitallibrary.org/proceeding.aspx?articleid=1339655
(Zitiert auf Seite 91)

[Sch97] Schafer, Kenneth und Kulander, Kenneth: High Harmonic

Generation from Ultrafast Pump Lasers. *Physical Review Letters* (1997), Bd. 78(4): S. 638–641, URL http://link.aps.org/doi/10.1103/PhysRevLett.78.638
(Zitiert auf Seiten 47 and 86)

[Siv12] Sivis, M; Duwe, M; Abel, B und Ropers, C: Nanostructure-enhanced atomic line emission. *Nature* (2012), Bd. 485(7397): S. E1–2; discussion E2–3, URL http://www.ncbi.nlm.nih.gov/pubmed/22575967
(Zitiert auf Seite 81)

[Tao90] Tao, Tao; Ro, JaeSang; Melngailis, John; Xue, Ziling und Kaesz, Herbert D: Focused ion beam induced deposition of platinum (1990)
(Zitiert auf Seite 12)

[Ude02] Udem, Th; Holzwarth, R und Hänsch, T W: Optical frequency metrology. *Nature* (2002), Bd. 416(6877): S. 233–7, URL http://dx.doi.org/10.1038/416233a
(Zitiert auf Seite 43)

[Uib07] Uiberacker, M; Uphues, Th; Schultze, M; Verhoef, a J; Yakovlev, V; Kling, M F; Rauschenberger, J; Kabachnik, N M; Schröder, H; Lezius, M; Kompa, K L; Muller, H-G; Vrakking, M J J; Hendel, S; Kleineberg, U; Heinzmann, U; Drescher, M und Krausz, F: Attosecond real-time observation of electron tunnelling in atoms. *Nature* (2007), Bd. 446(7136): S. 627–32, URL http://www.ncbi.nlm.nih.gov/pubmed/17410167
(Zitiert auf Seite 43)

[War87] Ward, J. W.: Computer simulation of current density profiles in focused ion beams. *Journal of Vacuum Science & Technology B: Microelectronics and Nanometer Structures* (1987), Bd. 5(1): S. 169, URL http://link.aip.org/link/?JVB/5/169/1&Agg=doi
(Zitiert auf Seite 58)

[Wil77] Wilson, W.D.; Haggmark, LG und Biersack, JP: Calculations

of nuclear stopping, ranges, and straggling in the low-energy region. *Physical Review B* (1977), Bd. 15, URL http://prb.aps.org/abstract/PRB/v15/i5/p2458_1
(Zitiert auf Seite 55)

[Xia03] Xiao Yue Zhai, Henrink Birn, Knud B. Jensen, Jesper S. Thomsen und Arne Andreasen, Erik I. Christensen: Digital Three-Dimensional Reconstruction and Ultrastructure of the Mouse Proximal Tubule. *Journal of the American Society of Nephrology : JASN* (2003), Bd. 14(3): S. 611–619, URL http://www.jasn.org/cgi/doi/10.1097/01.ASN.0000051725.00406.0C
(Zitiert auf Seite 93)

[Yao07] Yao, Nan: FOCUSED ION BEAM SYSTEMS Basics and Applications (2007), URL http://www.lavoisier.fr/livre/notice.asp?id=OA3WRSA2R66OWM
(Zitiert auf Seiten 8 and 9)

A Publications and Conferences

Weddemann, Alexander; Meyer, Judith; Regtmeier, Anna; Janzen, Irina; Akemeier, Dieter; Hütten, Andreas: Hydrogen-plasma-induced magnetocrystalline anisotropy ordering in self-assembled magnetic nanoparticle monolayers. *Beilstein journal of nanotechnology 4*, 164-172 (2013).

Bouchikhaoui, Houari; Stender, Patrick; Akemeier, Dieter; Baither, Dietmar; Hono, Kazuhiro; Hütten, Andreas; Schmitz, Guido: On the role of Ta cap in the recrystallization process of CoFeB layers. *Applied Physics Letters* 103, 142412-142415 (2013).

Pfullmann, Nils; Waltermann, Christian; Noack, Monika; Rausch, Stefan; Nagy, Tamas; Reinhardt, Carsten; Kovacev, Milutin; Knittel, Vanessa; Bratschitsch, Rudolf; Akemeier, Dieter; Hütten, Andreas; Leitenstorfer, Alfred; Morgner, Uwe: Bow-tie nano-antenna assisted generation of extreme ultraviolet radiation. *New Journal of Physics* 15, 93027 (2013).

Pfullmann, Nils; Waltermann, Christian; Kovacev, Milutin; Knittel, Vanessa; Bratschitsch, Rudolf; Akemeier, Dieter; Hütten, Andreas; Leitenstorfer, Alfred; Morgner, Uwe: Nano-antenna-assisted harmonic generation. *Applied Physics B* 113, 75-79 (2013).

Ennen, Inga; Albon, Camelia; Weddemann, Alexander; Auge, Alexander; Hedwig, Peter; Wittbracht, Frank; Regtmeier, Anna-Kristina;

Akemeier, Dieter; Dreyer, Axel; Peter, Michael; Jutzi, Peter; Mattay, Jochen; Mitzel, Norbert W.; Mill, Nadine; Hütten, Andreas: From Magnetic Nanoparticles to Magnetoresistive Biosensors. *Acta Physica Polonia A* 121 , 420-425 (2012).

Weddemann, Alexander; Albon, Camelia; Auge, Alexander; Wittbracht, Frank; Hedwig, Peter; Akemeier, Dieter; Rott, Karsten; Meissner, Daniel; Jutzi, Peter; Hütten, Andreas: How to design magneto-based total analysis systems for biomedical applications. *Biosensors and Bioelectronics* 26, 1152-1163 (2010).

Conferences

Akemeier, Dieter; Auge, Alexander; Wittbracht, Frank; Weddemann, Alexander; Hütten, Andreas: *Concepts for magnetoresistive sensors and microfluidic integration.* (Poster), Biosensors 2010, Glasgow

Akemeier, Dieter: *A magnetic microscope* (Talk), SFB 613 - Workshop 2009, Bad Salzdetfurth

Akemeier, Dieter; Albon, Camelia; Hedwig, Peter; Peter, Michael; Hütten, Andreas; Mattay, Jochen: *Single Molecule Detection and Manipulation inÊSpatio-Temporal Resolution with Magnetic Microsystems* (Poster), SFB 613 International Workshop 2010, Bielefeld

Akemeier, Dieter: *Nano-Structuring and Analytical Applications of a Dual-Beam FIB* (Talk), SFB 613 - Workshop 2011, Evengelische Akademie Loccum

Akemeier, Dieter: *Dual Beam Tomography Applications* (Talk), FEI European FIB/DualBeam User Club Meeting 2012, Eindhoven